

Quantitative Magnetic Resonance Imaging of Tissue Microvasculature and Microstructure in Selected Clinical Applications



Lea Starck

Thesis for the degree of Philosophiae Doctor (PhD)
University of Bergen, Norway
2022

UNIVERSITY OF BERGEN



Quantitative Magnetic Resonance Imaging of Tissue Microvasculature and Microstructure in Selected Clinical Applications

Lea Starck



Thesis for the degree of Philosophiae Doctor (PhD)
at the University of Bergen

Date of defense: 03.06.2022

© Copyright Lea Starck

The material in this publication is covered by the provisions of the Copyright Act.

Year: 2022

Title: Quantitative Magnetic Resonance Imaging of Tissue Microvasculature and Microstructure in Selected Clinical Applications

Name: Lea Starck

Print: Skipnes Kommunikasjon / University of Bergen

Scientific Environment

During my PhD studies I have been employed at the Department of Physics and Technology at the University of Bergen. I have also been affiliated with and shared office spaces at the Mohn Medical Imaging and Visualization Centre at the Department of Radiology at Haukeland University Hospital.

Associate Professor Renate Grüner at the Department of Physics and Technology at the University of Bergen has been my main supervisor for the PhD project. When I started the PhD project, she was centre leader at the Mohn Medical Imaging and Visualization Centre, Department of Radiology at Haukeland University Hospital. She is also Director of Research in Helse Vest.

Physicist Dr. Frank Riemer, senior researcher at Mohn Medical Imaging and Visualization Centre, as well as Associate Professor Hauke Bartsch, at the Department of Informatics at the University of Bergen and core staff member at the Mohn Medical Imaging and Visualization Centre, have been my co-supervisors.

The project was funded by the Trond Mohn Foundation through the VIDF project: Visual Data Science for Large Scale Hypothesis Management in Imaging Biomarker Discovery.



<https://mmiv.no/>

Acknowledgements

I thank my supervisor Renate Grüner who has guided and shown me how to become a researcher all the way through my master's degree studies, and now also through the PhD-track. Thank you, Renate, for all the feedback given over the past years, your kindness, and good humour. Your patience with my small and large worries have been a great help. I believe your ingenuity may very well have been the reason that I got to share an office with co-supervisors Frank Riemer and Hauke Bartsch.

I thank Frank Riemer and Hauke Bartsch for welcoming me into said office space. Hauke initially helped me quite a bit getting adjusted to Linux, and I'm certain that your various *<InsertProgrammingRelatedTopic>-Without-Any-Gaps-*tutorials have saved me tremendous amounts of time. Frank introduced me to diffusion MRI, has probably answered hundreds of my questions, and I could not have written Paper 4 without you. Thank you both for office, lunch and work-related chats.

I thank the patients who have participated in the studies by consenting that data was collected for research purposes also. I thank neurosurgeon Bente Skeie both for the collaboration on Papers 2 and 3 and for taking me along for a day in the clinic. I am glad that I was allowed to see for myself that a patient is much more than a data point.

I also thank the remaining co-authors; Erling Andersen, Ondřej Macíček, Radovan Jiřík, Oskar Angenete, Thomas A. Augdal, Karen Rosendahl, Gunnar Moen, Fulvio Zaccagna, Ofer Pasternak and Ferdia A. Gallagher.

I am grateful for the community at the Mohn Medical Imaging and Visualization Centre.

I thank my friends and family who have supported me throughout. You are my role models in patience, discipline, love and kindness. A thanks, as warm as their never-ending supply of coffee, goes to Borghild and Anna. Thank you for being my Covid squad and for letting me set up home office at the edge of your dining table.

Bergen 2022,

Lea Sjurine

Abstract

This thesis is based on four papers and aims to establish perfusion and diffusion measurements with magnetic resonance imaging (MRI) in selected clinical applications. While structural imaging provides invaluable geometric and anatomical information, new disease relevant information can be obtained from measures of physiological processes inferred from advanced modelling. This study is motivated by clinical questions pertaining to diagnosis and treatment effects in particular patient groups where inflammatory processes are involved in the disease.

Paper 1 investigates acquisition parameters in dynamic contrast enhanced (DCE)-MRI of the temporomandibular joint (TMJ) with possible involvement of juvenile idiopathic arthritis. High level elastic motion correction should be applied to DCE data from the TMJ, and the DCE data should be acquired with a sample rate of at least 4 s. Paper 2 investigates choices of arterial input functions (AIFs) in dynamic susceptibility contrast (DSC)-MRI in brain metastases. AIF shapes differed across patients. Relative cerebral blood volume estimates differentiated better between perfusion in white matter and grey matter when scan-specific AIFs were used than when patient-specific AIFs and population-based AIFs were used. Paper 3 investigates DSC-MRI perfusion parameters in relation to outcome after stereotactic radiosurgery (SRS) in brain metastases. Low perfusion prior to SRS may be related to unfavourable outcome. Paper 4 applies free water (FW) corrected diffusion MRI to characterise glioma. Fractional anisotropy maps of the tumour region were significantly impacted by FW correction. The estimated FW maps may also contribute to a better description of the tumour.

Although there are challenges related to post-processing of MRI data, it was shown that the advanced MRI methods applied can add to a more accurate description of the TMJ and of brain lesions.

List of publications

Paper 1: L. Starck, E. Andersen, O. Macíček, O. Angenete, T. A. Augdal, K. Rosendahl, R. Jiřík, and R. Grüner, "Effects of Motion Correction, Sampling Rate and Parametric Modelling in Dynamic Contrast Enhanced MRI of the Temporomandibular Joint in Children Affected With Juvenile Idiopathic Arthritis," *MRI*, vol. 77, pp. 204-212, 2021.

Paper 2: L. Starck, B. S. Skeie, H. Bartsch, and Renate Grüner, "Arterial Input Functions in Dynamic Susceptibility Contrast MRI (DSC-MRI) in Longitudinal Evaluation of Brain Metastases," Submitted.

Paper 3: L. Starck, B. S. Skeie, G. Moen, and Renate Grüner, "Dynamic Susceptibility Contrast MRI May Contribute in Stereotactic Radiosurgery Outcome Prediction in Brain Metastases," Submitted.

Paper 4: L. Starck, F. Zaccagna, O. Pasternak, F. A. Gallagher, R. Grüner, and F. Riemer, "Effects of Multi-Shell Free Water Correction on Glioma Characterization," *Diagnostics (Basel)*, vol. 11 no. 12, p. 2385, 2021.

Posters and presentations

L. Starck, "Effects of Sampling Rate in Dynamic Contrast Enhanced MRI of the TMJ in a Small Group of Children," in ISMRM Nordic Chapter, Trondheim 2018. (Oral presentation)

L. Starck, E. Andersen, O. Macíček, R. Jiřík, O. Angenete, T. A. Augdal, E. Hodneland, K. Rosendahl, and R. Grüner, "Effects of Image Registration in Dynamic Contrast-Enhanced MRI of the TMJ," in ISMRM, Montréal 2019. (Poster)

L. Starck, B. S. Skeie, H. Bartsch, R. Grüner, "Robust DSC Parameter Estimations in Patients With Brain Tumour Metastases," in MMIV Conference, Bergen 2020. (Oral presentation)

L. Starck, F. Zaccagna, O. Pasternak, F. A. Gallagher, R. Grüner, and F. Riemer, "Effects of Multi-Shell Free Water Correction on Glioma Characterization," in MMIV Conference, Bergen 2021. (Poster)

L. Starck, B. S. Skeie, H. Bartsch, R. Grüner, "Selection of Arterial Input Functions in Dynamic Susceptibility Contrast MRI in the Longitudinal Follow-Up of Brain Metastases," Submitted. (Poster)

Reprints are presented with permissions granted through open access publishing.

Contents

Scientific environment	i
Acknowledgements	ii
Abstract	iii
List of publications	iv
List of abbreviations	vii
List of figures	viii
List of tables	ix
1 Introduction	1
1.1 Basic principles of magnetic resonance imaging	1
1.1.1 The physics of MRI	1
1.1.2 Image encoding	4
1.1.3 MRI and quantitative measurements	6
1.2 Physiology of the microvasculature	9
1.2.1 Contrast agent administration to the circulatory system	9
1.2.2 Capillary architecture	9
1.3 Perfusion weighted imaging	11
1.3.1 Dynamic contrast enhanced MRI	11
1.3.2 Dynamic susceptibility contrast MRI	20
1.3.3 Arterial input functions	22
1.4 Diffusion weighted imaging	25
1.4.1 Measuring diffusion and constructing diffusion tensors	25
1.4.2 The apparent diffusion coefficient and noise	28
1.4.3 Indices and directionality	30
1.4.4 Free water elimination	31
1.5 Aims	33
1.5.1 Optimisation of perfusion measurements to evaluate juvenile idiopathic arthritis in the temporomandibular joint	33
1.5.2 Choice of arterial input functions	34
1.5.3 Perfusion measurements prior to stereotactic radiosurgery to predict outcome in brain metastases	34
1.5.4 Free water diffusion corrections applied to detect heterogeneity in glioma	35
2 Methods	37
2.1 Data collection	37
2.1.1 Patients and clinical scores	37
2.1.2 MRI protocols	37

2.2	Parameter extraction	38
2.2.1	Paper 1	38
2.2.2	Paper 2 and Paper 3	38
2.2.3	Paper 4	42
2.3	Statistical analyses	43
2.3.1	Paper 1	43
2.3.2	Paper 2	43
2.3.3	Paper 3	44
2.3.4	Paper 4	44
3	Results	45
3.1	Paper 1	45
3.2	Paper 2	45
3.3	Paper 3	45
3.4	Paper 4	46
4	Discussion	49
4.1	Paper 1	49
4.2	Paper 2	50
4.3	Paper 3	50
4.4	Paper 4	51
4.5	Remaining challenges and outlook	52
4.5.1	Number of patients	52
4.5.2	Image quality	53
4.5.3	Ethical concerns with use of contrast agent	53
4.5.4	Complementary information with different MRI indices	54
4.5.5	Application in the clinic	55
4.6	Conclusion	55
	References	57
	Appendices	77

List of abbreviations

Acronym	Description	Unit
AATH	Adiabatic Approximation to Tissue Homogeneity	
ADC	Apparent Diffusion Coefficient.....	mm ² /s
AIF	Arterial Input Function	
BAT	Bolus Arrival Time.....	min
CBF	Cerebral Blood Flow.....	ml/100 g /min
CBV	Cerebral Blood Volume.....	ml/100 g
CSF	Cerebral Spinal Fluid	
CT	Computed Tomography	
DCATH	Distributed Capillary Adiabatic Tissue Homogeneity	
DCE	Dynamic Contrast Enhanced	
DSC	Dynamic Susceptibility Contrast	
DTI	Diffusion Tensor Imaging	
DWI	Diffusion Weighted Imaging	
EES	Extravascular Extracellular Space	
EPI	Echo Planar Imaging	
FA	Fractional Anisotropy.....	-
FA _t	Free Water Corrected FA	
FLAIR	Fluid-Attenuated Inversion Recovery	
FW	Free Water	
GCTT	Gamma Capillary Transit Time	
JIA	Juvenile Idiopathic Arthritis	
MD	Mean Diffusivity.....	mm ² /s
MR	Magnetic Resonance	
MRI	Magnetic Resonance Imaging	
MTT	Mean Transit Time.....	min
PET	Positron Emission Tomography	
PWI	Perfusion Weighted Imaging	
rCBF	Cerebral Blood Flow.....	A.U.
rCBV	Cerebral Blood Volume.....	A.U.
ROC	Receiver Operating Characteristic	
ROI	Region of Interest	
SRS	Stereotactic Radiosurgery	
SVD	Singular Value Decomposition	
TE	Echo Time.....	ms
TH	Tissue Homogeneity	
TMJ	Temporomandibular Joint	
TR	Repetition Time.....	ms
2XCM	Two Compartment Exchange Model	

List of Figures

1	Net spin precession in a magnetic field.	3
2	The spin warp pulse sequence diagram	5
3	Frequency and spatial representations of MRI data	7
4	Modelling capillary architecture	10
5	A signal response curve	11
6	The extended Tofts model of tracer kinetics	15
7	The two-compartment exchange model	16
8	The tissue homogeneity model	17
9	The adiabatic approximation to the tissue homogeneity model	18
10	An arterial input function	22
11	Free and restricted Brownian motion	25
12	The Stejskal-Tanner sequence	26
13	Diffusion signal across b-values	29
14	Schematic overview of papers	37
15	Correlation between region of interest volume estimates in metastatic brain tumours	41
16	Fibre tracking in the left Superior Longitudinal Fasciculus 3	46

List of Tables

1	Summary of dynamic contrast enhanced MRI parameters	13
2	Summary of dynamic susceptibility contrast MRI parameters	20
3	Summary of patient cohorts	38
4	Summary of MRI protocols	39
5	Mean tract number, length, and irregularity with and without free water correction in whole brain tractography	47

1 Introduction

The work in this thesis encompasses advanced perfusion and diffusion weighted image acquisition and analysis in selected clinical applications. An overview is given pertaining to the general principles of magnetic resonance imaging (MRI). The theory of the more advanced perfusion and diffusion weighted imaging and analysis methods is presented, followed by a brief summary of current state-of-the-art in the field. These methods are applied to three selected clinical cases. First, a new diagnostic test for juvenile idiopathic arthritis (JIA) in the temporomandibular joint (TMJ) is explored, using perfusion weighted imaging (PWI). Second, to explore prognostic value, PWI is performed in the longitudinal follow-up of brain metastases treated with stereotactic radiosurgery (SRS). Third, diffusion weighted imaging (DWI) is applied to characterise glioma.

1.1 Basic principles of magnetic resonance imaging

MRI is based on a strong external magnetic field interacting with atomic nuclei that possess a net spin. A major source of resonance signals from the human body originate from hydrogen (^1H) atoms. The MRI measuring methods are well suited to describe geometry of structures, physiological changes, and chemical composition in tissue, for example in cancerous tumours. This is possible due to high spatial resolution (1 mm^3), dynamic tracking of contrast agents injected into the blood stream, recording of signal losses due to apparent diffusion, as well as the resonance frequency signatures caused by unique kinds of molecules.

1.1.1 The physics of MRI

A clinical MRI system has a large bore shaped coil magnet, typically producing a 1.5 T or 3 T homogeneous magnetic field directed into the magnet bore. The main field direction is usually denoted as the z-direction in a cartesian coordinate system. The field causes a net precession of the atomic spins in the body about the field direction, described by the Bloch equation (Eqn. 1) [1],

$$\frac{d\mathbf{M}(t)}{dt} = \gamma(\mathbf{M}(t) \times \mathbf{B}(t)) \quad (1)$$

which states that the change in time in net magnetic momentum \mathbf{M} , is proportional to the cross product between the net magnetic momentum and the applied magnetic field \mathbf{B} , with the gyromagnetic ratio, γ , acting as the constant of proportionality. The gyromagnetic ratio of an atomic nucleus is defined as its magnetic moment divided by its angular momentum. The magnetization amplitude is governed by the relations expressed in Eqn. 2,

$$|\mathbf{M}| \propto \frac{N\gamma^2 B_0}{3kT} \quad (2)$$

where M is the magnetization amplitude, N is the number of spins, γ is the gyromagnetic ratio, B_0 is the main field strength, k is the Boltzmann constant, and T is the temperature. At 42.58 MHz/T [2] hydrogen has the largest gyromagnetic ratio among all MR sensitive isotopes in the body. This, along with its high relative abundance [3], contributes toward the dominance of resonance signals derived from hydrogen atoms. By comparison the gyromagnetic ratios of other MR active isotopes, Fluorine (^{19}F) and Sodium (^{23}Na) which next to hydrogen, are the second and third most MR sensitive isotopes in the human body are 40.08 MHz/T and 11.27 MHz/T [3, 4], respectively. Placed in the main magnetic field, spins will align parallel and anti-parallel to it, populating different energy levels as described by the Boltzmann distribution (Eqn. 3) [3].

$$\frac{N_{\downarrow}}{N_{\uparrow}} = e^{-\frac{\Delta E}{kT}} \quad (3)$$

N_{\downarrow} and N_{\uparrow} are the number of spins aligned anti-parallel (high energy state) and parallel (low energy state) to the main field direction, respectively. ΔE denotes the energy difference between the energy states, k is the Boltzmann constant, and T is the temperature. The energy difference ΔE can be expressed in terms of frequency and in terms of magnetic field strength (Eqn. 4), from which the Larmor frequency, (Eqn. 5), can easily be calculated.

$$\Delta E = \omega \hbar = \gamma \hbar B_0 \quad (4)$$

$$\omega = \gamma B_0 \quad (5)$$

ω is the spin precession and resonance frequency, \hbar is the Planck constant divided by 2π , γ is the gyromagnetic ratio, and B_0 is the main magnetic field strength.

In order to excite the hydrogen atoms, an oscillating radio frequency pulse is applied. The radio frequency pulse has components perpendicular to the main field direction and a frequency equal to the resonance frequency of the hydrogen spins [3]. This causes the net magnetization that was aligned with the main field direction (along the z-axis) prior to the pulse application to flip towards the xy-plane, while simultaneously precessing about the z-axis (Fig. 1).

The excitation energy is released in the free induction decay signal following the excitation pulse. The spins relax back into their original positions. The relaxation process has two independent components; T1- and T2-relaxation, that is, the re-alignment along the main field direction (z-direction) and the loss of phase coherence in the xy-plane, respectively. The T1 and T2 relaxation times are defined according to Eqns. 6 and 7, when the exponents are set equal to one [1].

$$M_z(t) = M_{z,max} \left(1 - e^{-\frac{t}{T_1}} \right) \quad (6)$$

$$M_{xy}(t) = M_{xy,max} e^{-\frac{t}{T_2}} \quad (7)$$

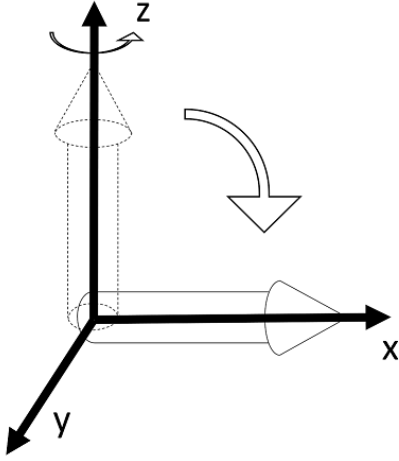


Figure 1: Excitation and net spin precession in a magnetic field. Application of a radio frequency pulse perpendicular to the main magnetic field direction parallel to the z-axis causes the net spin to flip toward the xy-plane. The cartesian frame of reference spins about an axis parallel to the z-axis with frequency identical to the net spin precession frequency.

M_z is the magnetization along the z-axis, $M_{z,max}$ is the steady state nuclear magnetization, that is, the magnetization along the z-axis prior to excitation. t is the elapsed time after the excitation pulse and $T1$ is the T1 relaxation time. Similarly, M_{xy} is the magnetization in the xy-plane, $M_{xy,max}$ is the maximum magnetization in the xy-plane, present prior to T2 relaxation, and $T2$ is the T2 relaxation time. It is the T1 and T2 times inherent to the various tissues that provide contrast in the final MR image [5]. Eqn.8 is the Bloch equation modified [1] to encompass the effects of relaxation,

$$\frac{d}{dt} \begin{pmatrix} M_x \\ M_y \\ M_z \end{pmatrix} = \begin{pmatrix} -\frac{1}{T2} & \gamma B_z & -\gamma B_y \\ -\gamma B_z & -\frac{1}{T2} & \gamma B_x \\ \gamma B_y & -\gamma B_x & -\frac{1}{T1} \end{pmatrix} \begin{pmatrix} M_x \\ M_y \\ M_z \end{pmatrix} + \begin{pmatrix} 0 \\ 0 \\ \frac{M_{z,max}}{T1} \end{pmatrix} \quad (8)$$

where M_x , M_y , and M_z and B_x , B_y , and B_z are the magnetic moment components and field strength components, respectively. $M_{z,max}$ is the steady state nuclear magnetization. $T1$ and $T2$ are the T1 and T2 relaxation times.

Gradients and radio frequency pulses are applied in specific patterns to de-phase and re-phase the response signal, producing a delayed resonance signal echo, the origin of which can be spatially located [6]. The sequences determining the timing and interplay between the pulses and gradients are called pulse sequences. The time between two successive excitation pulses is called repetition time (TR), and the time between the excitation pulse and sampling of the echo signal is called the echo time (TE). M_{xy} , the signal that the

receiver coils are sensitive to, is dependent on the chosen TR and TE , according to Eqn. 9, which is valid for a pulse sequence in which the echo signal response is generated by application of gradients and a longitudinal steady-state was reached [7, 8]. When a gradient echo is produced, some of the loss of phase coherence in the xy -plane is due to field inhomogeneities and not just neighbouring spin properties, for which reason the measured T2 time is often denoted $T2^*$.

$$M_{xy}(TR, TE, \alpha) \propto M_{z,max} \frac{\sin \alpha \left(1 - e^{-\frac{TR}{T1}}\right)}{\left(1 - (\cos \alpha) e^{-\frac{TR}{T1}}\right)} e^{-\frac{TE}{T2^*}} \quad (9)$$

M_{xy} is the magnetization in the xy -plane, $M_{z,max}$ is the steady state nuclear magnetization, α is the flip angle, and $T1$ and $T2^*$ are the T1 and T2 times, respectively. In other words, the image can be weighted according to the tissue inherent T1 and T2 relaxation times by adjusting the repetition and echo times. Thus, pulse sequences have three main tasks; determining image contrast weighting, creating resonance signal and signal echoes, and spatially encoding the sampled resonance echo signal.

1.1.2 Image encoding

To construct an MR image, it is necessary to locate the resonance signal origin. To select a slice of the three-dimensional object, a slice selective gradient is superimposed on the main magnetic field, causing a scale of spin precession frequencies along the gradient [6]. Only spins that are precessing with frequencies matching the excitation pulses will contribute to the sampled signal.

The sliced two-dimensional image is mapped to a cartesian frame of reference, as in the classic example of a spin warp sequence (Fig. 2) [9]. Signals along the x-axis are localised by application of a frequency encoding gradient, like, but applied subsequently to, the initial slice selection gradient. When a gradient is applied in the y-direction, spins along the y-axis will also acquire a range of precession frequencies. When the y-gradient is turned off, the spins will return to their original precession frequencies, but the phase of their periodic motion is shifted. With multiple phase encoding steps, the phase shift can be detected by measuring the amount of signal interference caused by the phase encoding gradient.

Because the sampled MRI signal is a mix of many frequencies, a Fourier transform [10], is applied to detect which frequencies are in the signal, such that the intensity per frequency can be extracted. Eqn. 10 is the general form of a Fourier transform of an infinite continuous signal,

$$F(v) = \int_{-\infty}^{\infty} f(t) e^{2\pi i t v} dt \quad (10)$$

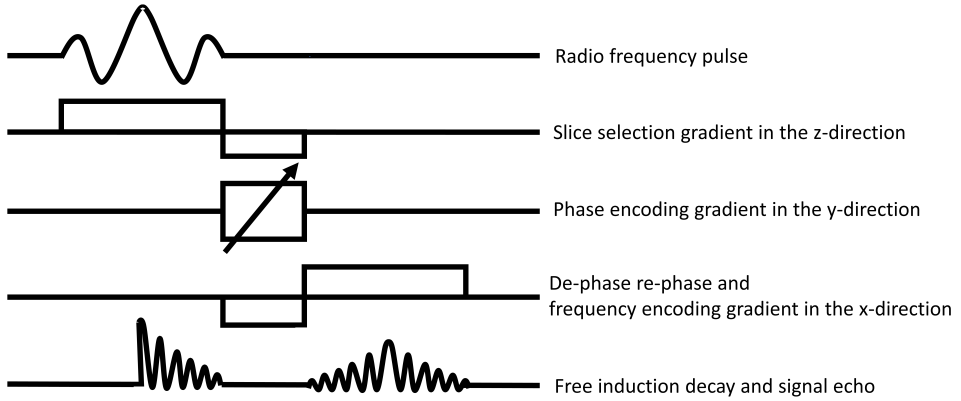


Figure 2: The spin warp pulse sequence diagram. A slice selection gradient in the z-direction is applied simultaneously to the radio frequency and overlapping with the initial free induction decay. The sampled signal echo is generated by a de-phase re-phase and frequency encoding gradient in the x-direction. A phase encoding gradient with varying amplitude is applied in the y-direction for every radio frequency pulse repetition.

where $F(v)$ is the signal in the frequency domain and $f(t)$ is the signal in the time domain.

Any image can be Fourier transformed and mapped to a complex plane, according to its spatial frequencies. Spatial frequencies in the horizontal direction can be viewed as vertical line densities. Correspondingly, spatial frequencies in the vertical direction can be viewed as horizontal line densities. The Fourier transform can be applied both in the horizontal and vertical direction to obtain a two-dimensional frequency representation of any regular image (Eqn.11),

$$F(u, v) = \int_{-\infty}^{\infty} \int_{-\infty}^{\infty} f(x, y) e^{2\pi i(xu + yv)} dx dy \quad (11)$$

where $F(u, v)$ is the frequency encoded image intensities as a function of the vertical and horizontal line densities and $f(x, y)$ is the regular image in the spatial domain. By applying the inverse Fourier transform to the frequency representation of an MR image, the conventional MR image in the spatial domain is generated. Low spatial frequencies correspond to slow intensity changes in the image, containing the contrast information and general shapes. High spatial frequencies correspond to rapid intensity changes in the image, corresponding to image resolution.

Facilitating MRI, in that it organises the measured resonance echo signal in the spatial frequency domain, k-space is defined (Fig. 3) [11, 12]. It is a coordinate system with axes

labelled k_x and k_y , where $k_x = \gamma G_x m \Delta t$ and $k_y = \gamma n \Delta G_y \tau$. γ is the gyromagnetic ratio, and G_x and G_y are the frequency encoding gradients in the respective k_x and k_y directions. m is the sample number in the k_x direction and n is the sample number in the k_y direction, also known as the partition number. Finally, Δt is the elapsed time between each signal sample point in the k_x direction and τ is the length of time that the G_y gradient is applied for. The k-space axes have units of m^{-1} .

The reason why the MR signal can be mapped directly to k-space is that while the sampling gradient remains switched on, spins along the readout direction will, as previously discussed, precess with a frequency dependent on their position. Since phase shift scales with frequency and time, phase shift increases with the duration of the gradient. According to the definition of k_x , k can be thought of as the gyromagnetic ratio multiplied by the area under the gradient. The phase shift is cyclic and increases with increasing area under the gradient. While the area is still small, the image raw data consists of few phase cycles, whereas as time goes on, more cycles fit into the field of view. Large objects can be detected with low frequency phase cycles since different parts of it will have unique phase shifts, whereas they will be invisible to high frequency phase cycles because signals with phases shifted 180° will cancel out. Conversely, the resolution of small objects becomes possible with the high frequency phase cycles. In other words, the frequencies of the phase cycles correspond to spatial frequencies analogous to the Fourier transformation of a regular spatial image. To arrive at a spatial representation of the information contained in the sampled frequencies, which will constitute the final MR image, the inverse Fourier transform is applied to the sampled k-space in both directions [11, 12]. Since the measurement points are discrete, the discrete Fourier transform is applied (Eqn. 12), and is usually computed using the fast Fourier transform approach [10].

$$f(x, y) = \frac{1}{mn} \sum_{k_x=0}^{m-1} \sum_{k_y=0}^{n-1} F(k_x, k_y) e^{-2\pi i \left(\frac{x k_x}{m} + \frac{y k_y}{n} \right)} \quad (12)$$

$f(x, y)$ is the spatial proton density representation and $F(k_x, k_y)$ is the spatial frequency representation of the MR image.

1.1.3 MRI and quantitative measurements

The physical quantities T1 and T2 are rarely measured in MRI. Rather, as discussed above, the MRI contrast is dependent on the proton density and the amount of T1 and T2 weighting as determined by the pulse-sequence parameters, such as echo- and repetition times, flip angle, as well as net magnetic field strength and the imaged isotope. While it is true that an MR image is usually composed of thousands of imaging voxels, each representing a mean signal value that scales with proton densities, there is no fixed scale of image brightness that corresponds to a certain proton density.

There are also additional mechanisms that can cause a voxel to display a brightness that does not correspond to the real proton density at the location of the voxel. Some of these

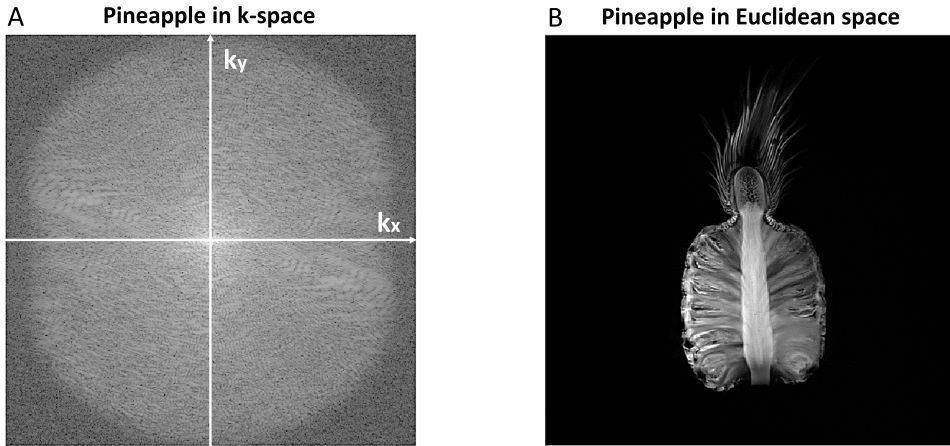


Figure 3: k-space (A) stores the spatial frequency representation of a pineapple along the k_x and k_y axes. The MR image (B) is a more familiar spatial representation of that same pineapple.

are artefacts caused by the imaging hard-ware, encompassing for example gradient field non-linearity and radio frequency pulse distortions, causing voxel misregistration due to physical limitations of the coils and magnets [13, 14]. Another group of artefacts are inherent to physics, the natural phenomena that are exploited in the imaging process. Among these are chemical shifts and susceptibility artefacts. Chemical shifts are caused by slight differences in resonance frequency that depend on the molecular structure in which the hydrogen atoms are bound [15]. Susceptibility artefacts occur when the spins are subjected to local field distortions that arise depending on the para- or diamagnetic properties of the various materials of which the imaged object is composed [16]. Susceptibility properties are the basis for use of exogenous contrast agents. Physiology can also be the origin of artefacts. Among these are flow effects and motion. Spins that are flowing may be moving from one phase and frequency encoded area to another during the MRI measurement, causing loss or gain of signal in different voxels, and misregistration of the signal in the phase encoding direction [17]. Similarly, when patients or their organs move, it can cause errors in magnitude and registration of the signal.

To correctly interpret MR images, one is usually dependent on expert radiologists. Their numerous years of experience are paramount to identify expected tissue structures and abnormalities warranting medical attention. Even when contrast agents are applied, so that enhancing areas of interest are achieved, based on a static MR image it is not always obvious at an early stage whether for example a tumour has responded to treatment or not. The bright contrast enhanced signal could be interpreted either as scar tissue, or as a growing tumour [18–20]. In other instances, it may not yet be obvious what abnormal-

ities to look for, such as in the diagnostics of arthritis in the TMJ [21–23]. PWI and DWI can be applied to obtain quantifiable physiological measurements and to establish MRI as a quantitative measuring tool in the clinic.

By introduction of contrast agents or tracers to the blood stream, tissue dynamics can be explored. These kinds of measurements are usually referred to as perfusion weighted MRI, i.e., PWI. Dynamic PWI, such as dynamic contrast enhanced (DCE)-MRI [24] and dynamic susceptibility contrast (DSC)-MRI [25, 26], provides new information that is not present in a basic structural MR image. Visualising dynamics for efficient interpretation by the radiologists can be a challenge but is facilitated by computing parameter maps. The parameter maps constitute voxel-wise estimates of perfusion related physical properties of the tissue and are computed by application of appropriate models of the tissue microvasculature.

Diffusion weighted MRI, i.e., DWI, is another approach to generate quantitative measurements, simultaneously revealing some of the qualities of the investigated tissue microvasculature. Diffusion measurements are based on random motion of molecules, the mean diffusivity being the average total distance covered by a randomly moving molecule per unit time [27]. As diffusing spins are exiting the region along the chosen gradient direction, their phase shift will no longer match that of the surrounding spins. When a gradient of opposite polarity is applied, a signal loss will occur, since the moving spins will not regain their original phase [28]. Based on this signal loss, the amount of diffusion in a given direction can be detected. In general, diffusion in tissue cannot be regarded as isotropic, since the tissue is full of barriers that restrict otherwise random diffusion motion. When diffusion is measured in multiple directions, these barriers defining the tissue structure can, to a degree, be reconstructed.

Specific research questions investigated as part of this thesis are:

- How should DCE imaging data from the TMJ in children that are being investigated for JIA be acquired and processed? Do they provide useful information in the diagnosis of JIA?
- What normalisation should be applied for optimal longitudinal follow-up of DSC parameters in patients with brain metastases that are treated with SRS?
- Can DSC-MRI data acquired prior to SRS help predict outcome in patients with brain metastases?
- Can free water (FW) estimations and FW corrected data improve characterisation of tumours in treatment naïve glioma patients?

The use of PWI and DWI in the clinic is dependent on application. Before returning to the above research questions, a description is given of tissue microstructure, PWI and DWI.

1.2 Physiology of the microvasculature

1.2.1 Contrast agent administration to the circulatory system

Investigating microvasculature using PWI, a standard contrast agent administration consists of chelate embedded Gadolinium, at a dosage of 20 ml/ 100 kg (0.1 mmoles/kg) [29, 30]. As a rule, contrast agent is injected intravenously using a power injector and a subsequent saline flush. The power injector ensures accurate and repeatable flow rates of contrast [31]. The saline flush is injected to clear contrast agents from the veins, creating a sharper pass bolus as it is pushed toward the heart [32]. After passing through heart and lungs, the contrast is circulated through the other organs in the body [33]. Recirculation and down-stream dilution effects can prevent the contrast-time curve from returning to baseline [32]. Initially, the half time of Gadolinium based contrasts in the body ranges between 70 and 120 minutes [34], but there has recently been raised some concern about residual Gadolinium accumulating in the brain after repeated usage [34–36].

1.2.2 Capillary architecture

When imaging the microvasculature, one is limited to the size of a voxel containing intravascular and extravascular extracellular space (EES) space (Fig. 4a). The intravascular space, containing blood plasma and red blood cells, consists of multiple arterioles branching out into capillaries (diameter 8-10 μm) [37]. The contrast agent is assumed to be well mixed in the blood plasma, but the space taken up by the red blood cells is not available to it [38]. Capillaries form a web and can be modelled as a collection of straight tube segments [39–41] (Fig. 4b). They are collected again as they drain into the venules. If the vessels are leaky, contrast agent will also accumulate in the EES before slowly diffusing back into the blood stream and being washed out through the kidneys [33].

Inflammatory conditions are characterised by changes in the microvascular function [42]. Arterioles may dilate, increasing blood flow, which in turn increases the fluid extravasation gradient across the endothelial wall coating of capillaries and venules [42, 43]. Where the capillary web becomes disrupted or altered due to angiogenesis, which is typical in the case of cancers, there will be an effect on perfusion measurement parameters [44, 45]. Increases in fluid content and defective cell membranes will affect diffusion measurements [46]. Alterations in microvascular function forms a basis for using advanced MRI to explore extent and physiology of chronic inflammatory diseases.

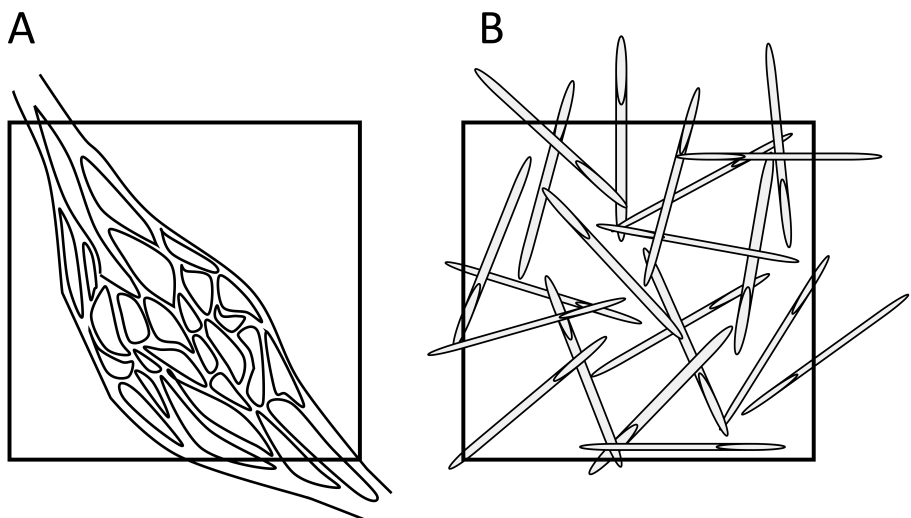


Figure 4: Modelling capillary architecture. A voxel containing intravascular and extracellular space (A) and capillaries modelled as randomly oriented straight tube segments (B). The intravascular space can contain both arterioles and capillaries.

1.3 Perfusion weighted imaging

According to the Oxford Lexico dictionary, in a medical context, perfusion refers to “the passage of blood, a blood substitute, or other fluid through the blood vessels or other natural channels in an organ or tissue” [47]. Perfusion related measurements can be performed using a variety of imaging modalities, such as positron emission tomography (PET), computed tomography (CT) and MRI [48]. Commonly, PWI relies on measuring dynamic signal changes related to tracers in the blood stream. When an exogenous contrast agent is administered, PWI is performed with DCE-MRI [24], or DSC-MRI [25, 26]. Common to DSC- and DCE-MRI is the dynamic measurement of the tissue contrast response curve, as well as the arterial input function (AIF), which denotes the contrast flowing into the tissue. As will be further discussed below, the deconvolution of these functions reveals important properties of the physiology under investigation.

1.3.1 Dynamic contrast enhanced MRI

By repeatedly acquiring T1-weighted images prior to, during and after the passing of the injected contrast agent, the aim of DCE-MRI is to arrive at quantitative parameter estimations from the tissue response curve. Some of these parameters can be estimated directly from the signal response curve [49]. These include steepness, maxima, time to peak, area under the response curve, and bolus arrival time (Fig. 5).

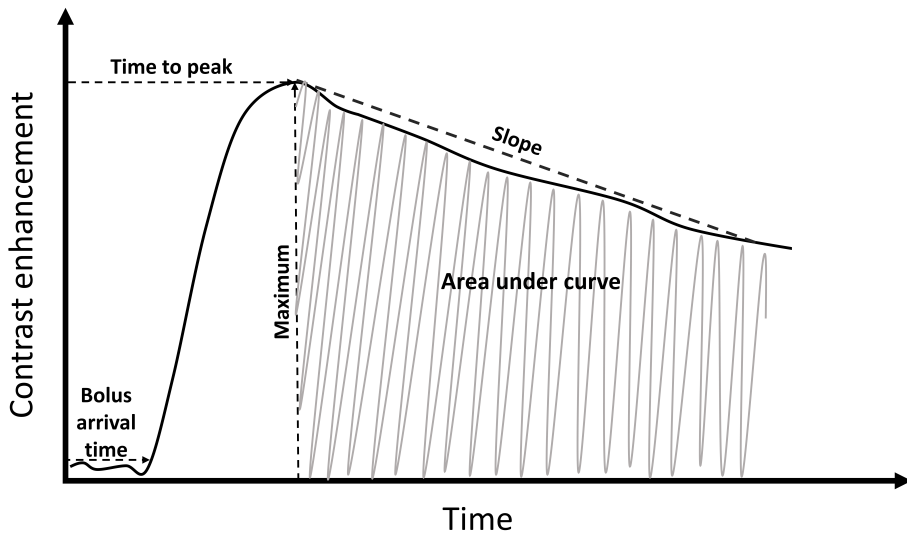


Figure 5: A signal response curve. The signal response curve in dynamic contrast enhanced MRI is used to infer parameters such as slope of tail, maximum, time to peak, area under the response curve, and bolus arrival time.

Other parameters are derived from tracer kinetic models that assume various physiological tissue properties and must be estimated by deconvolution of the AIF and contrast response curve [24]. A short summary of relevant tissue parameters is presented in Table 1. The tissue can be visualised in terms of the estimated parameters by generating parameter maps where each pixel representing a parameter estimation corresponds to an imaging voxel in the structural image. The contrast molecules can traverse the vascular endothelium of the vessels and capillaries in the body by way of passive diffusion, though usually assumed, not through the blood brain barrier unless it is disrupted [50]. As time passes, contrast agent will accumulate in the EES until it slowly diffuses back into the blood stream and is washed out of the body through the kidneys. However, recent studies have shown that incomplete excretion from both brain and kidneys is a concern [51]. Both T1 and T2 relaxation times are shortened by the contrast agent [52–54]. The T1 relaxivity is usually assumed to be linearly related to contrast agent concentration and expressed according to Eqn.13 [53–55],

$$R_1 = R_{1,0} + r_1 \cdot C \quad (13)$$

where $R_1 = \frac{1}{T_1}$ is the total T1 relaxivity, $R_{1,0} = \frac{1}{T_{1,0}}$ is the tissue T1 relaxivity in the absence of contrast agent, r_1 is the contrast agent T1 relaxivity, and C is the contrast agent concentration. R_1 , $R_{1,0}$ and r_1 are theoretically known quantities, though they depend on field strength, tissue and chemical composition [54]. Both gradient and spin echo sequences can be applied to acquire the DCE images [56]. Eqn. 9, remains valid when gradient echoes are applied and is then used to relate the signal intensity to the contrast agent concentration present in a voxel at a given time. Because the T1 relaxivity is increased by the contrast agent, the T1 relaxation time is shortened, and the contrast signal increased. To generate T1-weighted images, DCE-MRI is performed with short TR (≤ 500 ms) and TE (≤ 10 ms). Because the TR is short, the flip angle is also kept small ($\leq 20^\circ$) [56]. Total acquisition time typically exceeds five minutes.

To estimate perfusion parameters, it is necessary to make some assumptions about the tissue that is investigated. The sum of these assumptions can be regarded as a tissue model, to which the data are fitted. One can think of the models as dividing the tissue into different volumes and imposing certain rules about how the contrast may travel through the system of these volumes. Assuming contrast agent can neither be generated nor destroyed in the system, these rules are summarised mathematically. As the data are fitted, one finds an impulse function $H(t)$ which is convolved with the AIF to yield the measured contrast response curve. In PWI literature one is often referred to the residue function [38, 57], as defined as in Eqn. 14,

$$R(t) = 1 - \int_0^\infty H(t)dt \quad (14)$$

Parameter	Unit	Description
α^{-1}	-	Width of capillary transit time distribution
BAT	min	Bolus arrival time
E	-	Extraction fraction
F_p	ml/ml/min	Blood plasma flow
K^{trans}	1/min	Transfer constant
K_{ep}	1/min	Rate constant
PS	ml/ml/min	Permeability surface area product
σ	min	Standard deviation of mean transit time
T_c	min	Mean capillary transit time
v_e	-	Extravascular extracellular volume
v_p	-	Plasma volume

Table 1: Summary of dynamic contrast enhanced MRI parameters. Perfusion parameters (α^{-1} , BAT , E , F_p , K^{trans} , F_p , PS , σ , T_c , v_e and v_p) estimated by application of dynamic contrast enhanced MRI and pharmacokinetic modelling.

$R(t)$ reflects the amount of contrast agent concentration left in the capillary after a time t . Intuitively $R(0) = 1$ and $\lim_{t \rightarrow \infty} R(t) = 0$. The mean capillary transit time can therefore defined as in Eqn. 15.

$$T_c = \int_0^{\infty} R(t) dt \quad (15)$$

Theoretically, a residue function could contain all information about the microcirculation [58], however the deconvolution does not have a unique solution when it contains more than one unknown parameter, nor is any measurement completely free of noise. In DCE-MRI several tissue models have been developed in order that one may reasonably account for unique features of the physiology.

Tofts model

The Tofts model [59], assumes that a voxel contains two parts; blood vessels or capillaries, and EES (Fig. 6). The blood vessel or capillary contains volumes of blood plasma, as well as erythrocytes. As a rule, the contrast agent concentration is somewhat higher in the plasma regions, than in the total blood volume, and is calculated according to Eqn. 16 [38],

$$C_b = \frac{C_p}{1 - Hct} \quad (16)$$

where C_p and C_b are the contrast agent concentrations in plasma and blood volumes respectively, and Hct is the ratio of plasma to blood. The Tofts model also assumes that the contrast agent is well mixed in the blood vessel, and that the amount of contrast passively diffusing into the EES is proportional to the relative amount of contrast present on either side of the dividing wall comprised of the vascular endothelium [59]. In other words, the contrast agent may passively diffuse back and forth across the capillary wall. The original formulation of Tofts model [59], neglects the fractional plasma volume v_p , such that based on conservation of mass, the descriptive differential equation becomes Eqn. 17 [24]. Eqn. 18 is the integral form.

$$\frac{C_t(t)}{dt} = K^{trans} \left(C_p(t) - \frac{C_t(t)}{v_e} \right) \quad (17)$$

$$C_t(t) = K^{trans} \int_0^t C_p(\tau) e^{-\left(\frac{K^{trans}}{v_e}\right)(t-\tau)} d\tau \quad (18)$$

C_p corresponds to the measurable AIF and C_t is the measured tissue contrast response curve. The equation has two unknowns, the transfer constant K^{trans} and the fraction of the total volume that is EES and where the contrast agent may diffuse; v_e . These unknown quantities are estimated by fitting the measured AIF and contrast response curve to the model. By definition, $k_{ep} = K^{trans}/v_e$ [24], and is easily calculated. How much contrast that may diffuse into the EES per time, K^{trans} depends on the blood flow F_p in the capillary, the capillary surface S , and how permeable it is, P [60]. Oftentimes, S and P are simply collected in a single parameter, the surface permeability product PS [60, 61].

Given that the total contrast concentration, C_T , equals the sum of concentrations in the capillary $v_p C_p(t)$ and tissue concentration $C_t(t)$, Eqn. 18 can be modified to Eqn. 19 [24]. The extended Tofts model includes the plasma volume v_p and therefore has three unknown parameters that must be fitted to the data.

$$C_T(t) = v_p C_p(t) + K^{trans} \int_0^t C_p(\tau) e^{-\left(\frac{K^{trans}}{v_e}\right)(t-\tau)} d\tau \quad (19)$$

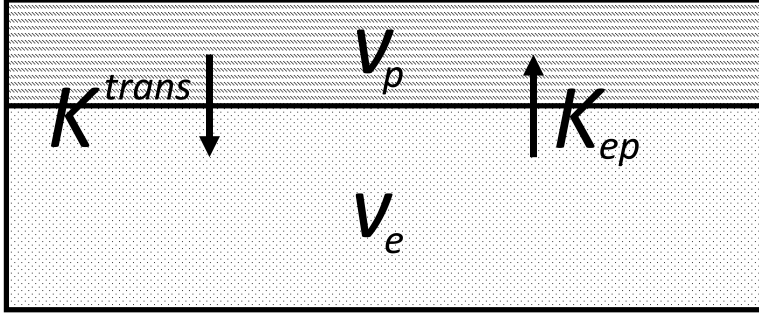


Figure 6: The extended Tofts model of tracer kinetics. The model divides a voxel into two parts; the blood vessel or capillary (top box), and the compartment of extravascular extracellular space (EES) (bottom box). The extended Tofts model seeks to estimate the relative volumes of the capillary (v_p) and EES (v_e), as well as the transfer rate (K^{trans}) of contrast into the EES and the reverse transfer rate of contrast diffusing back into the capillary from the EES (k_{ep}).

Two-compartment exchange model

The two-compartment exchange model (2CXM) was proposed by Brix et al. [62, 63], and it describes the capillary system with two differential equations (Eqns. 20 and 21). The equations correspond to two compartments. The EES is counted as a compartment, as is the capillary, where blood enters the arterial end and exits the venous end, and from which it can diffuse into the EES (Fig. 7).

$$V_p \frac{C_p(t)}{dt} = F_p (C_a(t) - C_p(t)) - PS (C_p(t) - C_t(t)) \quad (20)$$

$$V_t \frac{C_p(t)}{dt} = PS (C_p(t) - C_t(t)) \quad (21)$$

Assuming well mixed volumes, the amount of contrast that enters or leaves the capillary is equal to the plasma volume V_p multiplied by the change in contrast agent concentration $\frac{dC_p(t)}{dt}$. The first term of the right-hand side of Eqn. 20 describes the difference between contrast agent concentration entering the capillary $C_a(t)$ (AIF), and the concentration in the capillary $C_p(t)$ that will leave, multiplied by the blood flow F_p . The second term of the right-hand side of Eqn. 20 describes the amount of contrast leaving into the EES, which is proportional to the difference in contrast agent concentrations in the capillary and in the tissue, $C_t(t)$. Eqn. 21 is simply the negative equivalent of the second term on

the right-hand side of Eqn. 20, it describes the contrast agent that enters the EES volume V_e . Finally, the measured contrast response curve $C_T(t)$ is given by Eqn. 22,

$$C_T(t) = v_p C_p(t) + v_e C_t(t) \quad (22)$$

where $C_p(t)$ and $C_t(t)$ are the contrast agent concentrations in the capillary and EES respectively, and where $v_p = V_p/V_T$ and $v_e = V_e/V_T$ correspond to the volume ratios of the plasma volume and the EES volume to the total volume V_T .

The 2CXM model requires a temporal resolution that is sufficient for resolving K^{trans} into F_p and PS [57, 60]. Given F_p and PS one may calculate the extraction fraction E Eqn. 23. It is the fraction of the contrast entering the capillary which is extracted into the EES.

$$E = \frac{\int_0^\infty PS \cdot C_p(t) dt}{\int_0^\infty F_p \cdot C_p(t) dt} = \frac{PS}{F_p} \quad (23)$$

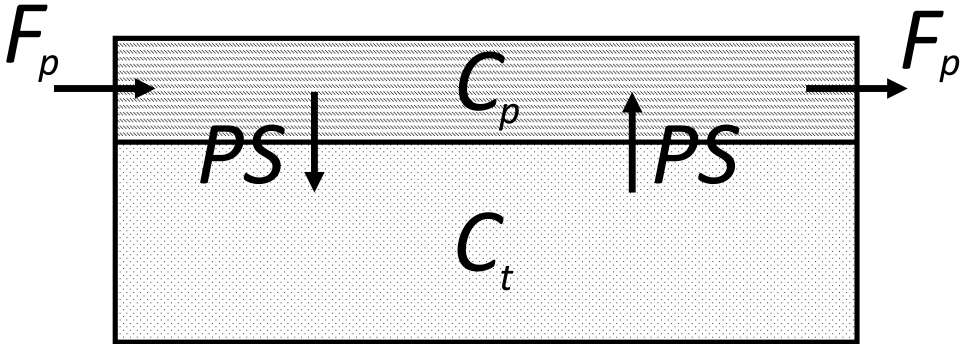


Figure 7: The two-compartment exchange model (2CXM).¹ In the 2CXM blood, containing contrast, enters the capillary compartment in the arterial end and exits through the venous end. Contrast can also diffuse across the endothelial wall between the capillary compartment and extravascular extracellular space. The contrast is well mixed in the compartments.

¹Fig. 7 is an adaption of a figure presented by Brix et al. [62].

Tissue homogeneity model

Contrary to the Tofts model and the 2CXM, the tissue homogeneity (TH) model does not assume that the capillary is well mixed [64]. Instead, a plug-flow model is assumed, in which the contrast agent concentration is initially reduced with increasing distance from the capillary arterial inlet and is dependent on time (Fig. 8). Again, from the conservation of mass, one arrives at coupled pair of equations (Eqns. 24 and 25) [65].

$$A_p \frac{\partial C_p(x,t)}{\partial t} = -F_p \frac{\partial C_p(x,t)}{\partial x} - \frac{PS}{L} \left[C_p(x,t) - \frac{C_t(t)}{\lambda} \right] \quad (24)$$

$$A_t L \frac{dC_t(t)}{dt} = \frac{PS}{L} \int_0^L \left[C_p(x,t) - \frac{C_t(t)}{\lambda} \right] dx \quad (25)$$

$C_p(x,t)$ and $C_t(t)$ are the contrast agent concentrations in the capillary and EES, respectively. Similarly, A_p and A_t are the cross-sectional areas of the compartments. F_p denotes the blood flow, PS is the permeability surface area product, L is the capillary length and λ is the equilibrium partition coefficient. The solution to the TH equations is rather complicated but can be handled in the frequency domain by performing Laplace or Fourier transforms, where closed form solutions exist [65, 66].

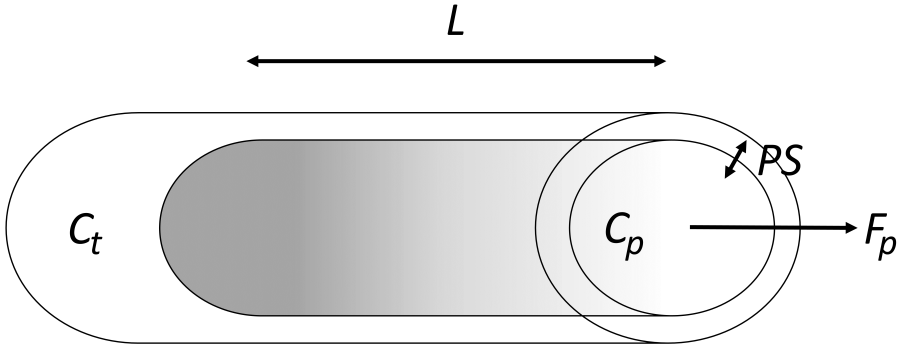


Figure 8: The tissue homogeneity model (TH).² In the TH model blood, containing contrast enters, the capillary compartment in the arterial end and exits through the venous end. Contrast diffuses across the endothelial wall between the capillary compartment and extravascular extracellular space. The amount of contrast is dependent on distance (L) from the arterial inlet and time.

²Fig. 8 is an adaption of a figure presented by St. Lawrence and Lee [65].

Adiabatic approximation to the tissue homogeneity model

The adiabatic approximation to the tissue homogeneity (AATH) model assumes that the contrast agent concentration in the EES changes slowly compared to the contrast agent concentration in the capillary [65, 67]. Thus, a simplification to the TH model is made where for short time intervals the change in EES contrast concentration is assumed to be zero, in other words, it changes only in discrete steps (Fig. 9). The adiabatic approximation is performed by substituting Eqn. 26 into Eqns. 24 and 25,

$$C_t(t) = \sum_{j=0}^{n-1} \Delta C_t(j\Delta t)u(t-j\Delta t) \quad (26)$$

where $\Delta C_t(j\Delta t)$ is the discrete change in contrast agent concentration in the EES and $u(t-j\Delta t)$ is the unit step function. St. Lawrence and Lee [65, 67], showed that the AATH impulse function, i.e., the solution to this problem is simpler than the TH model solution and can be handled in the temporal domain (Eqn. 27),

$$H(t) = \begin{cases} 1 & 0 \leq t < T_c \\ Ee^{-\frac{EF_p}{v_e}(t-T_c)} & t \geq T_c \end{cases} \quad (27)$$

where the solution describes that there is a fixed time before contrast is extracted through the venous end of the capillary. E is the extraction fraction, F_p is the blood flow, v_e is the EES volume and T_c is the mean transit time. They are estimated based on the numerical fitting of the measured AIF and contrast response curve to the model.

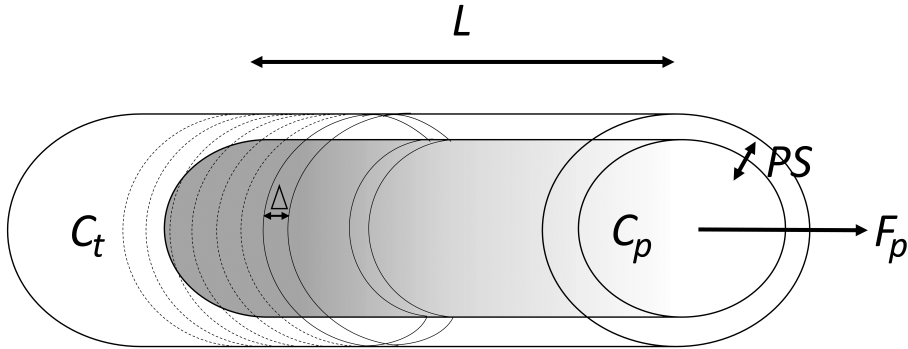


Figure 9: The adiabatic approximation to the tissue homogeneity (AATH) model.³ The AATH model is similar to the tissue homogeneity model, however, the contrast agent concentration changes in discrete steps along the distance (L) from the arterial inlet.

³Fig. 9 is an adaption of a figure presented by St. Lawrence and Lee [65].

Distributed capillary adiabatic tissue homogeneity model

The distributed capillary adiabatic tissue homogeneity (DCATH) model was originally motivated by the fact that cancerous vasculature architecture is different from that of normal tissue [68]. The hypothesis was that the variability of transit times would be greater in cancerous tissues than that in normal tissues. Koh et al. [68], chose to model an imaging voxel not as a single capillary compartment accompanied by the EES, but as is closer to the truth, that there are many capillaries within a voxel, each with their own transit time. Consequently, the DCATH model assumes a probability density function of T_c , i.e., capillary transit times (Eqn. 28).

$$\frac{1}{N} \int_0^t g(T_c) dT_c = \int_0^t g_c(T_c) dT_c = 1 \quad (28)$$

The distribution function $g(T_c)$ can be assumed to be Gaussian, where N is an ad hoc normalisation factor that is introduced to incorporate the physical necessity of the lower limit of T_c to be non-negative, and $g_c(T_c) = \frac{1}{N}g(T_c)$. Alternatively, an assymmetric distribution could be chosen for $g_c(T_c)$, incorporating the gamma function, smoothly decreasing to zero, and otherwise decaying like the normal distribution. In both cases, the standard deviation σ of the distribution is an additional parameter that must be estimated in the numerical deconvolution of the AIF and contrast response curve [68]. With the assumption in Eqn. 28, the AATH impulse function Eqn. 27 can now be rewritten as Eqn. 29

$$H(t) = \begin{cases} 1 - \int_0^t g_c(T_c) dT_c & 0 \leq t < T_c \\ E e^{-\frac{EF_p t}{v_e}} \int_0^t g_c(T_c) e^{-\frac{EF_p t}{v_e}} dT_c & t \geq T_c \end{cases} \quad (29)$$

Gamma capillary transit time model

The gamma capillary transit time (GCTT) model is based on the DCATH model (Eqn. 29), but exchanges the DCATH probability distribution $g(T_c)$ for a normalised gamma probability distribution of transit times [69]. The inverse of the gamma distribution shape parameter, i.e., $\alpha^{-1} = \tau/T_c$ is proportional to the scale parameter τ of the distribution, and hence represents a measure of the width of the distribution. It has been shown that in the limit $\alpha^{-1} \rightarrow 0$, the GCTT model impulse response approaches the impulse response of the AATH model and when $\alpha^{-1} \rightarrow 1$, the GCTT model impulse response approaches that of the 2XCM [69].

While there have been proposed many pharmacokinetic models, simpler models like the Tofts model remain frequently applied. These models have fewer target parameters. When choosing a model, it is important to consider how plausible its a priori parameter assumptions are, and whether increasing the number of fitted parameters sufficiently improves the fit [57]. With increasing complexity of the models, additional features of the tissue of interest can be described, though it comes at the cost of the need for higher temporal resolutions and increased signal to noise ratios, since adding additional free parameters increases the risk of over-fitting and one would rather avoid modelling noise. Improved MRI scanner capabilities may help alleviate these issues.

1.3.2 Dynamic susceptibility contrast MRI

Under the assumption that contrast agent does not traverse the blood brain barrier thus accumulating in the tissue [50], first pass bolus tracking, i.e., DSC-MRI, has predominantly been used for perfusion imaging in the brain [55]. It remains true that both T1 and T2 relaxation times are shortened by the contrast agent. The T2 relaxivity is expressed in Eqn. 30.

$$R_2 = R_{2,0} + r_2 \cdot C \quad (30)$$

where $R_2 = 1/T_2$ is the total T1 relaxivity, $R_{2,0} = 1/(T_{2,0})$ is the tissue T2 relaxivity in the absence of contrast agent, r_2 is the contrast agent T1 relaxivity, and C is the contrast agent concentration, analogous to Eqn. 13 [52]. Gradient echo sequences are commonly applied in DSC-MRI, generating T2-weighted images, typically with somewhat longer TR (≤ 2000 ms) and TE (30-50 ms) as well as a larger flip angle (60-90 °) than in DCE-MRI, but the total acquisition time is limited to approximately two minutes [56]. In contrast to T1 relaxivity, the T2 relaxation causes a hypointense signal.

Like in DCE-MRI, the DSC-MRI contrast response curves can be used to estimate semi-quantitative perfusion parameters [70]. However, the main interest lies in estimating cerebral blood flow (CBF), cerebral blood volume (CBV) and mean transit time (MTT) [71] (Tab. 2), of contrast agent in the capillary bed. The capillary bed is simply taken to be the imaging voxel. A correct parameter estimation relies on the system behaving linearly [72], that is, that contrast is neither created nor destroyed within the system and that the rules of linear superposition apply.

Parameter	Unit	Description
CBF	ml/min/100 g	Cerebral blood flow
CBV	ml/100 g	Cerebral blood volume
MTT	min	Mean transit time

Table 2: Summary of dynamic susceptibility contrast MRI parameters. Perfusion parameters (CBF , CBV and MTT) estimated by application of dynamic susceptibility contrast MRI.

DSC-MRI is less complicated than DCE-MRI. A priori assumptions about interactions between multiple tissue compartments before fitting the model equations to the measurement data are not necessary. Although some assumptions may have to be made in the measurement of the AIF and tissue response curve, to find CBF , the tissue response function (Eqn. 31), just needs to be deconvoluted [25, 73].

$$C_v(t) = CBF \cdot K \int_0^\infty C_a(\tau)R(t - \tau)d\tau \quad (31)$$

Here $C_v(t)$ and $C_a(t)$ are known functions, since they are the measured tissue contrast response curve inside the voxel and the AIF, respectively. CBF is the cerebral blood flow, K is a normalisation constant and $R(t)$ the residue function, i.e., the impulse response of the imaging voxel, a dimensionless function ranging between 1 and 0, determining what happens to the contrast $C_a(t)$ entering the imaging voxel. $CBF \cdot K$ and $R(t)$ are unknowns and consequently the parameters that must be fitted in the deconvolution process [73]. In practice, relative cerebral blood flow ($rCBF$) is usually the estimated parameter.

Singular value decomposition (SVD) has become a popular approach to deconvolution in DSC-MRI [74]. The tissue response curve and arterial input function are measured at equally spaced discrete time points and Eqn. 31 can be rewritten as a matrix equation, Eqn. 32, or shorthand Eqn. 33.

$$CBF \cdot \Delta t \begin{pmatrix} C_a(t_1) & 0 & \dots & 0 \\ C_a(t_2) & C_a(t_1) & \dots & 0 \\ \dots & \dots & \dots & \dots \\ C_a(t_j) & C_a(t_{j-1}) & \dots & C_a(t_1) \end{pmatrix} \begin{pmatrix} R(t_1) \\ R(t_2) \\ \dots \\ R(t_j) \end{pmatrix} = \begin{pmatrix} C_v(t_1) \\ C_v(t_2) \\ \dots \\ C_v(t_j) \end{pmatrix} \quad (32)$$

$$A \cdot \mathbf{b} = \mathbf{c} \quad (33)$$

Given that $R(0) = 1$, the equation may be solved iteratively. But the method is sensitive to noise, and while one could add a regularization term [75], the SVD approach is often preferred instead. With SVD the inverse of A is diagonalised and Eqn. 33 is solved in terms of the diagonalization, where the elements in the diagonal matrix that are above a certain threshold are set to zero, thereby reducing noise [76].

CBV is proportional to the area under the contrast curve. If one could divide by the amount of contrast present in an ideal voxel containing only blood, one would have a measurement in terms of a fraction of a voxel. The size of a voxel is known and the amount of contrast in an ideal voxel is taken to be the arterial input function. Thus, relative cerebral blood volume $rCBV$ can be calculated according to Eqn. 34 [25, 73],

$$rCBV = \frac{\int_0^t C_v(\tau) d\tau}{\int_0^t C_a(\tau) d\tau} \quad (34)$$

where $C_v(t)$ is the tissue contrast response curve and $C_a(t)$ is the arterial input function. MTT is related to CBF and CBV by the central volume theorem [58], Eqn. 35.

$$MTT = \frac{CBV}{CBF} \quad (35)$$

1.3.3 Arterial input functions

Until now it has merely been stated that an AIF is needed to perform DCE- and DSC-MRI, and its place in the perfusion parameter estimation equations has been described. These equations alone should indicate that an accurate AIF measurement is critical to achieve accurate perfusion parameter estimations, and experiments have confirmed it [71, 77]. Because there will always be a trade-off between various quality aspects of an AIF measurement [78, 79], a plethora of measurement and approximation techniques have been developed and are widely applied.

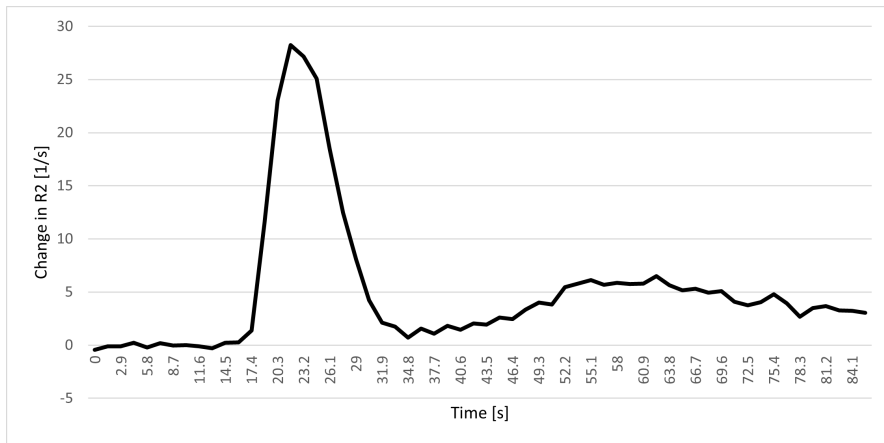


Figure 10: An arterial input function (AIF). Typically, an AIF exhibits an early signal rise, small width and a high peak.

Local and global AIFs

AIFs are meant to be a measurement of the contrast agent concentration flowing into the region of interest (ROI). A local AIF measurement close to the ROI would therefore seem intuitive [80]. It has been shown that when this is not the case, delay and dispersion of the AIF can lead to an underestimation of *CBF* [81, 82]. However, delay can be corrected for by applying an appropriate deconvolution method [76], and to some degree, so can dispersion [75]. Dispersion can also be reduced by the choice of local AIFs [83]. Saline injection following the contrast agent administration is standard protocol, regardless of whether a global or local AIF is chosen, and part of its effect when administered properly is to shorten *BAT*, increase initial steepness, maximum intensity, and maximum intensity duration of the signal [84, 85]. Tissue surrounding the measurement vessel can contribute to the AIF signal. These are partial volume effects that occur when the vessel is smaller than the imaging voxel. Local AIFs are often measured in small vessels close to the ROI. While global AIFs can be measured in large feeding arteries rendering partial volume effects less pertinent, they too are susceptible to partial volume effects [86, 87].

Scan-specific, subject-specific, and population-based AIFs

AIFs can be categorised as scan-specific [88–95], subject-specific [94–96], or population-based [88–94, 96]. Like the name suggests, scan-specific AIFs are extracted from individual study scans and may consequently do better justice to AIF variations between scans than subject-specific and population-based AIFs [93]. Hence, they could potentially also render more accurate perfusion parameter estimations. However, single measurements may cause poorer repeatability of subsequently derived perfusion parameters than do averaged AIFs [92], and unless an automated AIF search algorithm is applied, scan-specific AIFs can be somewhat more labour demanding than applying a population-based AIF.

An AIF is subject-specific if it is applied for parametric perfusion modelling based on data acquired from repeated study scans of the same subject. The AIF may for instance be the scan-specific AIF from the first-time scan of a patient, used repeatedly on subsequent data collected from follow-up scan sessions [94–96].

A population-based AIF can be calculated from a random subset of the patients in question, temporally aligning the set of AIFs and then computing the median or average [97]. The mean population-based AIF could be applied straight away, or it could be fit to a parametric model AIF (not to be confused with the main DCE or DSC parametric modelling) before application. Numerous AIF models exist [59, 82, 97, 98]. Among AIF modelling methods, the Parker model, originally proposed for abdominal MRI, is probably the most famous, and was designed to be applied to population-based AIFs [97]. Sometimes, like in the NordicICE software (NordicNeuroLab Inc., Bergen, Norway) one can choose a population-based model AIF, first developed by van Osch et al. [99], based on physiological data from a typical 35-year old male. In such cases, the population-based AIF is independent of the subjects in the actual data being analysed. Population-based AIFs are easy to apply, but individual variations are often disregarded [93, 100].

The choice between scan-specific, subject-specific, and population-based AIFs may depend on the application. For DCE-MRI studies, some authors argue for population-based AIFs when imaging the head and neck area [92]. When imaging the prostate cancer, more accurate perfusion model output has been achieved using a scan-specific AIF [88], though in predicting biopsy outcome scan-specific AIFs were not found to be better than population-based AIFs [91]. Others have claimed diagnostically accurate perfusion analysis with population-based AIFs in the prostate [89]. In studies of DCE-MRI parameters in brain tumours, scan-specific AIF measurements have been recommended [93]. In DSC-MRI, scan-specific and automated AIFs are by far the most commonly applied AIFs, probably because the temporal resolution relative to DCE-MRI is high, such that measurements of scan specific AIFs are less noise ridden. Nevertheless, though research addressing choice of AIFs in DSC-MRI is scarce, preferences for scan- or subject-specific AIFs in brain tumour patients have been reported [94–96].

Automated and semi-automated AIFs

Both automated and semi-automated AIF search algorithms are being used in perfusion MRI studies [101–105]. The AIF detection algorithms look for voxels that display contrast signal curves with a high maximum, small width, and an early signal rise [77, 106–110]. Several automatic AIF selection methods are based on clustering algorithms, an example is provided by Mouridsen et al. [108]. Mouridsen et al. [108], describe a k-means clustering approach which is implemented in NordiICE (NordicNeuroLab Inc., Bergen, Norway). They argue that the Euclidean distance between vectors describing contrast curves originating from different tissue should be large compared to contrast curves originating from similar tissue. Assuming equal contrast concentrations across the arteries, the contrast curves were normalised to have the same area under the curve prior to k-means clustering. K-means clustering minimises the inter cluster variance, and maximises the intra cluster variance. K-means clustering was performed a second time on the AIFs contained in the cluster with shortest arrival time and a final AIF was chosen by computing the mean of the shortest arrival time AIFs in the second clustering [108].

Semi-automatic AIF search algorithms have traditionally involved the selection of a search region [108, 111–113], and applied algorithms typically identify voxels experiencing early arrival and maximum peak contrast agent concentrations within these regions [77, 80, 109, 110]. A set of suitable AIF candidates can be displayed by an applied software, and the user may then choose which ones to apply in the perfusion analysis, or perform other minor adjustments [105]. This allows a user-controlled experiment, though it can also add a level of subjectivity to the measurements [112]. AIFs can also be simulated by applying the method of mean tissue response. Mean perfusion parameter values of one or more healthy tissues are assumed to be known, and an AIF can then be calculated inversely and applied to the ROI [114, 115]. An obvious limitation of the method is that the subject may not be normally perfused, for example in the case of brain tumours, healthy appearing tissue may be affected by the disease [116, 117].

1.4 Diffusion weighted imaging

An important method of probing tissue microstructure with MRI are diffusion measurements and reconstruction of maps that reflect aspects of tissue diffusivity. Diffusion is the random motion of micro-molecules. In the diffusion measurement context, the motion of spin possessing molecules is modelled as Brownian motion [118], where there is no preferred direction of flow or change in concentration of molecules. The motion of individual spins is characterised by random fluctuations in position, such that individually traced out paths appear as random walks (Fig. 11). These random walks can be hindered by tissue structures. The goal of diffusion measurements is to make inferences about the tissue structure, based on the collective contributions, or rather lack thereof, of diffusing spins to a measurement signal.

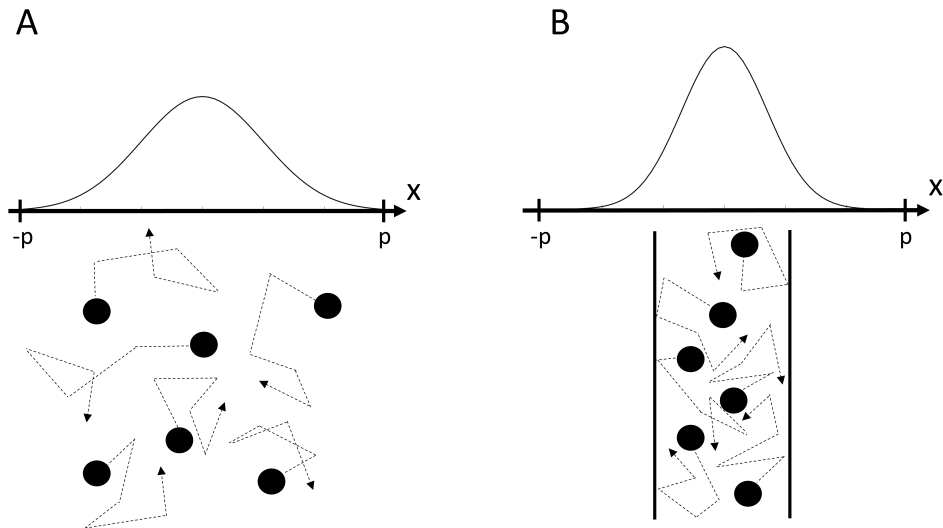


Figure 11: Free and restricted Brownian motion. The average displacement of diffusing water molecules, characterised by their random Brownian motion, is reduced by restrictions, such as for example tissue boundaries.

1.4.1 Measuring diffusion and constructing diffusion tensors

To measure diffusion, is to measure the amount of signal attenuation caused by a set of de-phasing and re-phasing gradients that are added to the imaging sequence (Fig. 12). These were introduced by Stejskal and Tanner [28]. The de-phasing gradient causes spins at different locations to experience different amounts of phase shifts. When the re-phasing gradient is applied, the spins at the different locations will have their phase shifts reversed and returned to base. Spins that in the meantime have moved relative to the surrounding

spins will not experience equal amounts of phase shifts in both directions. Therefore, they contribute to signal loss compared to spins with none or shorter net displacement in the direction of the applied de-phase and re-phase gradients. The amount of signal loss is dependent on the gradient amplitude, the gradient duration, and the time interval between gradients. These are parameters that can be controlled in the experiment. Lastly, the signal attenuation is dependent on the diffusion constant D of the diffusing substance, that is, the particle flux through an area per time. The diffusion constant is the target variable of the measurements necessary for diffusion tensor imaging (DTI).

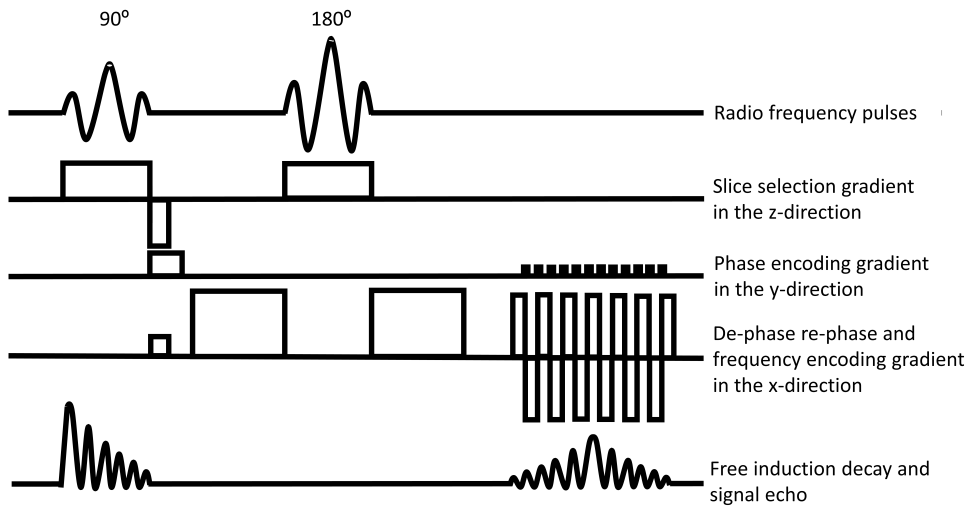


Figure 12: The Stejskal-Tanner sequence. Diffusion signal attenuation can be measured with the Stejskal Tanner sequence. The de-phasing gradient ensures that spins at different locations along the gradient acquire different amounts of phase shifts. Non-moving spins will have their phases returned to base by the re-phasing gradients. Since moving spins do not have equal phase shifts in both directions, they contribute to a signal loss compared to a non-diffusion sensitised image.

The diffusion constant D has units mm^2/s , as can be seen again from Fick's first law of diffusion (Eqn. 36),

$$J = -D\nabla c \quad (36)$$

which states that the particle flux J is proportional to the negative gradient of particle concentration c . ∇ refers to the gradient in spatial dimensions. Applying the rule of mass conservation (Eqn. 37), for a constant diffusion coefficient D one arrives at Fick's second law [119] in the form of Eqn. 38, which when $\partial c/\partial t = 0$ describes cases where the particle concentration does not change with time, as is the case with Brownian motion.

$$\frac{\partial c}{\partial t} = -\nabla J \quad (37)$$

$$\frac{\partial c}{\partial t} = D\nabla^2 c \quad (38)$$

Fick's second law has the form of the heat equation, with the fundamental solution given by the Gaussian kernel (Eqn. 39), which can also be expressed with reference to Einstein's formula (Eqn. 40), [27].

$$P(x, t) = \frac{1}{\sqrt{4\pi Dt}} e^{-\frac{x^2}{4Dt}} = \frac{1}{\sigma\sqrt{2\pi}} e^{-\frac{x^2}{2\sigma^2}} \quad (39)$$

$$\sigma = \sqrt{2Dt} \quad (40)$$

$P(x, t)$ is the probability to find a spin at a particular point in space in time, σ is the mean displacement, D is the diffusion constant and t is the diffusion interval.

The phase difference for a single spin at a specific point in space and time $\phi(x, t)$ with reference to a chosen base line point is given by Eqn. 41,

$$\phi(x, t) = e^{\int i\gamma G(t)tx} \quad (41)$$

where γ is the gyromagnetic ratio and G is the applied de-phase or re-phase gradient pulse.

The total measurement signal is the sum across phase differences originating from points in space and time, weighted by the probability to find the spins at said position [28, 120], and scaled by a minimally diffusion weighted baseline image (Eqn. 42),

$$S = S_0 \int_t \int_x P(x, t) \phi(x, t) dx dt \quad (42)$$

S and S_0 are the total measurement signal and the baseline signal, respectively. In the limit that the gradients are applied instantaneously, i.e., have a rectangular shape, Eqn. 42 can be solved, to yield Eqn. 43, which is re-stated in exponential form in Eqn. 44.

$$\ln S = S_0 - \gamma^2 G^2 \delta^2 \left(\Delta - \frac{\delta}{3} \right) D = \ln S_0 - bD \quad (43)$$

$$S = S_0 e^{-bD} \quad (44)$$

where Δ is defined as the time interval between the onsets of the de-phase and re-phase gradients, δ is the time interval for which the gradients are switched on, and b collects

the experiment-controlled variables into one parameter. Accordingly, there is a linear relationship between the b -value and the logarithm of the measured signal. A minimum of two measurements is required to compute the slope D , which, in an ideal world, is the diffusion constant.

Eqns. 43 and 44 only provide information about diffusion in the direction that the de-phase and re-phase gradients were applied. In addition to the non-diffusion weighted images, measurements of the diffusion constant D are required in a minimum of six directions to uniquely determine the magnitudes and directions of three orthogonal diffusion vectors, defining an ellipsoid [121]. The information contained in the six diffusion constant measurements are stored in a three-by-three symmetric diffusion tensor $\overline{\overline{D}}$, such that its eigenvectors are unit vectors corresponding to the orientation of the principal axes of the ellipsoid and its eigenvalues correspond to their length [122–124]. The diagonal elements of the diffusion matrix contain the diffusion constants D_{xx} , D_{yy} and D_{zz} , which are a measure of diffusion in the x -, y , and z -direction, respectively. To determine the diffusion tensor, Eqn. 43 is modified to a system of equations, each of which are in the form of Eqn. 45,

$$\ln S_i = \ln S_0 - b \hat{g}_i^T \overline{\overline{D}} \hat{g}_i \quad (45)$$

where \hat{g}_i is the unit vector in the direction of the applied de-phase and re-phase gradients of the measurement number i , S_i . To reduce noise, additional diffusion directions are oftentimes applied, and Eqn. 45 is solved with multi-variate linear regression.

1.4.2 The apparent diffusion coefficient and noise

There are several effects beyond diffusivity that affect signal attenuation. Therefore, instead of measuring the diffusion constant D , what is really measured is the apparent diffusion constant (ADC). Signal attenuation effects can be inherent to the tissue that is probed [125–127], due to motion and misregistration [128–130], and depend on the exact timing and interplay of the pulses applied in the measurement [131].

The Gaussian diffusion probability distribution is an approximation, precisely because the tissue microstructure restricts diffusion, such that the diffusion probability curve is less heavy tailed than the Gaussian distribution, causing a lower ADC than otherwise expected. The level of kurtosis introduced this way varies depending on the tissue and is more pronounced at higher b -values (Fig. 13) [126]. At low b -values the effect of intravoxel incoherent motion becomes apparent, due to microcirculation in the capillary network mimicking true diffusion [41]. Signal attenuation increases, which causes an increased ADC . Additionally, general phase dispersion can be caused by susceptibility effects [127], also contributing towards signal loss and a higher than expected ADC .

DWI requires long TR (~ 2000 - 5000 ms) [132] to reduce T1 effects. Ideally, T2 effects should also be minimised by short TE . However, the gradient amplitudes are limited and require the de-phasing and re-phasing gradients to be switched on for some non-infinitesimal time prior to sampling of the echo signal, necessitating somewhat longer TE

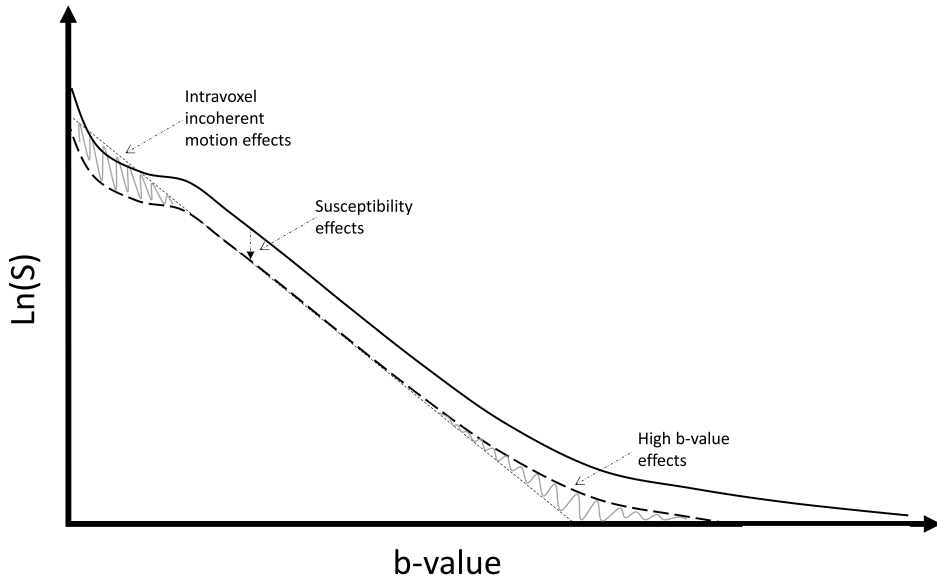


Figure 13: Diffusion signal across b-values.⁴ Signal attenuation (S) may increase at low b-values due to intravoxel incoherent motion, and across b-values due to susceptibility effects and phase dispersion. At high b-values the signal attenuation can deviate toward slightly lower signal attenuation than the straight line in the logarithmic plot would predict.

(~ 80-160 ms) [132, 133]. As discussed, calculation of the diffusion tensor presupposes that diffusion weighting is applied in at least six directions, and when multi-shell imaging is performed the amount of collected data scales with the number of b -values. Consequently, rapid image readouts are necessary, but even when these are applied, as a rough rule of thumb, one can acquire ten DWI volumes per minute, during which time the subject has ample opportunity to move. Diffusion measurements are extremely sensitive to motion, because of for example cardiac pulsations, respiration, and subject movement [128, 129]. Whenever spins move due to other mechanisms than diffusion, it can cause both additional phase dispersion and signal attenuation, as well as misregistration of the signal, oftentimes recognised as ghosting [130]. Ghosting effects appear with movement along the phase encoding direction such that image readout lines are shifted. The effects become more severe with stronger gradients.

⁴By courtesy of Allen D. Elster, MRIquestions.com, Fig. 13 is adapted of a version available at <https://mriquestions.com/diffusion-kurtosis.html> (visited 01/02/2022).

Single shot echo planar imaging (EPI) is the most common acquisition strategy for the necessary fast diffusion image readout [131], but it is also liable to image distortions. It is characterised by small blips in the phase-encoding gradient and large rapid oscillations in the frequency-encoding gradient [134, 135]. EPI acquisitions must be corrected for chemical shifts, particularly in the phase-encoding direction. Spins experience slightly differing fields due to different electron shielding effects in lipids and water, which causes them to have slightly different resonance frequencies. The frequency bandwidth per pixel is small in the phase-encoding direction and the phase difference is allowed to accumulate due to the single shot acquisition [130, 131]. Signal attenuation and the ensuing diffusion measurements are also affected by the acquisition scheme. Strong and fast shifting gradients can cause lingering fields inducing eddy currents that cause new random gradients which in turn affect signal attenuation [130]. Non-linearity of any applied gradient, as well as susceptibility artifacts, cause distortions in the image readout. Careful design of pulse sequences [131], and quality checks and calibrations of the scanner gradients [136], can help alleviate some of these issues.

1.4.3 Indices and directionality

The information stored in the diffusion matrices, i.e., the lengths and directions of the principal axes of a modelled ellipsoid, may need to be visualised and interpreted. By far the most common scalar contrasts that can be calculated are mean diffusivity (MD), Eqn. 46 and fractional anisotropy (FA), Eqn. 47.

$$MD = \frac{\lambda_1 + \lambda_2 + \lambda_3}{3} \quad (46)$$

$$FA = \frac{\sqrt{((\lambda_1 - \lambda_2)^2 + (\lambda_2 - \lambda_3)^2 + (\lambda_3 - \lambda_1)^2)}}{\sqrt{2(\lambda_1^2 + \lambda_2^2 + \lambda_3^2)}} \quad (47)$$

Here λ_1 , λ_2 , and λ_3 correspond to the longest, middle, and shortest lengths of the principal ellipsoid axes. MD intuitively corresponds to the mean ADC across the three dimensions of the ellipsoid, which is also equal to the trace of the diffusion tensor divided by three [122–124, 137]. Other ways to measure anisotropy exist, though FA as rendered in Eqn. 47 is most common. Regardless of which anisotropy measure that is chosen, anisotropy will usually range between 0 and 1, quantifying the ellipsoid shape such that a value closer to zero indicates that the ellipsoid approaches spherical shape.

Care must be taken when interpreting scalar MD and FA maps. Both MD and FA are susceptible to partial volume artefacts [138], and are consequently both somewhat dependent on voxel size. This is particularly true for FA , as disorganised fibres within a voxel can cause reduced FA [139]. Smaller voxel sizes can therefore induce over-all higher measured FA . FA also does not distinguish between tubular ellipsoids and ellipsoids that have a disc-like shape, and so there could be not just one, but multiple main diffusion directions within the same voxel. Nevertheless, FA contrasts are proven to be

of clinical value for investigating disease and treatment effects in, e.g., multiple sclerosis [140], stroke [141, 142], and cancer [116, 143], where abnormal *FA* is often interpreted as structural damage.

Tractography can be performed based on the principal eigenvectors within a voxel. The aim is to reconstruct a map of possible fibre tract trajectories in the brain. In deterministic fibre tracking, starting at user defined voxels, streamlines can be traced out following the principal eigenvectors between neighbouring voxels [144]. Another approach to fibre tracking includes the computation of the amount of anisotropic spins diffusing in a particular direction, using high resolution diffusion imaging [145]. In that case, steps in the tracking algorithm can include filtering out noise by thresholding the magnitude of possible fibre orientations within the voxel, and if there are more than one possible tracking direction within the voxel, the direction forming the smallest tract turning angle should be selected [145]. To practically perform fibre tracking, several tracking parameters, such as seed regions (i.e., starting voxels), minimum and maximum lengths of tracts, angular thresholds between fibre orientations in neighbouring voxels, as well as a minimum *FA* threshold need to be supplied. In addition to the concerns that accompany the interpretation of *FA* maps, the method of tract propagation and interpolarisation between neighbouring voxels and user set parameters contribute to uncertainties in the tracking [146].

1.4.4 Free water elimination

There are two main motivations for performing FW correction in the post processing steps of DWI. Firstly, the large water content in the cerebral spinal fluid (CSF) and large fibre tracts may cause partial volume effects at the edges of these areas [138, 147]. Without FW corrections *MD* at edge locations may be overestimated, and *FA* underestimated, due to the isotropic diffusion component characteristic of FW. Secondly, there are many conditions causing increased local vascularity or oedema [148, 149]. To better characterise these conditions, it may be helpful to remove FW signal contributions, such that the tissue structure at oedematous sites can be better investigated. While fluid-attenuated inversion recovery (FLAIR) DWI can suppress the CSF signal [150, 151], it may be unreliable in correcting oedematous fluids due to the fluid composition [148, 152, 153], it does not allow periodic motion correction [154], and is not applied in the clinic nearly as often as the classic single shot EPI sequence. Superiority of FW corrected DWI over FLAIR DWI has been experimentally verified in the Fornix [153].

FW correction with a two-compartmental tissue model was first proposed by Pierapoli and Jones [155] (Eqn. 48), where each voxel is assumed to have a compartment containing freely diffusing water, and one compartment where diffusion is restricted. There is assumed to be no exchange between the two compartments.

$$S_{2C} = S_0 \left(f e^{-bD_{FW}} + (1-f)e^{-bD_R} \right) \quad (48)$$

$$S = S_0 e^{-bD_{TOT}} \quad (49)$$

S_{2CM} , S , and S_0 are the diffusion weighted two-compartmental, single-compartmental measured, and minimally weighted signal, respectively. FW diffusion is isotropic and has a diffusivity most commonly set to $3.0 \cdot 10^{-3} \text{ mm}^2/\text{s}$. The FW compartment diffusion tensor D_{FW} is therefore known a priori. D_{TOT} is the naïvely measured diffusion tensor with no correction applied, incorporating the entire diffusion signal into the matrix. The remaining variables are fractional water volume f and the restricted diffusion tensor D_R . These are unknown parameters and must be found by fitting Eqn. 48 to diffusion measurements. Though prolonging scan times and ignoring that a single diffusion exponent may no longer perfectly fit the measured diffusion data, Pierapoli and Jones [155], suggested performing the bi-compartmental measurement with multiple b -values.

For any fractional water volume f there is a solution D_{FW} that minimises the difference between S_{2C} and S in Eqns. 48 and 49. This implies an infinite number of possible problem solutions [156]. Pasternak et al. [157] therefore added extra constraints on the solution in the form of a Laplace-Beltrami regularization [158]. This ensures piecewise smoothness in the restricted diffusion tensor across tissue voxels [159]. The range of solutions was also narrowed down by putting limits on f based on minimum and maximum expected signal attenuation in the tissue compartment [157]. This FW correction method [157], is applied in the current study, however the Laplace-Beltrami regularization is exchanged for a Euclidean metric [160], multiple b-shells are included, and as part of the initialization of the diffusion tensor an MD of $0.6 \cdot 10^{-3} \text{ mm}^2/\text{s}$ was assumed.

Several other FW correction methods have, as is one of the goals in this thesis, examined the effects of FW corrections in patients with cerebral glioma [161–167]. These FW correction methods include a new fractional FW volume initialization for single-shell acquisitions [161], deep learning algorithms [162–164], filtered tractography [165, 166], and restriction spectrum imaging [167]. Most of these studies focus on fibre tract reconstructions, and the consensus is that incorporating FW corrections allows more fibre reconstructions in peritumoral areas than non-corrected diffusion measurements do [161, 162, 165–167]. Others suggest the analysis of FA maps to describe tumour infiltration in the oedematous regions [163, 164].

1.5 Aims

The main focus of this thesis is to help establish perfusion and diffusion measurement MRI methods in important clinical applications where they may provide a substantial added value. Conventional clinical MR imaging is to a large extent based on structural images and is usually interpreted qualitatively. While structural imaging provides invaluable geometric and anatomical information when assessed by radiologists, there is much relevant information that may not be available at such a macroscopic level. New disease relevant information can be obtained from measures of physiological processes. It has been shown that in several applications, these measures can be early markers of disease severity or effects of treatment [168–171].

This study is motivated by clinical questions pertaining to diagnosis and measuring treatment effects in selected patient groups in which inflammatory processes are involved in the disease. With conventional structural MRI, it can be difficult to detect inflammation related to arthritis, to predict outcome after radiosurgery of brain metastases, to assess glioma quantitatively or to assess possible tumour infiltration. An overarching goal of this research is to be part of the current scientific development, where advanced MRI methods are developed in relation to the potentially heterogeneous nature of the underlying disease.

1.5.1 Optimisation of perfusion measurements to evaluate juvenile idiopathic arthritis in the temporomandibular joint

JIA is defined as arthritis of unknown origin, with a chronic persistence for a minimum of six weeks and onset prior to the 16th birthday [172]. While the reading of post contrast injection structural MR images is common in the evaluation of JIA in the TMJ [173, 174], there is still no consensus regarding the diagnostic method. There is a wide range of methods for JIA detection in the TMJ, [21, 173–177]. There is also a range of reported disease prevalence (0.7 - 40 %) [22], reported continuation of the disease into adulthood (41 - 67 %) [178, 179], and reported TMJ involvement in JIA (35 - 87 %) [21, 173, 175, 180]. Both differing diagnostic procedures and asymptomatic TMJ may contribute to lack of early therapeutic interventions [21–23]. It has been hypothesised that JIA causes an inflammation in the TMJ, hallmarked by increased vascularity [149, 181]. DCE-MRI may therefore lend itself as a tool for assessment of the microvasculature in the TMJ.

In the paper *Effects of Motion Correction, Sampling Rate and Parametric Modelling in Dynamic Contrast Enhanced MRI of the Temporomandibular Joint in Children Affected with Juvenile Idiopathic Arthritis*, effects of DCE-MRI acquisition and post processing methods on physical parameter estimations from dynamic data is investigated. The paper aims to provide a framework for DCE-MRI data processing methods to ensure that future evaluations of DCE-MRI as a possible diagnostic tool for JIA affected TMJ can be performed with parameter estimations of best attainable quality. To this end, DCE-MRI data with high temporal resolution (4 s) were acquired from 73 children with JIA. Three levels of motion correction were applied to the dynamic data, which was also down sampled,

mimicking a poorer temporal resolution. Additionally, the patients were stratified into two groups based on parameter estimations computed with several two-compartmental models; the 2XCM [62, 63], AATH [65, 67], DCATH [68], and GCTT [69] models. The groups were compared to one another, as well as to stratifications of the patients based on three radiologists' assessment of post contrast structural MR images.

1.5.2 Choice of arterial input functions

DSC-MRI relies on, and is sensitive to the measurement of an AIF for estimation of perfusion parameters [71, 77]. Care should be exercised to measure an adequate AIF. There are several examples of AIF selection methodologies that have been developed in response [182–185]. Clinical studies are often limited by the number of patients available to a research site, though there seems to be a move toward increased data sharing [186–190]. In order to estimate comparable quantitative perfusion parameters longitudinally and across sites, post-processing pipelines including a protocol for AIF measurements should be of interest.

In the paper *Arterial Input Functions in Dynamic Susceptibility Contrast MRI (DSC-MRI) in Longitudinal Evaluation of Brain Metastases*, various AIFs are applied to estimate DSC-MRI parameters in a longitudinal data set. Scans were performed approximately every three months in the follow-up schedule of 8 patients with brain metastases. The AIFs were selected using both fully automated and semi-automated algorithms, with various selection criteria. Scan-specific and subject-specific AIFs, as well as AIFs mimicking population-based AIFs were selected. The paper aims to investigate AIF selection criteria for use in longitudinal DSC-MRI assessment of brain metastases.

1.5.3 Perfusion measurements prior to stereotactic radiosurgery to predict outcome in brain metastases

Metastatic spread to the brain is estimated to happen in 5.6 – 9.6 % of cancer patients [191–193], and SRS is a primary treatment strategy of brain metastases [194–196]. Following treatment, apparent tumour volume may increase, either due to true disease progression or to pseudo-progression [18]. Using only structural images it is difficult to differentiate these states at an early stage [19, 20], complicating outcome predictions after SRS. So far, pretherapeutic DSC-MRI parameter estimates have not always been reported to correlate with SRS treatment outcome [197–199].

In the paper *Dynamic Susceptibility Contrast MRI May Contribute in Stereotactic Radiosurgery Outcome Prediction in Brain Metastases* 32 patients are characterised with either progressing or non-progressing brain metastases at some point after SRS. The paper aims to investigate whether DSC-MRI parameters obtained from within contrast enhancing ROIs prior to SRS treatment are helpful in predicting outcome after SRS treatment. Statistical testing was performed to evaluate whether the estimated perfusion parameters can help distinguish between patients that likely have poor survival or progressive disease from those that are likely experiencing pseudo-progression or regression.

1.5.4 Free water diffusion corrections applied to detect heterogeneity in glioma

Among primary tumours, of malignant brain and central nervous system tumours, glioma account for 81 % of malignant cases [200, 201]. The proportion of cured patients has been estimated to 7.9 % [202]. Evaluations of DTI derived contrasts in imaging glioma disagree between studies [203–206]. Motivating free water elimination is the fact that reduction in FA can be caused both by isotropic diffusion signals, as well as tumour infiltration of white matter tracts [116, 117]. In conventional DTI, these effects may be difficult to differentiate [207].

In the paper *Effects of Multi-Shell Free Water Correction on Glioma Characterization*, the aim is to test whether multi-shell DTI can increase the amount of information contained in the FW maps and FW -corrected FA (FAt) maps. The FW elimination method developed by Pasternak et al. [157], involving multiple shells, including low b -value shells, was applied to data acquired from 26 glioma patients. Summary variables were computed from the constructed FW and FAt maps, and their ability to characterise tumours was tested.

2 Methods

Four papers are presented in this thesis, based on data collected in three groups of patients with three different diseases. Although separate entities, these diseases all involve inflammatory processes. Three advanced MRI techniques were applied to access physiological processes on a microvascular and microstructural level (Fig. 14).

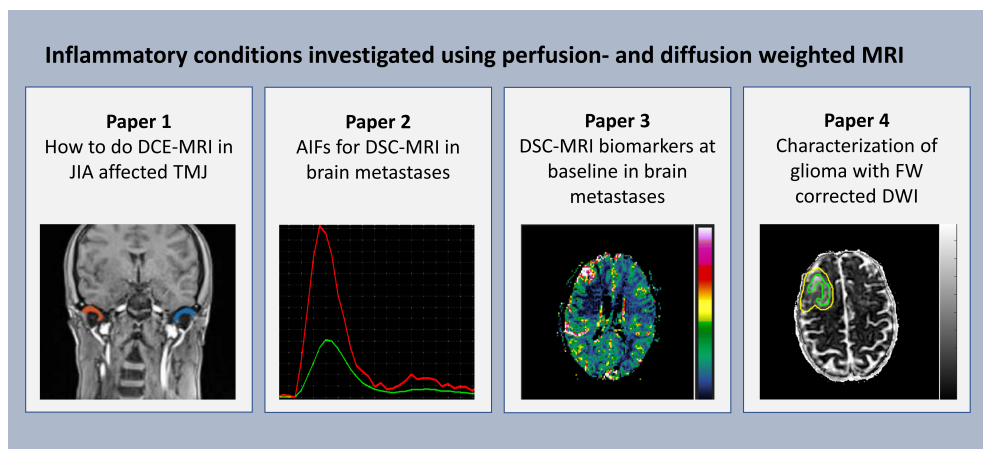


Figure 14: Paper 1 investigates acquisition parameters in dynamic contrast enhanced (DCE)-MRI of the temporomandibular joint (TMJ) with possible involvement of juvenile idiopathic arthritis (JIA). Paper 2 investigates choices of arterial input functions (AIFs) in dynamic susceptibility contrast (DSC)-MRI in brain metastases. Paper 3 investigates DSC-MRI perfusion parameters in relation to outcome after stereotactic radiosurgery in brain metastases. Paper 4 applies free water (FW) corrected diffusion MRI to characterise glioma.

2.1 Data collection

2.1.1 Patients and clinical scores

Written and informed consent to participation in the studies were given by all patients or their caretakers if the patients were younger than 12 years. All data were acquired in agreement with ethical approvals of either REK Vest or the NRES Committee of East England, Cambridge 2. Table 3 summarises the patient cohorts. Radiological image scores reflecting likelihood of JIA affected TMJ, and tumour gradings of glioma were performed by expert radiologists.

2.1.2 MRI protocols

Data collection parameters are summarised in Table 4.

	Paper 1	Paper 2	Paper 3	Paper 4
Disease	Juvenile Idiopathic Arthritis (JIA)	Brain metastases	Brain metastases	Glioma
Study type	Retrospective cross-sectional	Retrospective longitudinal	Retrospective longitudinal	Retrospective cross-sectional
Number of patients	73 (30 M, 42 F) *	8 (2 M, 6 F)	32 (15 M, 17 F)	26 (11 M, 15 F)
Mean age (years)	12 ± 3	64 ± 14	67 ± 10	53 ± 18

*52 (27 M, 25 F) had temporomandibular joints scored for JIA.

Table 3: Summary of patient cohorts comprising disease, type of study, numbers, sex (M = male, F = female), and age.

2.2 Parameter extraction

2.2.1 Paper 1

ROIs covering the synovial TMJs were based on consensus among three expert paediatric radiologists and were drawn manually on the 5th imaged volume after acquisition start. Contrast time curves were extracted from these ROIs by computing the average pixel signal value contained in the ROIs, and relative contrast enhancement curves were obtained by subtracting and dividing by the baseline signal. The relative contrast time curves were the bases for semi-quantitative perfusion parameters as described in chapter 1.3.1. Quantitative perfusion parameters were computed by implementing the AATH, DCATH, GCTT and 2XCM models in an inhouse developed MATLAB tool, version R2017a, (MathWorks Inc., Natick, Massachusetts, US). A population-based AIF was based on 22 random patients in the study. In a region containing the large brain feeding arteries, voxels with the highest signal peak were chosen to yield individual AIFs, these were temporally aligned by measuring and adjusting for the time between peaks. Finally, the median AIF was obtained and fitted and scaled according to the Parker model [97, 208]. As it is unlikely that JIA affected TMJ are symmetric in a patient [209], relative parameters, i.e., difference between parameters derived from the left and right TMJ divided by their sum, were calculated, and used for subsequent statistical analyses.

2.2.2 Paper 2 and Paper 3

Perfusion analysis was performed with NordicICE (NordicNeuroLab Inc., Bergen, Norway), using SVD to do the deconvolution [73]. Leakage correction was performed with a residue function approach and a parametric leakage fit [210]. Parameter maps were computed including $rCBV$, $rCBF$, and MTT maps. In each scan, 10 different AIFs were applied to perform perfusion analyses. The first two AIFs were scan-specific and fully automated, where one AIF was detected using unsupervised global detection in all slices,

	Paper 1	Paper 2	Paper 3	Paper 4			
MRI system	Magnetom Skyra*	Symphony Vision*	Symphony Vision*	Discovery MR750**			
Field strength	3 T	1.5 T	1.5 T	3 T			
Contrast agent	Gd-DOTA, Dotarem ***	Gd-DOTA, Dotarem***	Gd-DOTA, Dotarem***	-			
Kind of MRI	DCE-MRI	DSC-MRI	DSC-MRI	DWI			
Sequences	3D fast low angle shot	2D spin echo	2D gradient recalled echo echo planar imaging	2D spin echo	2D gradient recalled echo echo planar imaging	Inversion prepared fast 3D spoiled gradient recalled echo	Pulsed-gradient spin echo echo planar imaging
Image matrix	160 × 160 × 16 †	512 × 512 × 12	128 × 128 × 12 ‡	512 × 512 × 12	128 × 128 × 12 ‡	256 × 256 × 252	256 × 256 × 16
Slice thickness (mm)/spacing (mm)	2/2	5.5/7.2	5.5/7.2	5.5/7.2	5.5/7.2	1.5/1.5	2/4
Field of view (mm)	210 × 210	230 × 230	230 × 230	230 × 230	230 × 230	240 × 240	220 × 220
Repetition time (ms)	4	430	1450	430	1450	8.2	2000
Echo time (ms)	1	9.4	47	9.4	47	3.2	80
Inversion time (ms)	-	-	-	-	-	450	-
Flip angle (°)	9	-	-	-	-	-	-
b-values (s/mm ²)	-	-	-	-	-	-	0, 90, 150, 500, 1000
Diffusion directions	-	-	-	-	-	-	8

*Siemens, Healthineers, Erlangen, Germany, **GE Healthcare, Waukesha, WI

***Guerbet, Villepinte, France

† 60 volumes in time, 4 s sample rate, ‡ 60 volumes in time, 1.45 s sample rate

Table 4: Summary of MRI protocols including scanner name, field strength, type of MR image, applied sequence, resolution, sequence timings, flip angles, and parameters specific to diffusion imaging.

where voxels displaying an AIF-like shape were detected with a clustering algorithm [211], the second AIF was based on mean tissue response. The third and fourth AIFs were also scan-specific, where the AIF detecting clustering algorithm was applied in a user set ROI. One search region covered the circle of Willis. The other search region was placed in the hemisphere contralateral to the lesion. The fifth and sixth AIFs were patient-specific and defined identical to the already described semi-automatic scan-specific AIFs at the first scan in each patient. The seventh and eight AIF were two AIFs chosen among the scan-specific semi-automatically detected AIFs. They were chosen such that their mean height, full width at half maximum, time to peak and area under curve were close to the corresponding mean values in the scan-specific semi-automatically detected AIFs, thus mimicking population-based AIFs. The ninth and tenth AIFs were patient-specific and defined by calculating the means of the scan-specific semi-automatically detected AIFs. For Paper 3, only perfusion maps computed with the scan-specific semi-automated AIF with a search region placed over the circle of Willis were used.

Lesion volumes were drawn in the clinic for planning SRS. Though track was kept of the numerical representation of tumour volumes, the ROI maps drawn in the clinic were not available at time of analysis. Therefore, ROIs were redrawn using an inhouse algorithm based on subtraction of pre- and post-contrast T1-weighted images. Extraction of average perfusion parameters from ROIs was performed by aligning the perfusion maps to ROI masks based on structural T1 maps by way of slice-wise rigid translations performed in an inhouse script in MATLAB, version R2019b (MathWorks Inc., Natick, Massachusetts, US). Following an affine image registration scheme with the Elastix [212–214] command line tool, ROIs were defined by subtracting pre-contrast T1-weighted images from post-contrast T1-weighted images. The subtraction image was binarised by setting pixel-values below 5 % and above 80 % of maximum pixel value to zero, and remaining pixels to 1. Finally, guiding a manual segmentation in ITK-Snap, version 3.6.0 [215], the binary image was overlaid onto the post-contrast T1-weighted image. Volume estimations based on the new ROIs were found to be significantly correlated ($r(135) = 0.84, p < 10^{-37}$) to the volume estimations performed in the clinic (Fig. 15). Skull stripping, and white matter and grey matter segmentation was performed with FSL toolbox, version 6.0.1 [216–218].

In Paper 3 it was necessary to define the status of progressing and non-progressing disease. Definitions were based on the development of metastatic volume in time. Non-progression was defined as either continuous volume decrease (regression), and transient volume increase (pseudo-progression) taking place before a second SRS or death. Progression was defined as continuous or delayed volume increase prior to a second SRS or death. If death occurred prior to the first possible follow-up, this was also defined as progression.

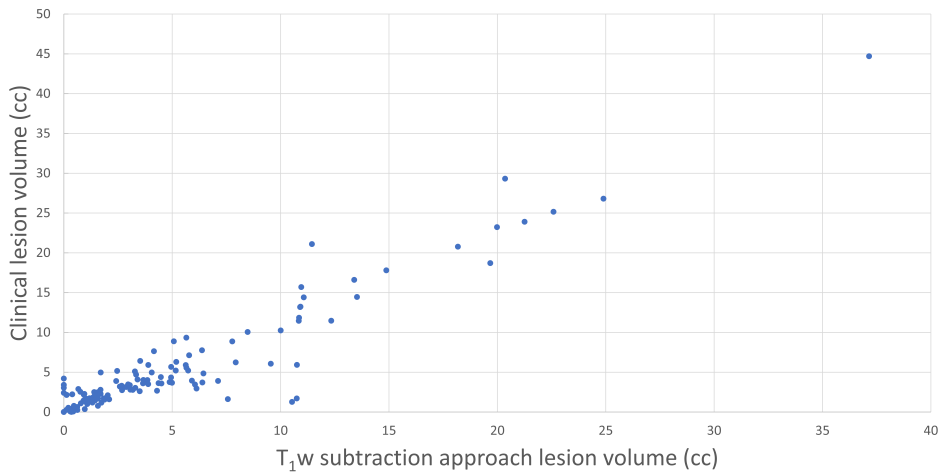


Figure 15: Correlation between region of interest volume estimates in metastatic brain tumours. Estimates were performed in the clinic and performed using an in-house T1-weighted subtraction approach.

2.2.3 Paper 4

In Paper 4, the FW-elimination algorithm developed by Pasternak et al. [157] was used. This method assumes two diffusion attenuation matrices, corresponding to two compartments within a voxel. The free water compartment is assumed to contain water diffusing isotropically at $3.0 \cdot 10^{-3} \text{mm}^2/\text{s}$. The other compartment contains the restricted water. Measuring diffusion, the sum of the contributions of these two attenuation matrices is measured, and the algorithm therefore minimises the distance between the measured attenuation and the attenuation caused by FW. Thus, the relative volumes of the water compartments are estimated. As an initialisation guess, non-CSF voxels are assigned an *MD* of $0.6 \cdot 10^{-3} \text{mm}^2/\text{s}$. A regularization term with a Euclidean metric [160] is added to provide piecewise smoothness between voxels.

Three parameter maps were produced: an *FW* map, an *FA* map, and an *FAt* map. The *FW* map and *FAt* map were computed by applying the FW corrected tensor fitting developed by Pasternak et al. [157] to multi-shell diffusion data (b-values 90 s/mm^2 , 150 s/mm^2 , 500 s/mm^2 , and 1000 s/mm^2). The non-corrected *FA* map was computed by performing regular tensor fitting with the FSL toolbox, version 6.0.1 (University of Oxford, UK) [216]. Using a normalised mutual information function and a 4th degree b-spline interpolation in SPM12, version 7771 (University College London, UK) [219], B0 images were registered to the T1-weighted images, and the transformation was applied to the parameter maps. ROIs, including total tumour volume, enhancing tumour volume, and necrotic tumour volume were drawn by an expert radiologist. Summary variables, comprising mean and variance, 25th and 75th quantile, median, skewness, kurtosis, and entropy, were extracted from the ROIs.

Additionally to the analysis presented in Paper 4, both FW-corrected and non-corrected DWIs were used to perform tractography at a b-value of 1000 s/mm^2 , using the DSI software [220]. 10,000 seeds were placed across the brain, an angular threshold of 90° was used, and only tracts between 10 mm and 60 mm were included. FW correction causes a shift in *FA* values across the parameter maps. Due to differences in optimal *FA* tracking thresholds several tracking thresholds were applied and compared based on resultant tract numbers, lengths, and irregularity (Equation 50) [221].

$$Irregularity = \frac{Area\ of\ Surface}{\pi \cdot Diameter \cdot Length} \quad (50)$$

The surface area is proportional to the number of tract surface voxels, length is calculated by summing over distances between coordinates representing the tract trajectory and taking their mean. Tract diameter is estimated based on tract length and volume, where volume scales with voxels covered by the tracts.

In regular fibre tracking a tracking threshold at $FA = 0.2$ is common [157, 161, 167, 222]. The shift in mean *FA* values after FW-correction was 0.07, and so fixed tracking thresholds of both $FA = 0.2$ and $FA = 0.27$ were applied. Additionally, another tracking

threshold was implemented using the Otsu threshold [223]. It is a method for binarising an image by maximising the intraclass variance between the upper and lower regions of the distribution that represents pixel intensities in the image (image histogram). Following the implementation in the DSI software package to filter out background voxels, where filtered out voxels are defined as those less than 0.6 times the Otsu threshold. The Otsu threshold has been successfully applied in several studies [221, 224–226].

The left Superior Longitudinal Fasciculus 3 was mapped in a single patient where this tract ran through an oedematous region, using a tractography as atlas implemented in DSI [206].

2.3 Statistical analyses

A significance threshold of $p = 0.05$ was chosen for all statistical tests involving p-values.

2.3.1 Paper 1

Three levels of motion correction (non-corrected, affine motion correction, and elastic motion correction) were compared by computing a least square fit (χ^2) between the motion corrected contrast concentration time curves and the pharmacokinetic model time curves. The effect of various levels of motion correction on relative pharmacokinetic parameters calculated with the GCTT model were compared using a one-way ANOVA test and Tukey's post hoc test. A paired sample t-test was used to compare low temporal resolution (8 s, 12 s, 16 s, and 20 s) semi-quantitative relative parameters to high temporal resolution semi-quantitative relative parameters. Both k-means clustering, and a random forest model were applied to group patients. Group sensitivities and specificities relative to diagnostic scorings based on structural MR images were computed. A two-way ANOVA test with Tukey's post hoc test was applied, where perfusion parameters (i.e., RT , M , S , A , F_p , E , ve , T_c , σ , BAT , and PS) and statistical group scorings were used as independent variables.

2.3.2 Paper 2

Standardised measurements describing the shape of a semi-automated scan-specific AIF were compared between each patient and the group mean, applying a one-sided t-test. Paired t-tests were used to test how well perfusion parameters $rCBV$, $rCBF$, and MTT calculated with 10 different AIFs, distinguished white matter and grey matter. Correlation coefficients between perfusion parameters in successive scans were calculated and ordered in matrices using a k-means algorithm, to form clusters of AIFs producing more similar perfusion parameters. Matrices containing Pearson's product moment correlation coefficient based p-values corresponding to the correlation coefficient matrices were also constructed, and adjustments for multiple comparisons were performed using the Bonferroni method.

2.3.3 Paper 3

Linear regression was applied to compare perfusion parameters $rCBV$ and $rCBF$ in patients defined as experiencing disease progression and non-progression. By way of ANOVA testing, it was tested whether several possible covariates (age, sex, lesion volume, two kinds of primary cancers, and dichotomised survival) and combinations of these, could improve a regression model free of covariates. Linear regression was also used to compare perfusion parameters between short survivors (survival < 60 days) and long survivors (survival > 60 days).

2.3.4 Paper 4

The effect of FW-correction on low-grade tumours (grade I and II) and high-grade tumours (grade III and IV) were compared by performing paired t-tests between FW-corrected (FA_t) and FA distributions. ANOVA testing with Tukey's post hoc test was applied to test whether neighbouring tumour volumes could be separated based on FW estimations and FA_t . A paired t-test was applied to FA_t and FA distributions derived from the various tumour volumes. p-values were adjusted for multiple comparisons using the Bonferroni method. To test how well FW-corrected data could correctly classify image voxels to the correct parts of the tumour, receiver operating characteristic (ROC) curves were calculated using a logistic regression model and labelled image voxels. Number of fibre tracts, their length, and irregularity [221] were compared using paired t-tests and several different FA tracking thresholds.

3 Results

3.1 Paper 1

Elastic motion correction provides a better least square fit to the GCTT model compared to non-correction and affine correction (Fig. 2 in Appendix A). Compared to non-correction, the percental improvement with elastic motion correction is 72 and 84 % in the left and right TMJ, respectively. With affine correction the corresponding percental improvements are 56 and 76 %. The applied pharmacokinetic models (AATH, DCATH, GCTT, and 2CXM) all leave comparable residues (Fig. 5 in Appendix A), with a relative standard deviation of 3.4 %.

With elastic motion correction, semi-quantitative relative parameters obtained with a simulated 8 s sample rate differ significantly from those obtained with a 4 s sampling rate. Disease relevant information may therefore be lost without a minimum 4 s sampling rate.

Parameters and group scorings (i.e., whether a patient's TMJ was likely affected by JIA or not) were used as categorical independent variables in an ANOVA test. Neither the parameters, nor the group interaction of the parameters with the group scorings significantly affected the values of the standardised relative parameters. However, group scorings did significantly affect the standardised relative parameters ($p = 1.0 \cdot 10^{-6}$).

3.2 Paper 2

Applying a range of AIFs causes much variability in the estimated perfusion parameters (Fig. 2 in Appendix B). Any of the applied AIFs can be used to differentiate between white matter and grey matter based on $rCBF$ ($p \leq 0.002$), but scan-specific AIFs should be used to differentiate between white matter and grey matter based on $rCBV$, ($p < 0.001$). However, if the top 1 % of $rCBV$ are taken out of the analysis, corresponding to implausible parameter estimations, patient-specific AIFs are also applicable ($p \leq 0.02$). Shape parameters of scan-specific AIFs suggest that AIFs sampled from the same patient at different time points may be more similar to one another than to AIFs sampled from separate patients (Fig. 4 in Appendix B).

3.3 Paper 3

Progressors had significantly lower $rCBV$ and $rCBF$ ($p \leq 0.01$) in the enhancing tumour volume at baseline and prior to SRS, than non-progressors, when patients with no follow-up were included in the analysis. Based on volume changes post SRS, 12 patients were labelled progressors, and 20 patients were labelled non-progressors. There were 13 regressors and 7 non-progressors with pseudo-progression among the non-progressors. Patients surviving for less than 60 days after SRS had significantly lower $rCBV$ ($p = 0.03$) than patients surviving longer than 60 days. There is a peak in $rCBF$ after SRS and prior to the transient volume increase in 5 of 7 pseudo-progressors (Fig. 4 in Appendix C). Of

the 25 patients with progressing or consistently regressing metastases, only 11 returned for more than two follow-up scans, and 5 returned for more than 3 follow-up scans.

3.4 Paper 4

The necrotic tumour region has a larger parameter mean and variance than other tumour regions (Fig. 2 in Appendix D). Mean FA and FW measurements from the enhancing, non-enhancing and total tumour regions do not differ significantly from one another. The area under the ROC curves separating necrotic tumour regions from enhancing regions based on FA estimations increased by 5 % after FW -correction. The effect of FW corrections on FA distributions differs in various tumour regions. In general, the FA distribution shifts toward higher FA values after FW -correction, but this is not the case in necrotic regions. Across tumour grades, the entropy of the FA distribution increases post FW -correction ($p \leq 0.003$). Skewness decreases ($p \leq 0.004$) in both low- and high-grade tumours, and kurtosis increases in high-grade tumours ($p < 0.001$). Tumour grade could not be significantly correlated to the mean of the parameters FW , FAt , and FA , nor to any of the distribution summary variables other than the mean (i.e., variance, 25th and 75th quantile, median, entropy, kurtosis, and skewness).

The various FA tracking stopping thresholds were used to perform whole brain tractography and the resulting statistics are shown in Table 5. The left Superior Longitudinal Fasciculus 3 was tracked in a patient where the tract ran through the oedematous region surrounding a grade IV tumour, (Fig. 16). 139 tracts were traced with FW -correction and an FA threshold of 0.27. Only 27 tracts were traced without FW -correction and an FA tracking threshold of 0.2.

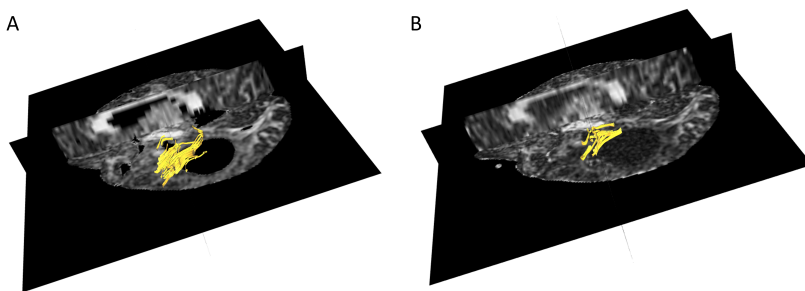


Figure 16: Fibre tracking in the left Superior Longitudinal Fasciculus 3. 139 tracts with FW -correction with an FA threshold of 0.27 (A). 27 tracts without FW -correction with an FA tracking threshold of 0.2 (B).

Otsu thresholds	Fixed $FA = 0.2$			Fixed $FA = 0.27$		
	Corrected	Non-corrected	p-value	Corrected	Non-corrected	p-value
Number of tracts	5600 ± 370	5500 ± 260	0.01	5500 ± 330	5400 ± 210	0.02
Mean tract length (mm)	28.2 ± 1.1	27.5 ± 1.1	0.008	27.9 ± 1.1	26.7 ± 1.3	< 0.001
Mean tract irregularity	37.0 ± 4.6	38.0 ± 5.2	< 0.001	35.4 ± 4.9	35.7 ± 5.3	0.08
				30.9 ± 4.6	31.2 ± 4.5	0.10
						< 0.001
						0.05

Table 5: Mean tract number, length, and irregularity with and without free water (FW) correction in whole brain tractography. Three fractional anisotropy (FA) thresholds were applied; individual Otsu thresholds and fixed FA -threshold at 0.2 and 0.27. The difference between the fixed FA thresholds corresponds to the distribution mean FA offset in FW corrected FA . Differences between tract number, length and irregularity in FW corrected and non-corrected data are statistically tested. p-values are calculated using a paired t-test and a significance threshold of $p = 0.05$. The final p-value column compares the tracking results in FW corrected data with an FA threshold of 0.27 to results in non-corrected data with an FA threshold of 0.2.

4 Discussion

Advanced MRI methods were applied to quantitatively assess MR data collected in patients with diseases that are difficult to diagnose or treat due to lack of quantitative diagnostic tools. A prerequisite for being able to use different modelling techniques is that the data basis is of a quality that enables the modelling to best approximate true measurements of potential disease-relevant parameters. Consequently, post-processing of the MRI recordings is important to achieve a sufficient image quality for the images to be used in the modelling. Image quality with respect to temporal resolution and motion correction of DCE-MRI recordings was studied in more detail in Paper 1. AIFs are also measurements that are part of subsequent perfusion estimates. AIF selections were studied in the context of DSC-MRI in Paper 2. Further, one must examine whether the output from the advanced models has clinical relevance. In Paper 3, lower perfusion parameters prior to SRS were associated with potentially less favourable outcome, and it was found that 5 of 7 pseudo-progressors had transiently increased $rCBF$ prior to transient volume increase. In Paper 4 the characterisation of glioma, in particular the necrotic tumour part, following FW estimation was explored.

4.1 Paper 1

There is no standard way to diagnose JIA in TMJ [21, 173–177]. With a sample rate of 4 s, we could investigate whether this high temporal resolution causes significant changes in semi-quantitative parameters (i.e., parameters describing the contrast response curve shape) in combination with different levels of motion correction. The contrast curve is also the starting point for the estimation of pharmacokinetic parameters, and we found that a high-level elastic motion correction made the model curves fit very well with the measured data. Many pharmacokinetic models have been developed. The papers that originally presented the AATH, DCATH and GCTT models [65, 67–69] are cited 128, 7 and 17 times, respectively, by papers that are available in PubMed, as of January 21st, 2022. In approximately 10 % of the papers citing these advanced models, they are applied to clinical DCE-MRI data [227–241]. In comparison, the extended Tofts model [24] is cited 1014 times and the 2XCM model [62, 63] 113 times by papers available in PubMed. An early comparison between pharmacokinetic models was performed by Buckley [242]. By modelling DCE-MRI data and subsequently fitting the Tofts and AATH models to the synthetic DCE-MRI data, he found that the Tofts model simulated the DCE-MRI data more reproducibly than the AATH model, and that the AATH model tended to overestimate PS and underestimate F_p at low flow or high permeability. Subsequently, others have also compared pharmacokinetic models by comparing various pharmacokinetic parameters [227, 228, 243]. Although the main aim of the study by Keunen et al. [243] was to characterise cancer drug treatment in rats, using the DCATH model, decreased K_{trans} and K_{ep} and no change in ve was found after treatment and similar trends were found with application of the Tofts model. Others have reported that the GCTT model outperforms the Tofts model in the characterisation of glioblastoma [227], and yet others found that while there may be correlation in pharmacokinetic parameters across several two-compartmental models, they are not necessarily quantitatively the same, and there

may be more agreement between parameters in healthy tissue than in cervical cancer tissue [228]. Insofar as the pharmacokinetic models fit the contrast-time-curve, our study shows that applied in the TMJ, it makes little, if any difference, whether one uses the 2XCM, AATH or GCTT models, as computed within the GCTT framework, or whether one applies the DCATH model. Which of the four models is most JIA sensitive in the TMJ, is still an open question. DCE-MRI could be suited for evaluation of JIA affectation of the TMJ, if the temporal resolution is high (≤ 4 s) and with a high-level motion correction. Although structural contrast-enhanced images are most used in the clinic at present [173, 174], given the lack of consensus on how to diagnose JIA affected TMJ, a comparison to some gold standard is difficult. Longitudinal follow-ups to monitor disease progression and changes in pharmacokinetic parameters in time may be of value.

4.2 Paper 2

A key to reaching treatment decisions concerning brain metastases is the longitudinal follow-up of patients to monitor disease development. Perfusion parameters such as $rCBV$ and $rCBF$ are sensitive to the AIF measurement needed for their estimation. To assess the potential of perfusion parameters in the evaluation of developing disease, one needs adequate AIF measurements to arrive at robust $rCBV$ and $rCBF$ estimates. Scan-specific AIFs are the most applied AIFs in DSC-MRI. There are many easily applicable methods for automated AIF selections [182–185]. However, apart from two abstracts presented at the ISMRM, both reporting preference for patient-specific AIFs when performing DSC-MRI [94, 95], little has been done to verify whether scan-specific or patient-specific AIFs are better suited in the longitudinal follow-up of brain metastases. Our results show that scan-specific AIFs are preferable. Shape analysis of the AIF showed that AIFs sampled at different time points in the same patient may be more similar to one another than to AIFs sampled across patients, implying that at least patient-specific AIFs rather than population-based AIFs are necessary. Low correlation between parameter estimations in time could provide a basis not preferring certain AIFs. Therefore, to assess parameters estimations in time, a clustering algorithm was applied to identify AIFs yielding the most correlated perfusion parameter estimations in time. Nevertheless, it is difficult to evaluate repeatability at different time points in metastases, as lesions develop in time. Consequently, the ability to differentiate between white matter and grey matter was tested. Scan-specific AIFs were best suited for this differentiation.

4.3 Paper 3

Low baseline perfusion estimates were associated with unfavourable outcome post SRS. An explanation for this may be that hypoxic tumours exhibit poorer response to radiotherapy and SRS [244, 245]. This result does not mean that patients with low perfusion do not benefit from SRS. Rather, if the metastasis in question appears to increase in size post treatment, it may trigger particular attention as it is more likely progressing than if it were highly perfused prior to SRS. However, this must be regarded as a possible hypothesis, since significant findings did not persist if patients with no follow-up were excluded from the analysis. Furthermore, the results are valid for metastases larger than

0.5 cc, given that this was one of our inclusion criteria to limit partial volume effects. Most research focusing on perfusion measurements in brain metastases patients is concentrated on post-SRS treatment perfusion measurements [246–250]. Insofar as perfusion measurements have been made prior to SRS treatment, our results harmonise well with other studies, one of which found increased $rCBV$ at baseline in treatment responders [251], and others have struggled to find a correlation between pretherapeutic $rCBV$ and $rCBF$ and outcome [197, 199, 252]. 5 out of 7 pseudo-progressors were observed to exhibit a transient $rCBF$ increase prior to transient volume increase. This is an observation that needs further validation in future research, as there are few patients in our study. Although transient volume observations are not an unusual proxy measurement for pseudo-progression, ideally pseudo-progression should be confirmed on histology.

4.4 Paper 4

By applying free water correction in gliomas, we showed that the estimation of FW estimation is a way to quantitatively and non-invasively characterise necrotic tumour regions. It may also be possible to monitor potential changes within tumour regions that are due to the development of the disease, although the hypothesis produced by our results must be further evaluated. In general, post contrast T1-weighted images are a common basis for the segmentation of enhancing lesion areas. There are also deep learning methods that help segment glioma and tumour classification [253–255]. The level of contrast enhancement, however, depends on the contrast dose, timing, and individual vasculature of the patient [256]. FW -correction may therefore introduce less user bias than the standard contrast enhanced MRI used for segmentation. Furthermore, the usefulness of characterising the necrotic area may exceed the task of mere segmentation. Recent studies have found that describing the necrotic region can help predict tumour aggressiveness in glioblastoma patients [257, 258]. Oxygen enhanced MRI, where the patient inhales pure O_2 prior to imaging, and the super oxygenated haemoglobin increases the T1 relaxation rate in perfused tissue where the O_2 is dissolved, is currently explored to characterise necrotic tumour regions, linking it to tumour aggressiveness [259]. Further research, perhaps in conjunction with other methods of characterising necrotic tumour regions should be performed to validate the clinical usefulness of our proof-of-concept study.

Discussion of non-published material related to Paper 4

Fibre tracts in the immediate vicinity of the glioma can be of importance when planning surgery, and several studies have reported improved fibre tracking following FW correction [164, 165, 168–170]. In agreement with these studies, we found an increased number of tracts in the tumour vicinity when applying a fixed threshold of $FA = 0.27$ to the FW corrected data, compared to the number of tracts in the same region by applying a threshold of $FA = 0.2$ to the non-corrected data. A usual tracking threshold is $FA = 0.2$ in non-corrected data, and so the applied threshold in the corrected data corresponds to the shift in mean FA post FW correction. Comparing tractography results between FW -corrected and non-corrected data is challenging due to the inherent FA increase in

FW-corrected data relative to non-corrected data. By setting a fixed *FA* threshold one risks engineering an increased number of modelled fibre tracts compared to the non-FW corrected scenario [165]. To assess possible biases in our results, we performed whole brain tractography with Otsu-optimal and two different fixed thresholds. With a fixed *FA* threshold of 0.27 in the FW-corrected data, and a fixed *FA* threshold of 0.2 in the non-corrected data, we observed no significant difference in mean number and length of modelled tracts in the corrected and non-corrected data. However, tract irregularity was significantly lower when tracking in the FW-corrected data. This could mean that FW-correction may help avoid false positive tracts. The employed FW-correction applies piecewise smoothing between neighbouring voxels in the diffusion tensor, hence some of the reduction of irregularity may also be due to the regularization. On the other hand, when equal and fixed *FA* thresholds are applied to FW-corrected and non-corrected DWI, there is no difference in tract irregularity.

4.5 Remaining challenges and outlook

4.5.1 Number of patients

A limitation in all the papers on which this thesis is based is the number of patients included in each study. In Paper 1, 52 out of 73 patients showed evidence of having JIA affected TMJ, based on scores determined from structural imaging as the ground truth. In Paper 2 only 8 brain metastases patients, that underwent at least five scans were included, although this included data from 83 scans. Papers 3 and 4 included perfusion or diffusion estimates from baseline scans from 32 and 25 patients, respectively. Because diseases investigated in this thesis are heterogeneous in nature, and there may be many factors contributing to a parametric map, larger numbers of patients are necessary to identify precise origins of the observed effects. To increase the number of patients multi-centre, and even international studies are necessary, since disease prevalence is relatively low and, in the case of brain tumours, the mortality rate is high. Paper 1 is a multi-centre study, but we acknowledge that data sharing concerning the JIA scores based on structural images could have been better managed. While studies such as these should be expanded, it is still the case that each patient needs an individual assessment for diagnostics and treatment planning. Even though one cannot hope to identify all causes and effects with relatively few data points, we were still able to evaluate post-processing techniques of DCE- and DSC-MRI data, and to point towards early perfusion measurements as potential biomarkers predictive of outcome in brain metastases and towards a FW elimination method for characterisation of glioma.

4.5.2 Image quality

Motion correction is a standard step in the data processing, and several software tools have been developed to do this; for instance Elastix [212, 213], SPM [219] and FSL [216–218]. In Paper 1 an affine motion correction as implemented in Elastix was combined with an inhouse algorithm through successive application. SPM and FSL are tools developed particularly for brain imaging. Tools like Elastix, SPM and FSL have been carefully validated and have been applied successfully many times. Nevertheless, it may be necessary to carefully consider the extent to which the motion correction tools provide the correct approach to the images being analysed.

Voxel brightness due to contrast enhancement is dependent on contrast dose, timing, and individual vasculature of the patient [256]. This may be of greater interest in delineation of ROIs than in the calculation of perfusion parameters. In the deconvolution for perfusion parameter estimation, contrast time curves are usually adjusted for delay. Also, the perfusion parameters are supposed to pick up differences in vascularity, not necessarily defining an ROI.

Diffusion images are sensitive to noise. For the diffusion acquisitions in Paper 4, diffusion was measured along eight directions in each b-value shell. While six directions are the minimum to fit the diffusion tensor, measurements in more directions might have rendered the data less noisy. However, the total acquisition time for the diffusion protocol was four minutes, which is a reasonable time frame in the clinic.

4.5.3 Ethical concerns with use of contrast agent

It could be a concern that contrast agent may accumulate in the brain, particularly when it is administered repeatedly. Although it is not currently established that Gadolinium-based contrast agent accumulation in the brain is dangerous [260], it may still be undesirable, particularly in children, as their brains are still undergoing rapid development. The risk of possible neurologic effects needs to be weighed against the advantages of possible early diagnosis of JIA affected TMJ. The assessment of post-contrast structural MR images is currently one of the more common methods for evaluation of possible JIA affected TMJ [173, 174]. Adding DCE-MRI analysis does therefore not add extra risk to a method which is already applied in the clinic. The use of Gadolinium-based contrast agent in brain tumour patients is much less controversial. Brain tumour patients are older, the disease is lethally aggressive, and it is probably not possible to distinguish symptoms of contrast agent accumulation from those of treatment side effects.

4.5.4 Complementary information with different MRI indices

PWI and DWI can be regarded as complementary, though not entirely independent, advanced MRI techniques. The dynamics of microcirculation is usually explored with DSC and DCE-MRI, although intravoxel incoherent motion can also be picked up by low b-value diffusion imaging [41]. Diffusion imaging and DTI on the other hand, capture aspects of the tissue microstructure. Different tissue aspects are investigated with perfusion and diffusion estimates, and the estimates are performed independently. However, microstructural integrity can also affect perfusion estimates. The net effect of damaged microstructure depends on the kind of damage. For example, one expects low perfusion estimates in necrotic regions, and high perfusion in regions with angiogenesis, however *MD* could be increased in both cases.

In Paper 4 we observed that “the *FA* distribution changed significantly in both the enhancing and non-enhancing tumour regions, but not in the necrotic region”. Since pseudo-progression is often accompanied by dead tissue, water, and immune cell infiltration, *FA* may behave similarly in regions of pseudo-progression as those of necrosis. In future work it could be tested whether FW-correction can help in early detection of pseudo-progression, and whether FW-based characterisations of lesions prior to or simultaneously to developing pseudo-progression can be correlated to findings of low baseline perfusion estimates, such as in Paper 3. As previously observed, it can be challenging to perform large studies on brain tumour patients. Also, the transition from group statistics to treatment decisions in individual patients may not be straight forward. If several independently estimated markers of disease development could be identified, more accurate singling out individuals with particular outcomes may be possible.

In recent years radiomics has become an emerging field. In radiomics, various pixel intensity-based features are used to characterise image patterns in ROIs, and then these features are fed to machine learning algorithms that correlate features to clinical outcomes [261]. A challenge in radiomics is that the features that are studied are based on image patterns, e.g., shapes and heterogeneity, rather than simple quantitative physiological estimates. Nevertheless, radiomics is being explored using parameter perfusion and diffusion maps as well [262–265], and patterns in the parameter maps are caused by the physiology represented on the maps. Since FW corrected maps may give a better characterisation of the underlying tissue, (ref. our study in Paper 4 with better description of the necrotic area, improved delineation of necrotic and enhancing regions as well as increased entropy in FW-corrected areas) adding FW estimates and FW corrected DTI indices to radiomics could help the understanding of the mechanisms leading to certain clinical outcomes. One could imagine applying radiomics to a range of pharmacokinetic parameter maps too, both in the central nervous system and in other parts of the body, for instance in the TMJ.

4.5.5 Application in the clinic

Although there is great potential in the application of advanced MRI methods in the clinic, there are still a few obstacles. One must take the step from group statistics to clinical decisions pertaining to individual patients. If an ROI is better described using a multi-modal approach combining several modelling approaches, the patients will spend more time in the scanner. This could compromise current patient comfort as current research may benefit future patients more than the present patients. Further, advanced MRI requires excellent cooperation between technical and clinical staff. An automated pipeline is necessary to ensure fast and homogeneous data processing without increasing the work load of hospital staff.

4.6 Conclusion

This thesis is part of the move toward increasingly quantitative MRI diagnostics and prognostics, based not only on structural imaging but also on physiological information inferred from advanced modelling. Necessary requirements for optimal data pre-processing were explored, as well as the feasibility of perfusion and diffusion MRI in selected clinical applications. It was shown that the advanced MRI methods applied can add to a more accurate description of the TMJ and of brain lesions. To routinely apply these methods in the clinic, however, pre-processing steps should become more automated, combinations of advanced MRI methods should be considered, and one must make the move from reporting group statistics to individual treatment decisions.

References

- [1] F. Bloch, "Nuclear induction," *Phys Rev*, vol. 70, no. 7-8, pp. 460–474, 1946.
- [2] The NIST Reference on Constants, Units, and Uncertainty. "CODATA Internationally Recommended 2018 values of the Fundamental Physical Constants." (2019), [Online]. Available: <https://physics.nist.gov/cgi-bin/cuu/Value?gammaubar> (visited on 09/24/2021).
- [3] R. W. Brown, Y.-C. N. Cheng, E. M. Haacke, M. R. Thompson, and R. Venkatesan, *Magnetic resonance imaging: Physical principles and sequence design, Second edition*, 2nd ed. Wiley, 2014, ISBN: 9781118633984.
- [4] R. B. Buxton, *Introduction to Functional Magnetic Resonance Imaging: Principles & Techniques*. Cambridge: Cambridge University Press, 2002.
- [5] P. A. Bottomley, T. H. Foster, R. E. Argersinger, and L. M. Pfeifer, "A review of normal tissue hydrogen NMR relaxation times and relaxation mechanisms from 1-100 MHz: Dependence on tissue type NMR frequency, temperature, species, excision and age," *Med Phys*, vol. 11, no. 4, pp. 425–448, 1984.
- [6] J. Pauly, P. L. Roux, D. Nishimura, and A. Macovski, "Parameter relations for the Shinnar-Le Roux selective excitation pulse design algorithm," *IEEE Trans Med Imaging*, vol. 10, no. 1, pp. 53–65, 1991.
- [7] M. Markl and J. Leupold, "Gradient echo imaging," *J Magn Reson Imaging*, vol. 35, no. 6, pp. 1274–1289, 2012.
- [8] R. B. Buxton, R. R. Edelman, B. R. Rosen, G. L. Wismer, and T. J. Brady, "Contrast in rapid MR imaging: T1- and T2-weighted imaging," *J Comp Assist Tomogr*, vol. 11, no. 1, pp. 7–16, 1987.
- [9] W. A. Edelstein, J. M. S. Hutchinson, G. Johnson, and T. W. Redpath, "Spin warp NMR imaging and application to human whole-body imaging," *Phys Med Biol*, vol. 25, no. 4, pp. 751–756, 1980.
- [10] E. O. Brigham and R. E. Morrow, "The fast Fourier transform," *IEEE Spectrum*, vol. 4, no. 12, pp. 63–70, 1967.
- [11] D. B. Twieg, "The k-trajectory formulation of the NMR imaging process with applications in analysis and synthesis of imaging methods," *Med Phys*, vol. 10, no. 5, pp. 610–621, 1983.
- [12] D. B. Plewes and W. Kucharczyk, "Physics of MRI: A primer," *J Magn Reson Imaging*, vol. 35, no. 5, pp. 1038–1054, 2012.
- [13] S. Langlois, M. Desvignes, J.-M. Constans, and M. Revenu, "MRI geometric distortion: A simple approach to correcting the effects of non-linear gradient fields," *J Magn Reson Imaging*, vol. 9, no. 6, pp. 821–831, 1999.
- [14] S. S. Hidalgo-Tobon, "Theory of gradient coil design methods for magnetic resonance imaging," *Concepts Mag Res*, vol. 36A, no. 4, pp. 223–242, 2010.

- [15] M. N. Hood, V. B. Ho, J. G. Smirniotopoulos, and J. Szumowski, "Chemical shift: The artifact and clinical tool revisited," *Radiographics*, vol. 19, no. 2, pp. 357–371, 1999.
- [16] J. F. Schenk, "The role of magnetic susceptibility in magnetic resonance imaging: MRI magnetic compatibility of the first and second kinds," *Med Phys*, vol. 23, no. 6, pp. 812–850, 1996.
- [17] T. C. Larson III, W. M. Kelly, R. L. Ehman, and F. W. Wehrli, "Spatial misregistration of vascular flow during MR imaging of the CNS: Cause and clinical significance," *AJR Am J Roentgenol*, vol. 155, no. 5, pp. 1117–1124, 1990.
- [18] S. C. Thust, J. van den Bent, and M. Smits, "Pseudoprogession of brain tumors," *J Magn Reson Imaging*, vol. 48, no. 3, pp. 571–589, 2018.
- [19] R. J. Young *et al.*, "Potential utility of conventional MRI signs in diagnosing pseudoprogession in glioblastoma," *Neurology*, vol. 76, no. 22, pp. 1918–1924, 2011.
- [20] A. L. Stockham *et al.*, "Conventional MRI does not reliably distinguish radiation necrosis from tumor recurrence after stereotactic surgery," *J Neurooncol*, vol. 109, no. 1, pp. 149–158, 2012.
- [21] P. F. Weiss *et al.*, "High prevalence of temporomandibular joint arthritis at disease onset in children with juvenile idiopathic arthritis, as detected by magnetic resonance imaging but not by ultrasound," *Arthritis Rheumatol*, vol. 58, no. 4, pp. 1189–1196, 2008.
- [22] P. J. Manners and C. Bower, "Worldwide prevalence of juvenile arthritis - why does it vary so much?" *J Rheumatol*, vol. 29, no. 7, pp. 1520–1530, 2002.
- [23] P. Niibo, C. Pruunsild, Ü. Voog-Oras, T. Nikopensusius, T. Jagomägi, and M. Saag, "Contemporary management of TMJ involvement in JIA patients and its orofacial consequences," *EPMA J*, vol. 7, no. 12, pp. 1–9, 2016.
- [24] P. S. Tofts *et al.*, "Estimating kinetic parameters from dynamic contrast-enhanced T(1)-weighted MRI of a diffusable tracer: Standardized quantities and symbols," *J Magn Reson Imaging*, vol. 10, no. 3, pp. 223–232, 1999.
- [25] B. R. Rosen, J. W. Belliveau, J. M. Vevea, and T. J. Brady, "Perfusion imaging with NMR contrast agents," *Magn Reson Med*, vol. 14, no. 2, pp. 701–735, 1990.
- [26] L. Østergaard, "Principles of cerebral perfusion imaging by bolus tracking," *J Magn Reson Imaging*, vol. 22, no. 6, pp. 710–717, 2005.
- [27] A. Einstein, "Über die von der molekularkinetischen Theorie der Wärme geforderte Bewegung von in ruhenden Flüssigkeiten suspendierten Teilchen," *Ann Phys*, vol. 322, no. 8, pp. 549–560, 1905.
- [28] E. O. Stejskal and J. E. Tanner, "Spin diffusion measurements: Spin echoes in the presence of a time-dependent field gradient," *J Chem Phys*, vol. 42, no. 1, pp. 288–292, 1965.
- [29] Z. Zhou and Z.-R. Lu, "Gadolinium-based contrast agents for magnetic resonance cancer imaging," *WIREs Nanomed Nanobiotechnol*, vol. 5, no. 1, pp. 1–18, 2013.

- [30] Department of Radiology, University of Wisconsin School of Medicine and Public Health. "Gadolinium based contrast dosing charts." (2017), [Online]. Available: <https://www.radiology.wisc.edu/wp-content/uploads/2017/10/gadolinium-based-contrast-dosing-charts.pdf> (visited on 09/29/2021).
- [31] J. Endrikat, R. Barbati, M. Scarpa, G. Jost, and A. E. Uber, "Accuracy and repeatability of automated injector versus manual administration of an MRI contrast agent - results of a laboratory study," *Invest Radiol*, vol. 53, no. 1, pp. 1–5, 2018.
- [32] K. T. Bae, "Intravenous contrast medium administration and scan timing at CT: Considerations and approaches," *Radiology*, vol. 256, no. 1, pp. 32–61, 2010.
- [33] K. T. Bae, J. P. Heiken, and J. A. Brink, "Aortic and hepatic contrast medium enhancement at CT. Part I. Prediction with a computer model," *Radiology*, vol. 207, no. 3, pp. 647–655, 1998.
- [34] R. J. McDonald *et al.*, "Gadolinium retention: A research roadmap from the 2018 NIH/ACR/RSNA workshop on gadolinium chelates," *Radiology*, vol. 289, no. 2, pp. 517–534, 2018.
- [35] R. J. McDonald *et al.*, "Intracranial gadolinium deposition after contrast-enhanced MR imaging," *Radiology*, vol. 275, no. 3, pp. 772–782, 2015.
- [36] E. Vergauwen *et al.*, "Central nervous system gadolinium accumulation in patients undergoing periodical contrast MRI screening for hereditary tumor syndromes," *Hered Cancer Clin Pract.*, vol. 16, no. 2, 2018. doi: 10.1186/s13053-017-0084-7.
- [37] Britannica, The Editors of Encyclopaedia. "Capillary." (2021), [Online]. Available: <https://www.britannica.com/science/capillary> (visited on 09/29/2021).
- [38] T. S. Koh, S. Bisdas, D. M. Koh, and C. H. Thng, "Fundamentals of tracer kinetics for dynamiccontrast-enhanced MRI," *J Magn Reson Imaging*, vol. 34, no. 6, pp. 1362–1276, 2011.
- [39] O. M. Abdullah, A. D. Gomez, S. Merchant, M. Heidinger, S. Poelzing, and E. W. Hsu, "Orientation dependence of microcirculation-induced diffusion signal in anisotropic tissues," *Magn Reson Med*, vol. 76, no. 4, pp. 1252–1262, 2016.
- [40] R. Eriksson, H. W. Persson, S. O. Dymling, and K. Lindström, "A microcirculation phantom for performance testing of blood perfusion measurement equipment," *Eur J Ultrasound*, vol. 2, no. 1, pp. 65–75, 1995.
- [41] D. Le Bihan, "What can we see with IVIM MRI?" *Neuroimage*, vol. 187, pp. 56–67, 2019.
- [42] J. S. Pober and W. C. Sessa, "Inflammation and the blood microvascular system," *Cold Spring Harb Perspect Biol*, vol. 7, no. 1, a016345, 2015.
- [43] G. W. Payne, J. A. Madri, W. C. Sessa, and S. S. Segal, "Abolition of arteriolar dilation but not constriction to histamine in cremaster muscle of eNOS^{-/-} mice," *Am J Physiol Heart Circ Physiol*, vol. 285, no. 2, H493–H498, 2003.
- [44] S. P. Li and A. R. Padhani, "Tumor response assessments with diffusion and perfusion MRI," *J Magn Reson Imaging*, vol. 35, no. 4, pp. 745–763, 2012.

- [45] M. Muto *et al.*, “Dynamic susceptibility contrast (DSC) perfusion MRI in differential diagnosis between radionecrosis and neoangiogenesis in cerebral metastases using rCBV, rCBF and K₂,” *Radiol Med*, vol. 123, no. 7, pp. 545–552, 2018.
- [46] D.-M. Koh and D. J. Collins, “Diffusion-weighted MRI in the body: Applications and challenges in oncology,” *AJR Am J Roentgenol*, vol. 188, no. 6, pp. 1622–1635, 2007.
- [47] Oxford Lexico, Lexico.com. “Uk english, perfusion.” (2021), [Online]. Available: <https://www.lexico.com/definition/perfusion> (visited on 08/05/2021).
- [48] A. A. Qayyum and J. Kastrup, “Measuring myocardial perfusion: The role of PET, MRI and CT,” *Clin Radiol*, vol. 70, no. 6, pp. 576–584, 2015.
- [49] C. K. Kuhl *et al.*, “Dynamic breast MR imaging: Are signal intensity time course data useful for differential diagnosis of enhancing lesions?” *Radiology*, vol. 211, no. 1, pp. 101–110, 1999.
- [50] J.-M.-Idée, M. Port, I. Raynal, M. Schaefer, S. Le Greneur, and C. Corot, “Clinical and biological consequences of transmetallation induced by contrast agents for magnetic resonance imaging: A review,” *Fundam Clin Pharmacol*, vol. 20, no. 6, pp. 563–576, 2013.
- [51] S. M. Lattanzio, “Toxicity associated with gadolinium-based contrast-enhanced examinations,” *AIMS Biophys*, vol. 8, no. 2, pp. 198–220, 2021.
- [52] R. M. Weisskoff, C. S. Zuo, J. L. Boxerman, and B. R. Rosen, “Microscopic susceptibility variation and transverse relaxation: Theory and experiment,” *Magn Reson Med*, vol. 31, no. 6, pp. 601–610, 1994.
- [53] L. M. De León-Rodríguez, A. Martins, M. C. Pinho, N. M. Rofsky, and A. D. Sherry, “Basic MR relaxation mechanisms and contrast agent design,” *J Magn Reson Imaging*, vol. 42, no. 3, pp. 545–565, 2015.
- [54] Y. Shen *et al.*, “T₁ relaxivities of gadolinium-based magnetic resonance contrast agents in human whole blood at 1.5, 3, and 7 T,” *Invest Radiol*, vol. 50, no. 5, pp. 330–338, 2015.
- [55] S. Sourbron *et al.*, “Bolus-tracking MRI with a simultaneous T₁- and T₂* measurement,” *Magn Reson Med*, vol. 62, no. 3, pp. 672–681, 2009.
- [56] G.-H. Jahng, K.-L. Li, L. Ostergaard, and F. Calamante, “Perfusion magnetic resonance imaging: A comprehensive update on principles and techniques,” *Korean J Radiol*, vol. 15, no. 5, pp. 554–577, 2014.
- [57] S. Sourbron and D. L. Buckley, “Tracer kinetic modelling in MRI: Estimating perfusion and capillary permeability,” *Phys Med Biol*, vol. 57, no. 2, R1–R33, 2011.
- [58] P. Meier and K. L. Zierler, “On the theory of the indicator-dilution method for measurement of blood flow and volume,” *J Appl Physiol*, vol. 6, no. 12, pp. 731–744, 1954.
- [59] P. S. Tofts and A. G. Kermode, “Measurement of the blood-brain barrier permeability and leakage space using dynamic MR imaging. 1. Fundamental concepts,” *Magn Reson Med*, vol. 17, no. 2, pp. 357–367, 1991.

- [60] S. P. Sourbron and D. L. Buckley, "On the scope and interpretation of the Tofts models for DCE-MRI," *Magn Reson Med*, vol. 66, no. 3, pp. 735–745, 2011.
- [61] C. A. Cuenod and D. Balvay, "Perfusion and vascular permeability: Basic concepts and measurement in DCE-CT and DCE-MRI," *Diagn Interv Imaging*, vol. 94, no. 12, pp. 1187–1204, 2013.
- [62] G. Brix *et al.*, "Microcirculation and microvasculature in breast tumors: Pharmacokinetic analysis of dynamic MR image series," *Magn Reson Med*, vol. 52, no. 2, pp. 420–429, 2004.
- [63] G. Brix, M. Bahner, U. Hoffmann, A. Horvath, and W. Schreiber, "Regional blood flow, capillary permeability, and compartment volumes: Measurement with dynamic computed tomography — initial experience," *Radiology*, vol. 210, no. 1, pp. 269–276, 1999.
- [64] J. A. Johnson and T. A. Wilson, "A model for capillary exchange," *Am J Physiol*, vol. 210, no. 6, pp. 1299–1303, 1966.
- [65] K. S. St. Lawrence and T.-Y. Lee, "An adiabatic approximation to the tissue homogeneity model for water exchange in the brain: I. Theoretical derivation," *J Cereb Blood flow Metab*, vol. 18, no. 12, pp. 1365–1377, 1998.
- [66] M. Bartoš, M. Šorel, and R. Jiřík, "Time-efficient fourier domain evaluation of pharmacokinetic model in dynamic contrast-enhanced magnetic resonance imaging," in *World Congress on Medical Physics and Biomedical Engineering IFMBE Proceedings*, L. Lhotska, L. Sukupova, I. Lacković, and G. Ibbott, Eds., 2018.
- [67] K. S. St. Lawrence and T.-Y. Lee, "An adiabatic approximation to the tissue homogeneity model for water exchange in the brain: II. Experimental validation," *J Cereb Blood flow Metab*, vol. 18, no. 12, pp. 1378–1385, 1998.
- [68] T. S. Koh *et al.*, "The inclusion of capillary distribution in the adiabatic tissue homogeneity model of blood flow," *Phys Med Biol*, vol. 46, no. 5, pp. 1519–1538, 2001.
- [69] M. C. Schabel, "A unified impulse response model for DCE-MRI," *Magn Reson Med*, vol. 68, no. 5, pp. 1632–1646, 2012.
- [70] K. Welker, J. Boxerman, A. Kalnin, T. Kaufmann, M. Shiroshi, and M. Wintermark, "ASFN recommendations for clinical performance of MR dynamic susceptibility contrast perfusion imaging of the brain," *AJNR Am J Neuroradiol*, vol. 36, no. 6, pp. E41–E51, 2015.
- [71] J. E. Perthen, F. Calamante, D. G. Gadian, and A. Connelly, "Is quantification of bolus tracking MRI reliable without deconvolution?" *Magn Reson Med*, vol. 47, no. 1, pp. 61–67, 2002.
- [72] J. C. Kosior and R. Frayne, "Perfusion parameters derived from bolus-tracking perfusion imaging are immune to tracer recirculation," *J Magn Reson Imaging*, vol. 31, no. 3, pp. 753–756, 2010.

- [73] L. Østergaard, R. M. Weisskoff, D. A. Chesler, C. Gyldensted, and B. R. Rosen, "High resolution measurement of cerebral blood flow using intravascular tracer bolus passages. Part I: Mathematical approach and statistical analysis," *Magn Reson Med*, vol. 36, no. 5, pp. 715–725, 1996.
- [74] M. A. Schmidt *et al.*, "Standardized acquisition and post-processing of dynamic susceptibility contrast perfusion in patients with brain tumors, cerebrovascular disease and dementia: Comparability of post-processing software," *Br J Radiol*, vol. 93, no. 1105, p. 20190543, 2020.
- [75] F. Calamante, D. G. Gadian, and A. Connelly, "Quantification of bolus-tracking MRI: Improved characterization of the tissue residue function using Tikhonov regularization," *Magn Reson Med*, vol. 50, no. 6, pp. 1237–1247, 2003.
- [76] O. Wu, L. Østergaard, R. M. Weisskoff, T. Benner, B. R. Rosen, and A. G. Sorensen, "Tracer arrival timing-insensitive technique for estimating flow in MR perfusion-weighted imaging using singular value decomposition with a block-circulant deconvolution matrix," *Magn Reson Med*, vol. 50, no. 1, pp. 164–174, 2003.
- [77] M. Meijs, S. Christensen, M. G. Lansberg, G. W. Albers, and F. Calamante, "Analysis of perfusion MRI in stroke: To deconvolve, or not to deconvolve," *Magn Reson Med*, vol. 76, no. 4, pp. 1282–1290, 2015.
- [78] F. Calamante, "Arterial input function in perfusion mri: A comprehensive review," *Prog Nucl Magn Reson Spectrosc*, vol. 74, pp. 1–32, 2013.
- [79] T. E. Conturo *et al.*, "Arterial input functions for dynamic susceptibility contrast MRI: requirements and signal options," *J Magn Reson Imaging*, vol. 22, no. 6, pp. 697–703, 2005.
- [80] L. Willats, S. Christensen, H. K. Ma, G. A. Donnan, A. Connelly, and F. Calamante, "Validating a local arterial input function method for improved perfusion quantification in stroke," *J Cereb Blood Flow Metab*, vol. 31, no. 11, pp. 2189–2198, 2011.
- [81] F. Calamante, "Bolus dispersion issues related to the quantification of perfusion MRI data," *J Magn Reson Imaging*, vol. 22, no. 6, pp. 718–722, 2005.
- [82] F. Calamante, D. G. Gadian, and A. Connelly, "Delay and dispersion effects in dynamic susceptibility contrast MRI: Simulations using singular value decomposition," *Magn Reson Med*, vol. 44, no. 3, pp. 466–473, 2000.
- [83] L. Willats, A. Connelly, and F. Calamante, "Minimizing the effects of bolus dispersion in bolus-tracking MRI," *NMR Biomed*, vol. 21, no. 10, pp. 1126–1137, 2008.
- [84] M. Boos, K. Scheffler, R. Haselhorst, E. Reese, J. Frölich, and G. M. Bongartz, "Arterial first pass gadolinium-CM dynamics as a function of several intravenous saline flush and Gd volumes," *J Magn Reson Imaging*, vol. 13, no. 4, pp. 568–576, 2001.
- [85] T. F. Hany, G. C. McKinnon, D. A. Leung, T. Pfammatter, and J. F. Debatin, "Optimization of contrast timing for breath-hold three-dimensional MR angiography," *J Magn Reson Imaging*, vol. 7, no. 3, pp. 551–556, 1997.

- [86] J. J. Chen, M. R. Smith, and R. Frayne, "The impact of partial-volume effects in dynamic susceptibility contrast magnetic resonance perfusion imaging," *J Magn Reson Imaging*, vol. 22, no. 3, pp. 390–399, 2005.
- [87] M. J. P. van Osch, J. van der Grond, J. G. Chris, and C. J. G. Bakker, "Partial volume effects on arterial input functions: Shape and amplitude distortions and their correction," *J Magn Reson Imaging*, vol. 22, no. 6, pp. 704–709, 2005.
- [88] R. Meng, B. Meadler, S. D. Chang, E. C. Jones, S. L. Goldenberg, and P. Kozlowski, "3T DCE MRI in prostate cancer – comparison between population average and patient specific arterial input function," in *ISMRM*, 2009.
- [89] M. Azahaf *et al.*, "Impact of arterial input function selection on the accuracy of dynamic contrast-enhanced MRI quantitative analysis for the diagnosis of clinically significant prostate cancer," *J Magn Reson Imaging*, vol. 43, no. 3, pp. 737–749, 2015.
- [90] A. Fedorov *et al.*, "A comparison of two methods for estimating DCE-MRI parameters via individual and cohort based AIFs in prostate cancer: A step towards practical implementation," *Magn Reson Imaging*, vol. 32, no. 4, pp. 321–329, 2014.
- [91] R. Meng, S. D. Chang, E. C. Jones, S. L. Goldenberg, and P. Kozlowski, "Comparison between population average and experimentally measured arterial input function in predicting biopsy results in prostate cancer," *Acad Radiol*, vol. 17, no. 4, pp. 520–525, 2010.
- [92] T. Koopman *et al.*, "Repeatability of arterial input functions and kinetic parameters in muscle obtained by dynamic contrast enhanced MR imaging of the head and neck," *Magn Reson Med*, vol. 68, pp. 1–8, 2020.
- [93] R. E. Port, M. V. Knopp, and G. Brix, "Dynamic contrast-enhanced MRI using Gd-DTPA: interindividual variability of the arterial input function and consequences for the assessment of kinetics in tumors," *Magn Reson Med*, vol. 45, no. 6, pp. 1030–1038, 2001.
- [94] A. Bjørnerud, K. Mouridsen, and K. E. Emblem, "A patient-specific global residue function improves reproducibility in longitudinal monitoring of perfusion changes in lowgrade gliomas," in *ISMRM*, 2011.
- [95] K. Mouridsen, K. E. Emblem, A. Bjørnerud, D. Jennings, and G. Sorensen, "Subject-specific AIF optimizes reproducibility of perfusion parameters in longitudinal DSC-MRI in comparison to session and population level AIF," in *ISMRM*, 2011.
- [96] S. B. Withey, J. Novak, L. MacPherson, and A. C. Peet, "Arterial input function and gray matter cerebral blood volume measurements in children," *J Magn Reson Imaging*, vol. 43, no. 4, pp. 981–989, 2016.
- [97] G. J. M. Parker *et al.*, "Experimentally-derived functional form for a population-averaged high-temporal-resolution arterial input function for dynamic contrast-enhanced MRI," *Magn Reson Med*, vol. 56, no. 5, pp. 993–1000, 2006.

- [98] D. He, L. Xu, W. Qian, J. Clarke, and X. Fan, "A simulation study comparing nine mathematical models of arterial input function for dynamic contrast enhanced MRI to the parker model," *Australas Phys Eng Sci Med*, vol. 41, no. 2, pp. 507–518, 2018.
- [99] M. J. P. van Osch, E. P. A. Vonken, O. Wu, M. A. Viergever, and J. van der Grond, "Model of the human vasculature for studying the influence of contrast injection speed on cerebral perfusion MRI," *Magn Reson Med*, vol. 50, no. 3, pp. 614–622, 2003.
- [100] C. Yang, G. S. Karczmar, M. Medved, A. Oto, and M. Z. nd W. M. Stadler, "Reproducibility assessment of a multiple reference tissue method for quantitative dynamic contrast enhanced-MRI analysis," *Magn Reson Med*, vol. 61, no. 4, pp. 851–859, 2009.
- [101] I. Digernes, A. Bjørnerud, and S. A. S. Vatnehol, "A theoretical framework for determining cerebral vascular function and heterogeneity from dynamic susceptibility contrast MRI," *J Cereb Blood Flow Metab*, vol. 37, no. 6, pp. 2237–2248, 2017.
- [102] L. Bell *et al.*, "Optimization of DSC MRI echo times for CBV measurements using error analysis in a pilot study of high-grade gliomas," *AJNR Am J Neuroradiol*, vol. 38, no. 9, pp. 1710–1715, 2017.
- [103] L. Knutsson *et al.*, "Absolute quantification of cerebral blood flow: Correlation between dynamic susceptibility contrast MRI and model-free arterial spin labeling," *Magn Reson Imaging*, vol. 28, no. 1, pp. 1–7, 2010.
- [104] C. Tönnies *et al.*, "Deterministic arterial input function selection in DCE-MRI for automation of quantitative perfusion calculation of colorectal cancer," *Magn Reson Imaging*, vol. 75, pp. 116–123, 2021.
- [105] K. M. Schmainda *et al.*, "Multi-site concordance of DSC-MRI analysis for brain tumors: Results of a national cancer institute quantitative imaging network collaborative project," *AJNR Am J Neuroradiol*, vol. 39, no. 6, pp. 1008–1016, 2018.
- [106] R. Tabbara, A. Connelly, and F. Calamante, "Multi-stage automated local arterial input function selection in perfusion MRI," *MAGMA*, vol. 33, no. 3, pp. 357–365, 2020.
- [107] H. Rahimzadeh, A. F. Kazerooni, M. R. Deevband, and H. S. Rad, "An efficient framework for accurate arterial input selection in DSC-MRI of glioma brain tumors," *J Biomed Phys*, vol. 9, no. 1, pp. 69–80, 2019.
- [108] K. Mouridsen, S. Christensen, L. Gyldensted, and L. Østergaard, "Automatic selection of arterial input function using cluster analysis," *Magn Reson Med*, vol. 55, no. 3, pp. 524–531, 2006.
- [109] S. Christensen *et al.*, "Inferring origin of vascular supply from tracer arrival timing patterns using bolus tracking MRI," *J Magn Reson Imaging*, vol. 27, no. 6, pp. 1371–1381, 2008.

- [110] V. C. Keil *et al.*, “Effects of arterial input function selection on kinetic parameters in brain dynamic contrast-enhanced MRI,” *Magn Reson Imaging*, vol. 40, pp. 83–90, 2017.
- [111] E. J. W. Bleeker, M. A. van Buchem, and M. J. P. van Osch, “Optimal location for arterial input function measurements near the middle cerebral artery in first-pass perfusion MRI,” *J Cereb Blood Flow Metab*, vol. 29, no. 4, pp. 840–852, 2009.
- [112] M. Kleppestø, A. Bjørnerud, I. R. Groote, M. Kim, J. Vardal, and C. Larsson, “Operator dependency of arterial input function in dynamic contrast-enhanced MRI,” *MAGMA*, vol. doi: 10.1007/s10334-021-00926-z. Epub ahead of print. PMID: 34213687. ADD, 2021.
- [113] M. Cutajar, I. A. Mendichovszky, P. S. Tofts, and I. Gordon, “The importance of AIF ROI selection in DCE-MRI renography: Reproducibility and variability of renal perfusion and filtration,” *Eur J Radiol*, vol. 74, no. 3, e154–e160, 2010.
- [114] C. Yang, G. S. Karczmar, M. Medved, and W. M. Stadler, “Estimating the arterial input function using two reference tissues in dynamic contrast-enhanced MRI studies: Fundamental concepts and simulations,” *Magn Reson Med*, vol. 52, no. 5, pp. 1110–1117, 2004.
- [115] T. E. Yankeelov *et al.*, “Quantitative pharmacokinetic analysis of DCE-MRI data without an arterial input function: A reference region model,” *Magn Reson Imaging*, vol. 23, no. 4, pp. 519–529, 2005.
- [116] E. Goebell *et al.*, “Disarrangement of fiber tracts and decline of neuronal density correlate in glioma patients - a combined diffusion tensor imaging and ¹H-MR spectroscopy study,” *AJNR Am J Neuroradiol*, vol. 27, no. 7, pp. 1426–1431, 2006.
- [117] S. J. Price and J. H. Gillard, “Imaging biomarkers of brain tumour margin and tumour invasion,” *Br J Radiol*, vol. 84, no. Spec Iss 2, pp. S159–S167, 2011.
- [118] R. Feynman, R. Leighton, and M. Sands, *The Feynman Lectures of Physics, The New Millennium Edition, Volume I*. New York: Basic Books, 2020, pp. 41.1–41.10.
- [119] A. Fick, “On liquid diffusion,” *J Membr Sci*, vol. 100, no. 1, pp. 33–38, 1995.
- [120] D. A. Yablonskiy and A. L. Sukstanskii, “Theoretical models of the diffusion weighted MR signal,” *NMR Biomed*, vol. 23, no. 7, pp. 661–681, 2010.
- [121] M. E. Moseley *et al.*, “Diffusion-weighted MR imaging of anisotropic water diffusion in cat central nervous system,” *Radiology*, vol. 176, no. 2, pp. 439–445, 1990.
- [122] P. J. Basser, J. Mattiello, and D. LeBihan, “MR diffusion tensor spectroscopy and imaging,” *Biophys J*, vol. 66, no. 1, pp. 259–267, 1994.
- [123] P. J. Basser and C. Pierapoli, “Microstructural and physiological features of tissues elucidated by quantitative-diffusion-tensor MRI,” *J Magn Reson B*, vol. 111, no. 3, pp. 209–219, 1996.
- [124] P. J. Basser and C. Pierapoli, “A simplified method to measure the diffusion tensor from seven MR images,” *Magn Reson Med*, vol. 39, no. 6, pp. 928–934, 1998.

- [125] R. L. Brunsing *et al.*, “Restriction spectrum imaging: An evolving imaging biomarker in prostate MRI,” *J Magn Reson Imaging*, vol. 45, no. 2, pp. 323–336, 2016.
- [126] J. H. Jensen and J. A. Helpert, “MRI quantification of non-gaussian water diffusion by kurtosis analysis,” *NMR Biomed*, vol. 23, no. 7, pp. 698–710, 2010.
- [127] M. S. Graham, I. Drobnyak, M. Jenkinson, and H. Zhang, “Quantitative assessment of the susceptibility artefact and its interaction with motion in diffusion MRI,” *PLoS One*, vol. 12, no. 10, e0185647, 2017.
- [128] H. Hamaguchi *et al.*, “Effect of respiratory and cardiac gating on the major diffusion-imaging metrics,” *Neuroradiol J*, vol. 29, no. 4, pp. 254–259, 2016.
- [129] D. C. Hoinkiss and D. A. Porter, “Prospective motion correction in diffusion-weighted imaging using intermediate pseudo-trace-weighted images,” *Neuroimage*, vol. 149, pp. 1–14, 2017.
- [130] D. Le Bihan, C. Poupon, A. Amadon, and F. Lethimonnier, “Artifacts and pitfalls in diffusion MRI,” *J Magn Reson Imaging*, vol. 24, no. 3, pp. 478–488, 2006.
- [131] W. Wu and K. L. Miller, “Image formation in diffusion MRI: A review of recent technical developments,” *J Magn Reson Imaging*, vol. 46, no. 3, pp. 646–662, 2017.
- [132] A. Celik, “Effect of imaging parameters on the accuracy of apparent diffusion coefficient and optimization strategies,” *Diagn Interv Radiol*, vol. 22, no. 1, pp. 101–107, 2016.
- [133] O. Dietrich, A. Biffar, A. Baur-Melnyk, and M. F. Reiser, “Technical aspects of MR diffusion imaging of the body,” *Eur J Radiol*, vol. 76, no. 3, pp. 314–322, 2010.
- [134] P. Mansfield, “Multi-planar image formation using NMR spin echoes,” *J Phys C: Solid State Phys*, vol. 10, no. 3, pp. L55–L58, 1977.
- [135] R. J. Ordidge, P. Mansfield, and R. E. Coupland, “Rapid biomedical imaging by NMR,” *Br J Radiol*, vol. 54, no. 646, pp. 850–855, 1981.
- [136] H. Y. Mesri, S. David, M. A. Viergever, and A. Leemans, “The adverse effect of gradient nonlinearities on diffusion MRI: From voxels to group studies,” *NeuroImage*, vol. 205, p. 116127, 2020.
- [137] P. Mukherjee, J. I. Berman, S. W. Chung, C. P. Hess, and R. G. Henry, “Diffusion tensor MR imaging and fiber tractography: Theoretic underpinnings,” *AJNR Am J Neuroradiol*, vol. 29, no. 4, pp. 632–641, 2008.
- [138] S. B. Vos, D. K. Jones, M. A. Viergever, and A. Leemans, “Partial volume effect as a hidden covariate in DTI analyses,” *NeuroImage*, vol. 55, no. 4, pp. 1566–1576, 2011.
- [139] H. Oouchi *et al.*, “Diffusion anisotropy measurement of brain white matter is affected by voxel size: Underestimation occurs in areas with crossing fibers,” *AJNR Am J Neuroradiol*, vol. 28, no. 6, pp. 1102–1106, 2007.

- [140] P. Preziosa *et al.*, “Axonal degeneration as substrate of fractional anisotropy abnormalities in multiple sclerosis cortex,” *Brain*, vol. 142, no. 7, pp. 1921–1937, 2019.
- [141] A. Kulesh, V. Drobakha, E. Kuklina, I. Nekrasova, and V. Shestakov, “Cytokine response, tract specific fractional anisotropy, and brain morphometry in post-stroke cognitive impairment,” *J Stroke Cerebrovasc Dis*, vol. 27, no. 7, pp. 1752–1759, 2018.
- [142] B. Cheng *et al.*, “Cortical atrophy and transcallosal diaschisis following isolated subcortical stroke,” *J Cereb Blood Flow Metab*, vol. 40, no. 3, pp. 611–621, 2019.
- [143] J. Y. Kim, M. J. Yoon, J. E. Park, E. J. Choi, J. Lee, and H. S. Kim, “Radiomics in peritumoral non-enhancing regions: Fractional anisotropy and cerebral blood volume improve prediction of local progression and overall survival in patients with glioblastoma,” *Neuroradiol*, vol. 61, no. 11, pp. 1261–1272, 2019.
- [144] S. Mori and P. C. van Zijl, “Fiber tracking: Principles and strategies - a technical review,” *NMR Biomed*, vol. 15, no. 7-8, pp. 468–480, 2002.
- [145] F.-C. Yeh, T. D. Vertynen, Y. Wang, J. C. Fernández-Miranda, and W.-Y. I. Tseng, “Deterministic fiber tracking improved by quantitative anisotropy,” *PLoS ONE*, vol. 9, no. 1, e80713, 2010.
- [146] J. D. Tournier, S. Mori, and A. Leemans, “Diffusion tensor imaging and beyond,” *Magn Reson Med*, vol. 65, no. 6, pp. 1532–1556, 2011.
- [147] A. L. Alexander, K. M. Hasan, M. Lazar, J. S. Tsuruda, and D. L. Parker, “Analysis of partial volume effects in diffusion-tensor MRI,” *Magn Reson Med*, vol. 45, no. 5, pp. 770–780, 2001.
- [148] M. L. Ho, R. Rojas, and R. L. Eisenberg, “Cerebral edema,” *AJR Am J Roentgenol*, vol. 199, no. 3, pp. W258–W273, 2012.
- [149] N. Tasali *et al.*, “Temporomandibular joint (TMJ) pain revisited with dynamic contrast-enhanced magnetic resonance imaging (DCE-MRI),” *Eur J Radiol*, vol. 81, no. 3, pp. 603–608, 2011.
- [150] N. G. Papadakis *et al.*, “Study of the effect of CSF suppression on white matter diffusion anisotropy mapping of healthy human brain,” *Magn Reson Med*, vol. 48, no. 2, pp. 394–398, 2002.
- [151] L. Concha, D. W. Gross, and C. Beaulieu, “Diffusion tensor tractography of the limbic system,” *AJNR Am J Neuroradiol*, vol. 26, no. 9, pp. 2267–2274, 2005.
- [152] I. Blystad, J. B. M. Warntjes, Ö. Smedby, P. Lundberg, E. M. Larsson, and A. Tisell, “Quantitative MRI for analysis of peritumoral edema in malignant gliomas,” *PLoS ONE*, vol. 12, no. 5, e0177135, 2017.
- [153] A. R. Hoy, S. R. Kecsekemeti, and A. L. Alexander, “Free water elimination diffusion tractography: A comparison with conventional and fluid-attenuated inversion recovery, diffusion tensor imaging acquisitions,” *J Magn Reson Imaging*, vol. 42, no. 6, pp. 1572–1581, 2015.

- [154] C. Pierapoli, S. Marengo, G. Rohde, D. K. Jones, and A. S. Barnett, "Analyzing the contribution of cardiac pulsation to the variability of quantities derived from the diffusion tensor," in *ISMRM*, 2003.
- [155] C. Pierapoli and D. K. Jones, "Removing CSF contamination in brain DT-MRIs by using a two-compartment tensor model," in *ISMRM*, 2004.
- [156] B. Scherrer and S. K. Warfield, "Why multiple b-values are required for multi-tensor models: Evaluation with a constrained log-Euclidean model," in *2010 IEEE International Symposium on Biomedical Imaging: From Nano to Macro*, 2010.
- [157] O. Pasternak, N. Sochen, Y. Gur, N. Intrator, and Y. Assaf, "Free water elimination and mapping from diffusion MRI," *Magn Reson Med*, vol. 62, no. 3, pp. 717–730, 2009.
- [158] Y. Gur, O. Pasternak, and N. Sochen, "Fast GL(n)-invariant framework for tensors regularization," *Int J Comput Vis*, vol. 85, no. 211, pp. 211–222, 2009.
- [159] R. Kimmel, N. Sochen, and R. Malladi, "From high energy physics to low level vision," *Lecture Notes in Computer Science. Scale-Space Theory in Computer Vision. Springer*, vol. 1252, pp. 236–247, 1997.
- [160] O. Pasternak, N. Sochen, and P. J. Basser, "The effect of metric selection on the analysis of diffusion tensor MRI data," *Neuroimage*, vol. 49, no. 3, pp. 2190–2204, 2010.
- [161] A. A. O. Ismail *et al.*, "Characterizing peritumoral tissue using free water elimination in clinical DTI," *Brainlesion: Glioma, Multiple Sclerosis, Stroke and Traumatic Brain Injuries - MICCAI, BrainLes 2018*, vol. LNCS 11383, no. Pt 1, pp. 123–131, 2018.
- [162] L. Weninger, C. H. Na, K. Jütten, and D. Merhof, "Analyzing the effects of free water modeling by deep learning on diffusion MRI structural connectivity estimates in glioma patients," *PLoS ONE*, vol. 15, no. 9, e0239475, 2020.
- [163] M.-C. Metz *et al.*, "Predicting glioblastoma recurrence from preoperative MR scans using fractional-anisotropy maps with free-water suppression," *Cancers*, vol. 12, no. 3, p. 728, 2020.
- [164] M. Molina-Romero, B. Wiestler, P. Gómez, M. I. Menzel, and B. H. Menze, "Deep learning with synthetic diffusion MRI data for free-water elimination in glioblastoma cases," in *Medical Image Computing and Computer Assisted Intervention – MICCAI 2018*, A. Frangi, J. Schnabel, C. Davatzikos, C. Alberola-López, and G. Fichtinger, Eds., vol. 11072, 2018, pp. 98–106.
- [165] S. Gong *et al.*, "Free water modeling of peritumoral edema using multi-fiber tractography: Application to tracking the arcuate fasciculus for neurosurgical planning," *PLoS ONE*, vol. 13, no. 5, e0197056, 2018.
- [166] Z. Chen *et al.*, "Reconstruction of the arcuate fasciculus for surgical planning in the setting of peritumoral edema using two-tensor unscented Kalman filter tractography," *Neuroimage Clin*, vol. 7, pp. 815–822, 2015.

- [167] C. R. McDonald *et al.*, "Recovery of white matter tracts in regions of peritumoral FLAIR hyperintensity using restriction spectrum imaging," *AJNR Am J Neuroradiol*, vol. 34, no. 6, pp. 1157–1163, 2013.
- [168] M. A. Prah *et al.*, "Spatial discrimination of glioblastoma and treatment effect with histologically-validated perfusion and diffusion magnetic resonance imaging metrics," *J Neurooncol*, vol. 136, no. 1, pp. 13–21, 2018.
- [169] D. A. Rubin, "MRI and ultrasound of the hands and wrists in rheumatoid arthritis. Part I. Imaging findings," *Skeletal Radiol*, vol. 48, no. 5, pp. 677–695, 2019.
- [170] D. A. Rubin, "MRI and ultrasound of the hands and wrists in rheumatoid arthritis. Part II. Added clinical value," *Skeletal Radiol*, vol. 48, no. 6, pp. 837–857, 2019.
- [171] L. Tang and X. J. Zhou, "Diffusion MRI of cancer: From high to low b-values," *J Magn Reson Imaging*, vol. 49, no. 1, pp. 23–40, 2018.
- [172] R. E. Petty *et al.*, "International League of Associations for Rheumatology classification of juvenile idiopathic arthritis: Second revision, Edmonton, 2001," *J Rheumatol*, vol. 31, no. 2, pp. 390–392, 2004.
- [173] R. A. Hauser, S. Schroeder, E. Cannizzaro, L. Muller, C. J. Kellenberger, and R. K. Saurenmann, "How important is early magnetic resonance imaging of the temporomandibular joint for the treatment of children with juvenile idiopathic arthritis: A retrospective analysis," *Pediatric Rheumatol*, vol. 12, no. 36, pp. 1–7, 2014.
- [174] L. Müller *et al.*, "Early diagnosis of temporomandibular joint involvement in juvenile idiopathic arthritis: A pilot study comparing clinical examination and ultrasound to magnetic resonance imaging," *Rheumatology*, vol. 48, no. 6, pp. 680–685, 2009.
- [175] T. Karhullahti, H. Ylijoki, and O. Rönning, "Mandibular condyle lesions related to age at onset and subtypes of juvenile rheumatoid arthritis in 15-year-old children," *Scand J Dent Res*, vol. 101, no. 5, pp. 332–338, 1993.
- [176] S. Jank *et al.*, "Sonographic investigation of the temporomandibular joint in patients with juvenile idiopathic arthritis: A pilot study," *Arthritis Rheum*, vol. 57, no. 2, pp. 213–218, 2007.
- [177] M. V. Ronchesel *et al.*, "Temporomandibular joint and mandibular growth alterations in patients with juvenile rheumatoid arthritis," *J Rheumatol*, vol. 22, no. 10, pp. 1956–1961, 1995.
- [178] A. M. Selvaag, H. A. Aulie, V. Lilleby, and B. Flatø, "Disease progression into adulthood and predictors of long-term active disease in juvenile idiopathic arthritis," *Ann Rheum Dis*, vol. 75, no. 1, pp. 190–195, 2016.
- [179] F. Oliveira-Ramos *et al.*, "Juvenile idiopathic arthritis in adulthood: Fulfilment of classification criteria for adult rheumatic diseases, long-term outcomes and predictors of inactive disease, functional status and damage," *RMD Open*, vol. 2, no. 2, e000304, 2016.

- [180] M. Twilt, S. M. L. M. Moberers, L. R. Arends, R. ten Cate, and L. van Suijlekom-Smit, "Temporomandibular involvement in juvenile idiopathic arthritis," *J Rheumatol*, vol. 31, no. 7, pp. 1418–1422, 2004.
- [181] S. Suenaga, S. Hamamoto, K. Kawano, Y. Higashida, and T. Noikura, "Imaging of the temporomandibular joint in patients with arthrosis: Relationship between contrast enhancement of the posterior disk attachment and joint pain," *AJR Am*, vol. 166, no. 6, pp. 1475–1481, 1996.
- [182] J. Yin, J. Yang, and Q. Guo, "Evaluating the feasibility of an agglomerative hierarchy clustering algorithm for the automatic detection of the arterial input function using DSC-MRI," *PLoS ONE*, vol. 9, no. 6, e100308, 2014.
- [183] S. Chen, Y.-C. Tyan, J.-J. Lai, and C.-C. Chang, "Automated determination of arterial input function for dynamic susceptibility contrast MRI from regions around arteries using independent component analysis," *Radiol Res Pract*, vol. 2016, p. 2 657 405, 2016.
- [184] L. Knutsson *et al.*, "Reduction of arterial partial volume effects for improved absolute quantification of DSC-MRI perfusion estimates: Comparison between tail scaling and prebolus administration," *J Magn Reson Imaging*, vol. 41, no. 4, pp. 903–908, 2015.
- [185] M. Livne *et al.*, "A PET-guided framework supports a multiple arterial input functions approach in DSC-MRI in acute stroke," *J Neuroimaging*, vol. 27, no. 5, pp. 486–492, 2017.
- [186] A. Albi *et al.*, "Free water elimination improves test-retest reproducibility of diffusion tensor imaging indices in the brain: A longitudinal multisite study of healthy elderly subjects," *Hum Brain Map*, vol. 38, no. 1, pp. 12–26, 2017.
- [187] T. Hulsen, "Sharing is caring - data sharing initiatives in healthcare," *Int J Environ Res Public Health*, vol. 17, no. 9, p. 3046, 2020.
- [188] D. Simeon-Dubach and M. K. Henderson, "Opportunities and risks for research biobanks in the COVID-19 era and beyond," *Biopreserv Biobank*, vol. 18, no. 6, pp. 503–510, 2020.
- [189] L. C. Bell *et al.*, "Evaluating multisite rCBV consistency from DSC-MRI imaging protocols and postprocessing software across the NCI quantitative imaging network sites using a digital reference object (DRO)," *Tomography*, vol. 5, no. 1, pp. 110–117, 2019.
- [190] J. L. Boxerman *et al.*, "Consensus recommendations for a dynamic susceptibility contrast MRI protocol for use in high-grade gliomas," *Neuro Oncol*, vol. 22, no. 9, pp. 1262–1275, 2020.
- [191] F. G. Davis, T. A. Dolecek, B. J. McCarthy, and J. L. Villano, "Toward determining the lifetime occurrence of metastatic brain tumors estimated from 2007 United States cancer incidence data," *Neuro Oncol*, vol. 14, no. 9, pp. 1171–1177, 2012.

- [192] J. S. Barnholtz-Sloan, A. E. Sloan, F. G. Davis, F. D. Vignau, P. Lai, and R. E. Sawaya, "Incidence proportions of brain metastases in patients diagnosed (1973 to 2001) in the metropolitan Detroit cancer surveillance system," *J Clin Oncol*, vol. 22, no. 14, pp. 2865–2872, 2004.
- [193] L. J. Schouten, J. Rutten, H. A. M. Huveneers, and A. Twijnstra, "Incidence of brain metastases in a cohort of patients with carcinoma of the breast, colon, kidney, and lung and melanoma," *Cancer*, vol. 94, no. 10, pp. 2698–2705, 2002.
- [194] M. E. Linskey *et al.*, "The role of stereotactic radiosurgery in the management of patients with newly diagnosed brain metastases: A systematic review and evidence-based clinical practice guideline," *J Neurooncol*, vol. 96, no. 1, pp. 45–68, 2010.
- [195] D. Hartgerink *et al.*, "Stereotactic radiosurgery in the management of patients with brain metastases of non-small cell lung cancer: Indications, decision tools and future directions," *Front Oncol*, vol. 9, no. 8, p. 154, 2018.
- [196] M. Yamamoto *et al.*, "Stereotactic radiosurgery for patients with multiple brain metastases (JLGK0901): A multi-institutional prospective observational study," *Lancet Oncol*, vol. 15, no. 4, pp. 387–395, 2014.
- [197] R. Jakubovic *et al.*, "Magnetic resonance imaging-based tumour perfusion parameters are biomarkers predicting response after radiation to brain metastases," *Clin Oncol (R Coll Radiol)*, vol. 26, no. 11, pp. 704–712, 2014.
- [198] J. R. Knitter *et al.*, "Interval change in diffusion and perfusion MRI parameters for the assessment of pseudoprogression in cerebral metastases treated with stereotactic radiation," *AJR Am J Roentgenol*, vol. 211, no. 1, pp. 168–175, 2018.
- [199] M. Essig, M. Wasch Kies, F. Wenz, J. Debus, H. R. Hentrich, and M. V. Knopp, "Assessment of brain metastases with dynamic susceptibility-weighted contrast-enhanced MR imaging: Initial results," *Radiology*, vol. 228, no. 1, pp. 193–199, 2003.
- [200] Q. T. Ostrom *et al.*, "The epidemiology of glioma in adults: A "state of the science" review," *Neuro-Oncol*, vol. 16, no. 7, pp. 896–913, 2014.
- [201] Q. T. Ostrom *et al.*, "CBTRUS statistical report: Primary brain and other central nervous system tumours diagnosed in the United States in 2012-2016," *Neuro-Oncol*, vol. 21, no. Supplement 5, pp. v1–v100, 2019.
- [202] E. Crocetti *et al.*, "Epidemiology of glial and non-glial brain tumours in Europe," *Eur J Cancer*, vol. 48, no. 10, pp. 1532–1542, 2012.
- [203] L. El-Serougy, A. A. K. A. Razeq, A. Ezzat, H. Eldawoody, and A. El-Morsy, "Assessment of diffusion tensor imaging metrics in differentiation low-grade from high grade gliomas," *Neuroradiol J*, vol. 29, no. 5, pp. 400–407, 2016.
- [204] H. Y. Lee *et al.*, "Diffusion tensor imaging for glioma grading at 3-T magnetic resonance imaging," *J Comput Assist Tomogr*, vol. 32, no. 2, pp. 298–303, 2008.
- [205] A. Jakab, P. Molnár, M. Emri, and E. Berényi, "Glioma grade assessment by using histogram analysis of diffusion tensor imaging-derived maps," *Neuroradiology*, vol. 53, no. 7, pp. 483–491, 2011.

- [206] K. S. Holly *et al.*, “High-grade glioma exhibit higher peritumoral fractional anisotropy and lower mean diffusivity than intracranial metastases,” *Front Surg*, vol. 4, no. 18, pp. 1–10, 2017.
- [207] S. E. Maier, Y. Sun, and R. V. Mulkern, “Diffusion imaging of brain tumors,” *NMR Biomed*, vol. 23, no. 7, pp. 849–864, 2010.
- [208] O. Macíček *et al.*, “Time-efficient perfusion imaging using DCE- and DSC-MRI,” *Measure Sci Rev*, vol. 18, no. 6, pp. 262–271, 2018.
- [209] S. Demant *et al.*, “3D analysis of facial asymmetry in subjects with juvenile idiopathic arthritis,” *Rheumatology*, vol. 50, no. 3, pp. 586–592, 2011.
- [210] A. Bjørnerud, A. G. Sorensen, K. Mouridsen, and K. E. Emblem, “T1- and T2*-dominant extravasation correction in DSC-MRI: part I-theoretical considerations and implications for assessment of tumor hemodynamic properties,” *J Cereb Blood Flow Metab*, vol. 31, pp. 2041–2053, 2011.
- [211] A. Bjørnerud and K. E. Emblem, “A fully automated method for quantitative cerebral hemodynamic analysis using DSC-MRI,” *J Cereb Blood Flow Metab*, vol. 30, pp. 1066–1078, 2010.
- [212] D. P. Shamonin, E. E. Bron, B. P. F. Lelieveldt, M. Smits, S. Klein, and M. Staring, “Fast parallel image registration on CPU and GPU for diagnostic classification of Alzheimer’s disease,” *Front Neuroinform*, vol. 7, pp. 1–15, 2014.
- [213] S. Klein, M. Staring, K. Murphy, M. A. Viergever, and J. P. W. Pluim, “Elastix: A toolbox for intensity based medical image registration,” *IEEE Trans Med Imaging*, vol. 29, pp. 196–205, 2010.
- [214] R. van ’t Klooster. “Parameter file database: Par0018.” (2013), [Online]. Available: https://github.com/SuperElastix/ElastixModelZoo/blob/master/models/Par0018/Par0018_3D_affine_MI.txt (visited on 02/05/2021).
- [215] P. A. Yushkevich *et al.*, “User-guided 3D active contour segmentation of anatomical structures: Significantly improved efficiency and reliability,” *Neuroimage*, vol. 31, no. 3, pp. 1116–1128, 2006.
- [216] M. Jenkinson and S. Smith, “A global optimization method for robust affine registration of brain images,” *Med Image Anal*, vol. 5, no. 2, pp. 143–156, 2001.
- [217] M. Jenkinson, C. F. Beckmann, T. E. J. Behrens, M. W. Woolrich, and S. M. Smith, “FSL,” *Neuroimage*, vol. 62, pp. 782–790, 2012.
- [218] Y. Zhang, M. Brady, and S. Smith, “Segmentation of brain MR images through a hidden Markov random field model and the expectation-maximization algorithm,” *IEEE Trans Med Imag*, vol. 29, pp. 45–57, 2001.
- [219] W. Penny, K. Friston, J. Ashburner, and S. Kiebel, *Statistical parametric mapping: The Analysis of functional brain images*. London: Academic Press, 2006, pp. 143–156.
- [220] F.-C. Yeh. “Zenodo.” (2021), [Online]. Available: <http://doi.org/10.5281/zenodo.4764264> (visited on 10/15/2021).

- [221] F.-C. Yeh, "Shape analysis of the human association pathways," *Neuroimage*, vol. 223, p. 117 329, 2020.
- [222] D. Parker *et al.*, "Freewater estimator using iNtErpolated iniTialization (FERNET): Characterizing peritumoral edema using clinically feasible diffusion MRI data," *PLoS One*, vol. 15, no. 5, e0233645, 2020.
- [223] N. Otsu, "A threshold selection method from gray level histograms," *IEEE Trans Syst Man Cybern*, vol. 9, no. 1, pp. 62–66, 1979.
- [224] C. M. Bauer, L. E. Zajac, B. B. Koo, R. J. Killiany, and L. B. Merabet, "Age-related changes in structural connectivity are improved using," *J Neurosci Methods*, vol. 288, pp. 45–56, 2017.
- [225] P. N. Taylor, Y. Wang, and M. Kaiser, "Within brain area tractography suggests local modularity using high resolution connectomics," *Sci Rep*, vol. 7, p. 39 859, 2017.
- [226] B. Bigham, S. A. Zamanpour, F. Zemorshidi, F. Boroumand, and H. Zare, "Identification of superficial white matter abnormalities in Alzheimer's disease and mild cognitive impairment using diffusion tensor imaging," *J Alzheimers Dis Rep*, vol. 4, no. 1, pp. 49–59, 2020.
- [227] E. Kontopodis, G. Kanli, G. C. Manikis, S. Van Cauter, and K. Marias, "Assessing treatment response through generalized pharmacokinetic modeling of DCE-MRI data," *Cancer Inform*, vol. 14, no. Suppl 4, pp. 41–51, 2015.
- [228] X. Wang *et al.*, "A comparative study of two-compartment exchange models for dynamic contrast-enhanced MRI in characterizing uterine cervical carcinoma," *Contrast Media Mol Imaging*, vol. 2019, p. 3 168 416, 2019.
- [229] A. S. Malamas, E. Jin, Q. Zhang, J. Haaga, and Z.-R. Lu, "Anti-angiogenic effects of bumetanide revealed by DCE-MRI with a biodegradable macromolecular contrast agent in a colon cancer model," *Contrast Media Mol Imaging*, vol. 32, no. 9, pp. 3029–3043, 2015.
- [230] E. K. Weidman *et al.*, "Evaluating permeability surface-area product as a measure of blood-brain barrier permeability in a murine model," *AJNR Am J Neuroradiol*, vol. 37, no. 7, pp. 1267–1274, 2016.
- [231] S. H. Lee, K. Hayano, A. X. Zhu, D. V. Sahani, and H. Yoshida, "Water-exchange-modified kinetic parameters from dynamic contrast-enhanced mri as prognostic biomarkers of survival in advanced hepatocellular carcinoma treated with antiangiogenic monotherapy," *PLoS One*, vol. 10, no. 9, e0136725, 2015.
- [232] H. B. W. Larsson, M. B. Vestergaard, U. Lindberg, H. K. Iversen, and S. P. Cramer, "Brain capillary transit time heterogeneity in healthy volunteers measured by dynamic contrast-enhanced T1-weighted perfusion MRI," *J Magn Reson Imaging*, vol. 45, no. 6, pp. 1809–1820, 2017.
- [233] C. C. Colin *et al.*, "Exercise-stimulated arterial transit time in calf muscles measured by dynamic contrast-enhanced magnetic resonance imaging," *Physiol Rep*, vol. 7, no. 1, e13978, 2019.

- [234] W. Ceelen *et al.*, “Recombinant human erythropoietin alpha modulates the effects of radiotherapy on colorectal cancer microvessels,” *Br J Cancer*, vol. 96, no. 5, pp. 692–300, 2007.
- [235] I. S. Haldorsen *et al.*, “Increased microvascular proliferation is negatively correlated to tumour blood flow and is associated with unfavourable outcome in endometrial carcinomas,” *Br J Cancer*, vol. 110, no. 1, pp. 107–114, 2014.
- [236] I. S. Haldorsen *et al.*, “Dynamic contrast-enhanced MRI in endometrial carcinoma identifies patients at increased risk of recurrence,” *Eur Radiol*, vol. 23, no. 10, pp. 2916–2925, 2013.
- [237] A. Steins *et al.*, “Rapid stromal remodeling by short-term VEGFR2 inhibition increases chemotherapy delivery in esophagogastric adenocarcinoma,” *Mol Oncol*, vol. 14, no. 4, pp. 704–720, 2020.
- [238] M. C. Schabel *et al.*, “Functional imaging of the non-human primate placenta with endogenous blood oxygen level-dependent contrast,” *Magn Reson Med*, vol. 76, no. 5, pp. 1551–1562, 2016.
- [239] J. O. Lo *et al.*, “Vitamin C supplementation ameliorates the adverse effects of nicotine on placental hemodynamics and histology in non-human primates,” *Am J Obstet Gynecol*, vol. 212, no. 3, 307.e1–370.e8, 2015.
- [240] A. E. Frias *et al.*, “Using dynamic contrast enhanced MRI to quantitatively characterize maternal vascular organization in the primate placenta,” *Magn Reson Med*, vol. 73, no. 4, pp. 1570–1578, 2016.
- [241] R. L. Jensen, M. L. Mumert, D. L. Gillespie, A. Y. Kinney, M. C. Schabel, and K. L. Salzman, “Preoperative dynamic contrast-enhanced MRI correlates with molecular markers of hypoxia and vascularity in specific areas of intratumoral microenvironment and is predictive of patient outcome,” *Neuro Oncol*, vol. 16, no. 2, pp. 280–291, 2014.
- [242] D. L. Buckley, “Uncertainty in the analysis of tracer kinetics using dynamic contrast-enhanced T1-weighted MRI,” *Magn Reson Med*, vol. 47, no. 3, pp. 601–606, 2002.
- [243] O. Keunen *et al.*, “Anti-VEGF treatment reduces blood supply and increases tumor cell invasion in glioblastoma,” *Proc Natl Acad Sci U S A*, vol. 108, no. 9, pp. 3749–3754, 2011.
- [244] T. R. Wittenborn and M. R. Horsman, “Targeting tumour hypoxia to improve outcome of stereotactic radiotherapy,” *Acta Oncol*, vol. 54, no. 9, pp. 1385–1392, 2015.
- [245] D. Kawahara, L. Wu, and Y. Watanabe, “Optimization of irradiation interval for fractionated stereotactic radiosurgery by a cellular automata model with reoxygenation effects,” *Phys Med Biol*, vol. 65, no. 8, p. 085 008, 2020.
- [246] R. F. Bajas, J. S. Chang, P. Sneed, M. R. Segal, M. W. McDermott, and S. Cha, “Distinguishing recurrent intra-axial metastatic tumor from radiation necrosis following gamma knife radiosurgery using dynamic susceptibility-weighted contrast-enhanced perfusion MR imaging,” *AJNR Am J Neuroradiol*, vol. 30, no. 2, pp. 367–372, 2009.

- [247] F. Cicone *et al.*, “Accuracy of F-DOPA PET and perfusion-MRI for differentiating radionecrotic from progressive brain metastases after radiosurgery,” *Eur J Nucl Med mol Imaging*, vol. 42, no. 1, pp. 103–111, 2015.
- [248] F. W. A. Hoefnagels, F. J. Lagerwaard, and E. Sanches, “Radiological progression of cerebral metastases after radiosurgery: Assessment of perfusion MRI for differentiating between necrosis and recurrence,” *J Neurol*, vol. 256, no. 6, pp. 878–887, 2009.
- [249] M.-T. Chuang, Y.-S. Liu, Y.-S. Tsai, Y.-C. Chen, and C.-K. Want, “Differentiating radiation-induced necrosis from recurrent brain tumor using MR perfusion and spectroscopy: A meta-analysis,” *PLoS ONE*, vol. 11, no. 1, e0141438, 2016.
- [250] K. Mitsuya *et al.*, “Perfusion weighted magnetic resonance imaging to distinguish the recurrence of metastatic brain tumors from radiation necrosis after stereotactic radiosurgery,” *J Neurooncol*, vol. 99, no. 1, pp. 81–88, 2010.
- [251] I. Digernes *et al.*, “Brain metastases with poor vascular function are susceptible to pseudoprogression after stereotactic radiation surgery,” *Adv Radiat Oncol*, vol. 17, no. 3(4), pp. 559–567, 2018.
- [252] M.-A. Weber *et al.*, “Assessment of irradiated brain metastases by means of arterial spin-labeling and dynamic susceptibility-weighted contrast-enhanced perfusion MRI: Initial results,” *Invest Radiol*, vol. 39, no. 5, pp. 277–287, 2004.
- [253] Y. Wan, R. Rahmat, and S. J. Price, “Deep learning for glioblastoma segmentation using preoperative magnetic resonance imaging identifies volumetric features associated with survival,” *Acta Neurochir*, vol. 162, no. 12, pp. 3067–3080, 2020.
- [254] K. Kobayashi, M. Miyake, M. Takashi, and R. Hamamoto, “Observing deep radiomics for the classification of glioma grades,” *Sci Rep*, vol. 11, no. 1, pp. 1–13, 2021.
- [255] P. Kickingeder *et al.*, “Automated quantitative tumour response assessment of MRI in neuro-oncology with artificial neural networks: A multicentre, retrospective study,” *Lancet Oncol*, vol. 20, no. 5, pp. 728–740, 2019.
- [256] J. B. P. O’Connor, A. Jackson, G. J. M. Parker, and G. J. Jayson, “DCE-MRI biomarkers in the clinical evaluation of antiangiogenic and vascular disrupting agents,” *Br J Cancer*, vol. 96, no. 2, pp. 189–195, 2007.
- [257] A. Ishii *et al.*, “Histological characterization of the tumorigenic “peri-necrotic niche” harboring quiescent stem-like tumor cells in glioblastoma,” *PLoS ONE*, vol. 11, no. 1, e0147366, 2016.
- [258] S. Liu *et al.*, “Relationship between necrotic patterns in glioblastoma and patient survival: Fractal dimension and lacunarity analyses using magnetic resonance imaging,” *Sci Rep*, vol. 7, no. 1, p. 8302, 2017.
- [259] J. P. B. O’Connor, S. P. Robinson, and J. C. Waterton, “Imaging tumour hypoxia with oxygen-enhanced MRI and BOLD MRI,” *Br J Radiol*, vol. 92, no. 1096, p. 20180642, 2019.

- [260] B. J. Guo, Z. L. Yang, and L. J. Zhang, "Gadolinium deposition in brain: Current scientific evidence and future perspectives," *Front Mol Neurosci*, vol. 11, p. 335, 2018.
- [261] M. E. Mayerhoefer *et al.*, "Introduction to radiomics," *J Nucl Med*, vol. 61, no. 4, pp. 488–495, 2020.
- [262] J. Y. Kim *et al.*, "Incorporation diffusion- and perfusion-weighted MRI into a radiomics model improves diagnostic performance for pseudoprogression in glioblastoma patients," *Neuro Oncol*, vol. 21, no. 3, pp. 404–414, 2019.
- [263] C. Su *et al.*, "Radiomics based multicontrast MRI can precisely differentiate among glioma subtypes and predict tumour-proliferative behaviour," *Eur Radiol*, vol. 29, no. 4, pp. 1956–1996, 2019.
- [264] N. M. Braman *et al.*, "Intratumoral and peritumoral radiomics for the pretreatment prediction of pathological complete response to neoadjuvant chemotherapy based on breast DCE-MRI," *Breast Cancer Res*, vol. 19, no. 1, p. 57, 2017.
- [265] J. Wang *et al.*, "A radiomics model based on DCE-MRI and DWI may improve the prediction of estimating IDH1 mutation and angiogenesis in gliomas," *Eur J Radiol*, vol. 147, p. 110 141, 2022.

Appendix A: Paper 1

Effects of Motion Correction, Sampling Rate and Parametric Modelling in Dynamic Contrast Enhanced MRI of the Temporomandibular Joint in Children Affected With Juvenile Idiopathic Arthritis



Original Contribution

Effects of motion correction, sampling rate and parametric modelling in dynamic contrast enhanced MRI of the temporomandibular joint in children affected with juvenile idiopathic arthritis

Lea Starck^{a,b,*}, Erling Andersen^{b,c}, Ondřej Macíček^d, Oskar Angenete^{e,f}, Thomas A. Augdal^{g,h}, Karen Rosendahl^h, Radovan Jirík^d, Renate Grüner^{a,b,i}

^a Department of Physics and Technology, University of Bergen, Bergen, Norway

^b Mohn Medical Imaging and Visualization Centre, Haukeland University Hospital, Bergen, Norway

^c Department of Clinical Engineering, Haukeland University Hospital, Bergen, Norway

^d Institute of Scientific Instruments of the Czech Academy of Sciences, Brno, Czechia

^e Department of Radiology and Nuclear Medicine, St. Olav Hospital HF, Trondheim, Norway

^f Department of Circulation and Medical Imaging, Norwegian University of Science and Technology, Trondheim, Norway

^g Section for Paediatric Radiology, University Hospital of North Norway, Tromsø, Norway

^h Department of Clinical Medicine, UiT The Arctic University of Norway, Norway

ⁱ Department of Radiology, Haukeland University Hospital, Bergen, Norway



ARTICLE INFO

Keywords:

JIA
TMJ
DCE MRI
Sampling rate
Motion correction

ABSTRACT

The temporomandibular joint (TMJ) is typically involved in 45–87% of children with Juvenile Idiopathic Arthritis (JIA). Accurate diagnosis of JIA is difficult as various clinical tests, including MRI, disagree. The purpose of this study is to optimize the methodological aspects of Dynamic Contrast Enhanced (DCE) MRI of the TMJ in children. In this cross-sectional study, including data from 73 JIA affected children, aged 6–15 years, effects of motion correction, sampling rate and parametric modelling on DCE-MRI data is investigated. Consensus among three radiologists determined the regions of interest. Quantitative perfusion parameters were estimated using four perfusion models; the Adiabatic Approximation to Tissue Homogeneity (AATH), Distributed Capillary Adiabatic Tissue Homogeneity (DCATH), Gamma Capillary Transit Time (GCTT) and Two Compartment Exchange (2CXM) models. Effects of motion correction were evaluated by a sum of least squares between corrected raw data and the GCTT model. The effect of systematically down sampling the raw data was tested. The sum of least squares was computed across all pharmacokinetic models. Relative difference perfusion parameters between the left and right TMJ were used for an unsupervised k-means based stratification of the data based on a principal component analysis, as well as for a supervised random forest classification. Diagnostic sensitivity and specificity were computed relative to structural image scorings. Paired sample *t*-tests, as well as ANOVA tests, were used (significant threshold: $p < 0.05$) with Tukeys post hoc test. High-level elastic motion correction provides the best least square fit to the GCTT model (percentual improvement: 72–84%). A 4 s sampling rate captures more of the potentially disease relevant signal variations. The various parametric models all leave comparable residues (relative standard deviation: 3.4%). In further evaluation of DCE-MRI as a potential diagnostic tool for JIA a high-level elastic motion correction scheme should be adopted, with a sampling rate of at least 4 s. Results suggest that DCE-MRI data can be a valuable part in JIA diagnostics in the TMJ.

1. Introduction

Juvenile Idiopathic Arthritis (JIA) encompasses all cases of arthritis

of unknown origin with onset prior to the 16th birthday, persisting for a minimum of 6 weeks [1]. Reported JIA prevalence varies between 0.07 and 4.01 per 1000 children [2]. Continuation of active disease into

* Corresponding author at: Allégaten 55, 5007 Bergen, Norway

E-mail addresses: lea.starck@uib.no (L. Starck), erling.andersen@helse-bergen.no (E. Andersen), macicek@isibrno.cz (O. Macíček), oskar.angenete@stolav.no (O. Angenete), thomas.angell.augdal@unn.no (T.A. Augdal), karen.rosendahl@unn.no (K. Rosendahl), jirik@isibrno.cz (R. Jirík), eli.renate.gruner@helse-bergen.no (R. Grüner).

<https://doi.org/10.1016/j.mri.2020.12.014>

Received 3 September 2020; Received in revised form 7 December 2020; Accepted 20 December 2020

Available online 13 January 2021

0730-725X/© 2020 The Author(s). Published by Elsevier Inc. This is an open access article under the CC BY license (<http://creativecommons.org/licenses/by/4.0/>).

adulthood has, depending on the study, been reported for 41% and 67% of the patient cohort [3,4]. Early effective treatment is contingent on early detection of the disease, yet therapeutic interventions are often hampered by differing methodologies and asymptomatic temporomandibular joints (TMJs) [2,5,6]. Inflammation in the (TMJ) are frequently reported in cases of JIA, and it is estimated that the TMJ may be involved in between 45% and 87% of the cases [5], [7–10].

Methods for detecting JIA-involvement of the TMJ include structural imaging (radiographs, ultrasound, computed tomography and MRI) and clinical assessment including restricted mouth opening, mandibular deviation during mouth opening, facial asymmetry, and history of pain. [5], [10–13]. Reading of structural MRI images post contrast injection (i.e. T1 static) is currently one of the most sensitive assessment methods [8,9], [11]. Even though a variety of MRI techniques for examination of the temporomandibular joint exist, static images remain the gold standard. The TMJ may also be studied under the hypothesis that the inflammation is an origin of pain, accompanied by increased vascularity [8,14,15]. In addition to the MRI techniques recently reviewed [16], the TMJ may also be assessed with Dynamic Contrast Enhanced (DCE)-MRI. To capture the increased vascularity, the microvasculature may be assessed by measuring the change in signal intensity due to the passing of a contrast agent in time (i.e. T1 dynamic) [8]. DCE-MRI dynamics can be studied by means of semi-quantitative measures derived directly from the signal intensity time curves [17–19] or by tracer kinetic modelling [20,21]. No standard pipeline to process the DCE-MRI data in the temporomandibular joint exists. There are several models that can be applied in tracer kinetic modelling. A general feature of these approaches is that the capillary bed is regarded as a box (being the imaged tissue voxel or region of interest) with an inlet and an outlet, where blood containing contrast agent flows in and out, respectively. The contrast agent may also diffuse back and forth across the capillary wall. It is assumed that the system is linear and time invariant, and that contrast agent is neither generated nor destroyed in the system [21,22]. In general, the change in the measured contrast agent concentration within the capillary bed, $C(t)$, is the sum of all in-fluxes with the sum of all out-fluxes subtracted, Eq. (1),

$$\frac{dC(t)}{dt} = \sum_{in} J_i(t) - \sum_{out} J_o(t) \quad (1)$$

where $J_i(t)$ is the in-flux and $J_o(t)$ is the out-flux [21]. The concentration at the input of the voxel is called an arterial input function (AIF). The measured tracer concentration, $C(t)$, is determined by the impulse response of the system and is given by the convolution in Eq. (2),

$$C(t) = \int_0^t C_p(\tau) \cdot i(t - \tau) d\tau = [x * i](t) \quad (2)$$

where $C_p(t)$ is the AIF and $i(t)$ is the impulse response [21]. The impulse response is given by the specific model describing the microvasculature. Each model has several analytical parameters that are varied to provide the best fit between the left- and right-hand side of Eq. (2).

The aim of the current study is to explore the feasibility of DCE-MRI in the diagnosis of TMJ involvement in JIA. Methodological aspects of motion correction, signal sampling and parametric modelling are evaluated. Three levels of motion correction were applied and the results on the data examined and the sampling rate capturing the dynamics of the TMJ is investigated, [23]. Additionally, the ability of the Adiabatic Approximation to the Tissue Homogeneity Model (AATH), Distributed Capillary Adiabatic Tissue Homogeneity Model (DCATH), Gamma Capillary Transit Time Model (GCTT) and Two Compartment Exchange Model (2CXM) to produce parameters that are able to distinguish between presumed healthy and affected TMJ are examined. Finally, it is discussed if DCE-MRI can be of added value in the diagnosis of JIA affected TMJ.

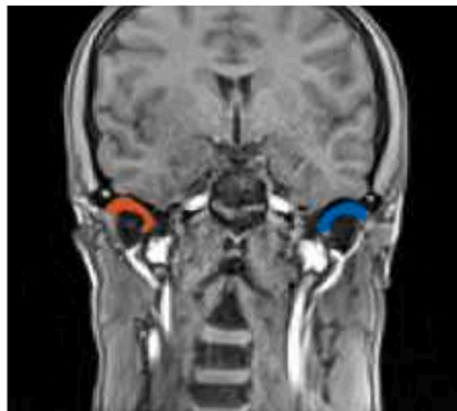


Fig. 1. Regions of interest, covering left (blue) and right (red) TMJ. (For interpretation of the references to colour in this figure legend, the reader is referred to the web version of this article.)

2. Material and methods

2.1. Data collection

All data were acquired and used in agreement with ethical approval from REK Vest. Written informed consent was obtained from their care takers and participants older than 12 years. DCE-MRI was included as part of an extensive, longitudinal, multicentre study on quality of life, oral health and imaging in JIA (the Norwegian study in JIA, Nor JIA), in a larger group of children. The analysed data consists of DCE-MRI acquisitions of the TMJ in a subset of 73 children, aged 6–15 years, diagnosed with JIA with possible TMJ involvement. The data constitutes a balanced subset of patients ranging from radiologically severe arthritis to cases with only subtle findings. With a sampling rate of 4 s, 60 image volumes (160x160x16 image matrices) were acquired from each participant, using a MAGNETOM Skyra 3 T system (Siemens Healthineers, Erlangen, Germany), using a 64-channel head coil and a 3D-FLASH sequence (TR/TE/FA = 4 ms/1 ms/9°). The contrast agent Gd-DOTA i.e. Dotarem® (Guerbet, Villepinte, France) was injected at a rate of 5 mL/s, at 10 s after acquisition start, using a power injector and a subsequent saline injection. The MRI data was collected at three study sites, using identical acquisition parameters. Clinical scores derived from assessment of structural MR images determined a measurement of likelihood of affected and unaffected TMJs. The assessment was performed by a by an expert paediatric radiologist. These scores were available from the local site only, comprising 52 participants. Among these 11 participants were deemed to have affected TMJ, 41 participants to have unaffected TMJ.

2.2. Data processing

Regions of interest were defined by manually selected masks, covering the left and right synovial TMJ, respectively, in the 5th imaged volume (acquired 20 s after acquisition start), Fig. 1. These were based on a consensus among three radiologists with between 5 and 15 years of experience. The DCE-MRI was acquired in coronal plane but several other acquisitions in both sagittal and coronal plane were also available to the image readers. When drawing the ROIs (on the coronal DCE-acquisition) the involved image readers (trained radiologists) carefully checked the location of the ROI also in sagittal plane, thereby avoiding the retrodiscal area and areas of abundant joint fluid. It is probably not possible to fully separate condylar cartilage from synovium. However,

Table 1

Parameter descriptions. Semi-quantitative (RT , M , S , A) and quantitative (F_p , E , ve , T_c , α^{-1} , σ , BAT and PS) perfusion parameters, estimated by application of the pharmacokinetic models.

Parameter	Unit	Description
RT	s	Time from baseline to the first maximum of relative enhancement curve
M	–	First maximum value of the relative enhancement curve
S	–	Slope of the relative enhancement curve tail
A	–	Area under the relative enhancement curve
F_p	ml/ml/ min	Blood plasma flow
E	–	Extraction fraction
ve	–	Extravascular extracellular fraction
T_c	min	Mean capillary transit time
α^{-1}	–	Width of the capillary transit time distribution
σ	min	Standard deviation of mean transit time
BAT	min	Bolus arrival time (AIF vs ROI delay)
PS	ml/ml min	Permeability surface product

contrast enhancement of the condylar cartilage is not a known marker of active inflammation in TMJ and does therefore not pose a diagnostic problem in this setting.

Relative enhancement curves were extracted from the DCE-MRI data by averaging pixel signal values contained in the regions of interest, subtracted and divided by the baseline signal, (signal - baseline)/baseline. Semi-quantitative perfusion parameters, Table 1 were computed directly from the relative enhancement curves.

Quantitative perfusion parameters, Table 1, were estimated using an inhouse developed MATLAB tool, version R2017a, (MathWorks Inc., Natick, Massachusetts, US). An AIF was not measured for each individual TMJ. Instead, a population-based AIF based on a random sample of 22 participants was used in the analysis. The 22 individual AIFs were selected semi-automatically by choosing voxels with the highest signal peak within a region containing the large brain feeding arteries. By finding delay between peaks, the AIFs were temporally aligned, and a median AIF calculated. The median AIF is composed of two peaks (due to the first and second bolus passage). The final AIF was obtained by a parametric fit and scaling according to the Parker model [24,25].

According to a previous study [26], it is unlikely that both TMJs in one participant are equally affected. In the following, relative parameter difference between the left and right TMJ, Eq. (3), are reported,

$$P_{rel} = \frac{|P_{left} - P_{right}|}{P_{left} + P_{right}} \quad (3)$$

where P_{left} and P_{right} are the parameters derived from the left and right TMJ, respectively and P_{rel} is the ensuing relative parameter difference. Since relative parameter differences between the left and right TMJ are reported the choice of using an identical AIF, in this case a population-based AIF, is motivated by the goal of highlighting the asymmetry between the joints.

2.3. Pharmacokinetic models

The Adiabatic Approximation to the Tissue Homogeneity Model (AATH) assumes a plug-flow of the blood through the intravascular space, so that the tracer concentration, $c(x, t)$ is dependent on the distance x from the inlet and the time t after the tracer enters at the inlet. The extravascular extracellular space (EES) is modelled as a single compartment [22], [27–29], and the contrast agent is assumed to cross the capillary wall only at the outlet (adiabatic approximation). Exchange of the contrast agent between the intra- and extra-vascular space is assumed in both directions.

Since there is both many capillaries and EES inside a DCE-MRI voxel, there will be a variation in transit times inside of each voxel. This is taken into account by the Distributed Capillary Adiabatic Tissue

Homogeneity Model (DCATH), which measures the contrast agent concentration in a voxel as a sum of concentrations in the capillaries in the voxel, iteratively applying either a normal, truncated normal or skewed Gaussian distribution of transit times (in this study the truncated normal distribution was applied). DCATH model thus outputs an additional parameter σ , which is the standard deviation in transit times in a voxel [30].

The Gamma Capillary Transit Time Model (GCTT) also, like the DCATH model, takes into account that a DCE-MRI voxel contains many capillaries of different sizes, causing varying transit times of the contrast agent through the capillaries. However, the GCTT model assumes a gamma distribution of transit times [20]. It can be shown that other tracer kinetic models, such as the Tofts, Extended Tofts, the Two Compartment Exchange Model (2CXM) and the AATH model, are special cases of the GCTT model when different transit time distributions are applied [20]. A special parameter for the GCTT model is α^{-1} , which measures the width of the transit time distribution. α^{-1} varies between 0 and 1, representing the limiting cases of a delta function distribution ($\alpha^{-1} = 0$), corresponding to the AATH model and the exponential function distribution ($\alpha^{-1} = 1$), corresponding to the 2CXM model [20].

2.4. Effects of motion correction

In motion correction, an input image is adjusted to fit a reference image. Three levels of motion correction were applied successively; no image registration, primary (affine) registration and elastic registration. A common parametric approach is to define a transformation which will align an input x image to the reference image, Eq. (4),

$$T(x) = Ax + t \quad (4)$$

where $T(x)$ is the transformation function, A is a matrix containing parameters, that in the case of affine registration allow rotation, scaling and skewing of the input image. The vector t contains parameters causing translation of the input image. The open source software Elastix [31,32] was used to implement a 3D affine registration. Thus, by finding the optimal four times three parameters of A and t , the 3D affine registration should correct for translational or rotational movements of the region of interest (head). The time series volumes were aligned to volume number five, which was acquired 20s after acquisition start. At this time the contrast agent was injected, but not accumulated in the region of interest. This volume was also used to draw the regions of interest, Fig. 1. Initial transformation parameters, as well as other details of the affine registration as applied with the Elastix software [31–33], are defined in a publicly available parameter text file [34].

The time series volumes were expected to exhibit varying levels of contrast, due to changes in tracer concentration in time. Therefore, mutual information [35] was chosen as an alignment quality measure on which to base the cost function of the motion correction transformation. Due to differences in tracer levels, a pixel in the reference image may have an intensity value that differs from the intensity value in the corresponding pixel in the input image. A two-dimensional histogram plot comparing the intensity values of input (x-axis) and reference image (y-axis), respectively, governs the approach. Lower degree of entropy in the histogram plot expresses more accurate image registration [35]. The transformation parameters were optimized using an iterative process dubbed adaptive stochastic gradient descent [31,36].

A second motion correction algorithm was applied on the affine registered images. This was an elastic motion correction scheme, originally developed in-house for registration of kidney images [37]. In the elastic motion correction scheme, the regions of interest (i.e. the gross TMJ volumes) were co-registered to later time points independent from the rest of the image. After registration of the regions of interest, they are re-inserted into the image. The registration is based on co-aligned image intensity gradient vectors in the input and reference image. However, image intensities vary in time due to the passing of contrast agent.

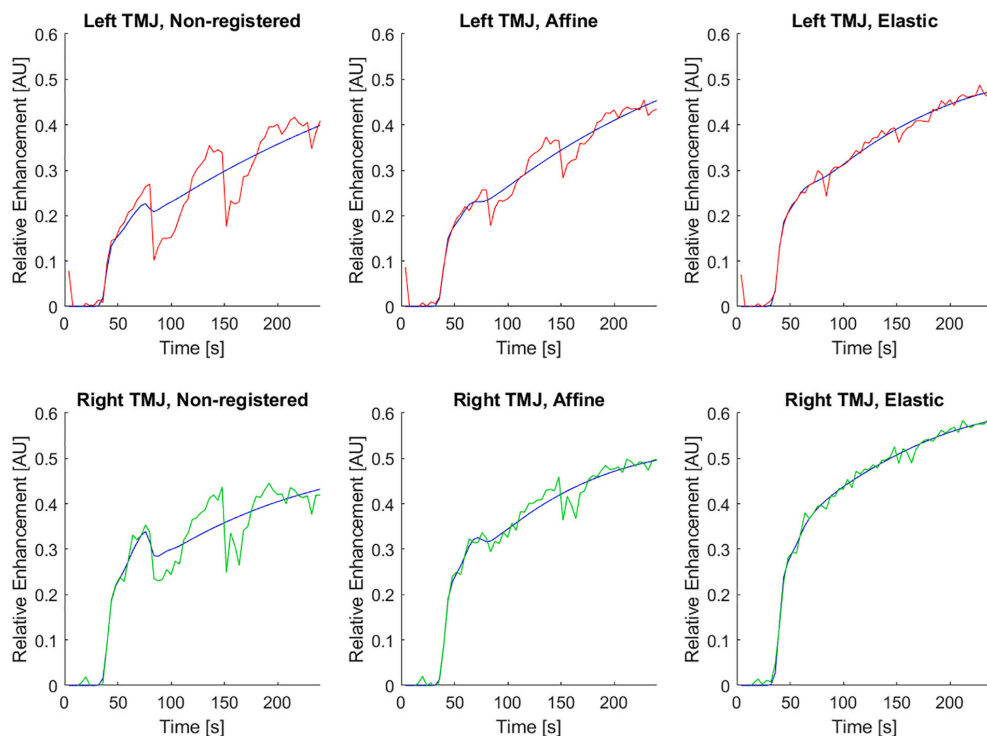


Fig. 2. Effects of three levels of motion correction in a random participant. Relative contrast agent enhancement curves from the left Temporomandibular Joint (TMJ) (upper row, red), right TMJ (lower row, green). DCE-MRI signal with no motion correction (left column), signal after affine motion correction (middle column) and signal after elastic registration (right column). The pharmacokinetic model GCTT is overlaid (blue). (For interpretation of the references to colour in this figure legend, the reader is referred to the web version of this article.)

Therefore, the gradients in the input and reference image are normalized. [37]. Normalizing the gradients meant removing their amplitude, letting the gradient vector entries take on relative values between 0 and 1, while the gradient direction remains the same, such that the geometrical outlines in the region of interest could be exploited.

2.5. Effects of sampling rate

The imaging data was acquired with a 4 s sample rate. Decreased sampling rates were mimicked by re-binning and averaging signal samples into bins of size 2, 3, 4 and 5. The results are relative enhancement curves with temporal resolutions of 8 s, 12 s, 16 s and 20 s, respectively. To investigate the effect of sampling rate on the information in the sampled signal, semi-quantitative relative parameter differences (P_{rel}) were computed and compared across the temporal resolutions.

2.6. Data-driven stratification of participants

Four semi-quantitative parameters and seven quantitative parameter differences were defined, Table 1. Each of the parameters was standardized and principal component analysis performed with Scikit-learn [38].

Using the MATLAB R2017a, (MathWorks Inc., Natick, Massachusetts, US) k-means clustering algorithm, the participants were divided into two groups based on four principal independent components, iteratively minimizing the distance between the vectors and the central point in each group. The k-means algorithm has a random starting point,

and the results would therefore vary slightly in each run. To generate a basis for investigating the likelihood of a participant belonging to the group he or she would be assigned to the algorithm was implemented 1000 times. Finally, each participant was assigned a decimal number between -1 and $+1$, depending on the number of times the k-means algorithm would assign the participant to either of the groups. A positive number denoted the affected group, negative numbers denoted the unaffected group. A number close to -1 would indicate a greater probability for the participant belonging to his or her assigned group. A number closer to zero should not be interpreted as evidence that the corresponding individual is necessarily closer to the opposite group.

Data labels, i.e. structural image scorings, were available from the local site, comprising 52 participants. These data were divided in balanced training and test sets and fitted to the random forest machine learning algorithm in Scikit-learn [38]. 75% (parameters from 39 participants) were used for training and 25% (parameters from 13 participants) were used for testing.

2.7. Statistics

The three levels of motion correction were compared by applying a least square fit (χ^2) between the measured data and the applied pharmacokinetic model (GCTT). Later analysis showed that the model curves do provide similar fits to the raw data. Moreover, since the GCTT model has an extra parameter, it would be more likely to overfit the data, and thus minimize the least square fit, making this a conservative approach. Three successive levels of motion correction (non-registered, affine and elastic) were compared based on a one-way ANOVA test. Tukey's post

Table 2

Sum of squares, χ^2 , between the relative enhancement curves and the fitted GCTT model after different applied motion corrections (non-registered, affine and elastic) across 47 participants. Percentages in round brackets refer to the percental improvement relative to non-registered data.

Registration Method	Left TMJ	Right TMJ
	Sum of Squares	Sum of Squares
Not registered (n = 47)	2.18	3.74
Affine (n = 47)	0.95 (56%)	0.90 (76%)
Elastic (n = 47)	0.60 (72%)	0.60 (84%)

Table 3

Effects of motion correction on DCE-MRI relative parameter differences. Means, standard deviations and *p*-values comparing the relative parameter difference, P_{rel} , distributions (Blood plasma flow F_p , Extraction fraction E , EES volume ve , Capillary transit time T_c , GCTT transit time distribution width α^{-1} and Bolus arrival time BAT) obtained with different motion correction methods (Non-registration, Affine and Elastic) in the 47 participants in which it was possible to estimate GCTT parameters without prior motion correction. The *p*-values are computed using the ANOVA test with three independent variables; no motion correction, affine motion correction and elastic Significance threshold $p < 0.05$.

Parameter (unit)	No motion correction		Affine motion correction		Elastic motion correction		<i>p</i> -value
	Mean	Std. dev.	Mean	Std. dev.	Mean	Std. dev.	
F_p	0.16	0.1	0.17	0.1	0.14	0.1	0.56
E	0.18	0.2	0.22	0.2	0.24	0.2	0.47
ve	0.62	0.4	0.62	0.4	0.61	0.4	0.98
T_c	0.28	0.3	0.27	0.2	0.23	0.2	0.51
α^{-1}	0.61	0.3	0.51	0.4	0.56	0.3	0.40
BAT	0.05	0.1	0.03	0.02	0.02	0.2	0.31

hoc test was applied to check for pairwise statistically differing means. The semi-quantitative parameter distributions of the GCTT model were visualized in boxplots with decreasing temporal resolutions, and with the different levels of motion correction applied. Semi-quantitative relative parameter difference (P_{rel}) distributions with low temporal resolutions (8 s, 12 s, 16 s and 20 s) were compared to the high temporal resolution (4 s) parameter distribution, using a paired sample *t*-test. *p*-values describing the levels of significance between the k-means clustered groups were computed based on a two-way ANOVA test with Tukeys post hoc test.

A significance threshold of $p = 0.05$ was selected in all statistical tests described above, meaning that any *p*-value lower than 0.05 indicates that the compared parameter distributions are statistically distinguishable.

3. Results

3.1. Effects of motion correction

Motion corrected relative enhancement curves from a randomly selected participant were overlaid by the GCTT model curves, Fig. 2, suggesting that elastic registration outperforms non-registration and affine registration. Without motion correction, the GCTT model failed to estimate parameters in 26 participants. The elastic registration scheme outperforms the affine registration, Table 2. The GCTT model was applied to the left and right TMJ from the remaining 47 participants. Measuring the sum-of-squares, χ^2 , between the measured motion corrected data in each TMJ and the corresponding modelled curve for each level of motion correction (no motion correction, affine registration and elastic registration), a better fit to higher-level motion corrected data is observed, Table 3.

Estimated GCTT relative perfusion parameter differences (P_{rel}) do not display mean values that differ significantly, Fig. 3, nor are the

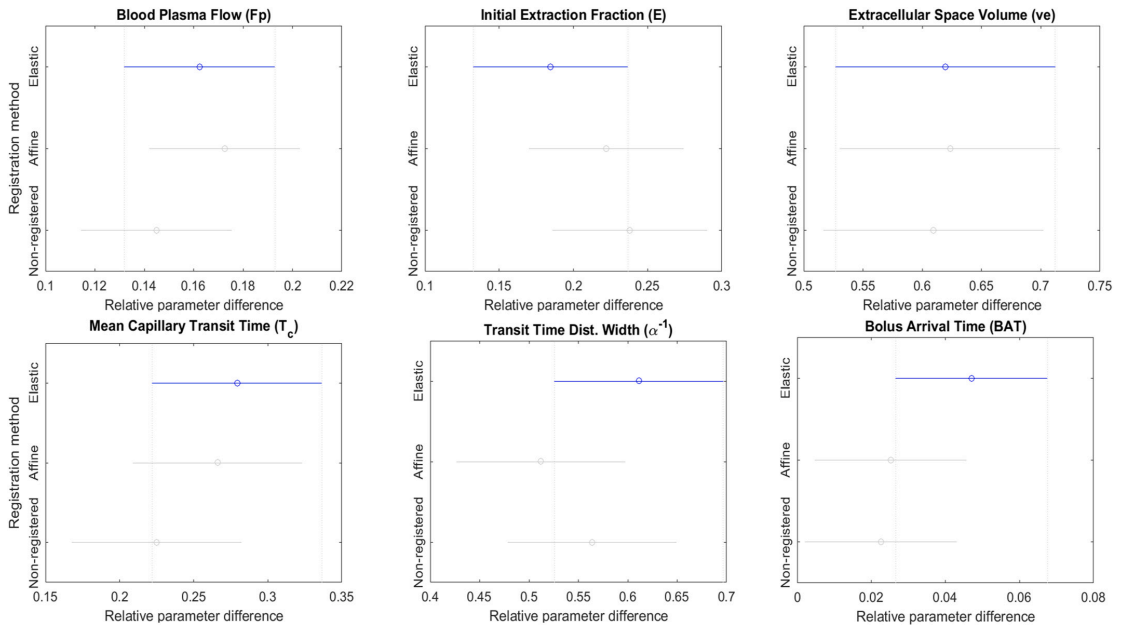


Fig. 3. Comparison of mean parameter values, P_{rel} (Blood plasma flow F_p , Extraction fraction E , EES volume ve , Capillary transit time T_c , GCTT transit time distribution width α^{-1} and Bolus arrival time BAT) between the left and right TMJ obtained with different motion correction methods (Non-registration, Affine and Elastic) in 47 participants.

Table 4
Effects of sampling rate in DCE-MRI. Statistical differences in relative parameter difference distributions in the Temporomandibular Joint in 73 participants across sampling rates and degree of motion correction. Significance threshold $p < 0.05$.

Parameter	Registration scheme	8 s	12 s	16 s	20 s
Rise Time, <i>RT</i>	Not registered	0.01	<	<	<
	Affine	0.01	<	0.005	0.005
	Elastic	<	0.005	0.005	0.005
Max, <i>M</i>	Not registered	0.90	0.42	<	<
	Affine	0.72	0.97	<	<
	Elastic	0.03	0.01	<	< 0.05
Slope, <i>S</i>	Not registered	0.83	0.48	0.26	0.24
	Affine	0.03	0.23	0.06	<
Area, <i>A</i>	Elastic	0.01	0.01	0.04	0.05
	Not registered	0.62	0.70	<	<
	Affine	0.48	0.29	<	<
	Elastic	0.02	0.07	<	<
				0.005	0.005

The significance threshold was set to $p=0.05$, and hence all values in table 4 below this threshold were rendered in bold. Bold font was chosen for easy reading of the table, drawing the attention to the pattern of the data.

ANOVA p -values comparing the various motion corrected schemes significant, Table 3. Means, standard deviations and p -values comparing the relative parameter difference, P_{rel} , distributions obtained with different motion correction methods (Non-registration, Affine and Elastic) in the 47 participants in which it was possible to estimate GCTT parameters without prior motion correction were calculated, Table 4. With increasing the level of motion correction, the p -values comparing the semi-quantitative relative parameter differences (P_{rel}) in the lower resolution data to the high (4 s) resolution data tend to decrease but are not statistically significant.

3.2. Effects of sampling rate

Reducing sampling rate reduces the variability in the estimated semi-quantitative relative parameter differences, P_{rel} , Fig. 4. When successively comparing P_{rel} of high temporal resolution (4 s), with lower temporal resolution (8 s, 12 s, 16 s and 20 s), Table 4, the distributions P_{rel} also change significantly with sufficiently decreased sample rates. With elastic motion correction this happens when the temporal resolution drops from 4 s to 8 s and suggests that it is important to have a sampling rate of 4 s.

3.3. Data-driven stratification of participants

The four pharmacokinetic models are all suited to fit the DCE-MRI data, and differ little in performance, Fig. 5. The relative standard-deviation of the sum of squares of residuals between the elastic registered raw data curve and the model curves is 3.4%.

A k-means algorithm was applied to categorize the participants into two groups, group A and group B. This was to investigate if the models categorize the participants very differently, based on the relative parameter differences. Based on a comparison to structural image scorings, group A was assumed to correspond to unaffected individuals, and group B was assumed to correspond to affected participants. Out of the 73 participants, 62 individuals were placed in group A, and 11 individuals were placed in group B, when analysing the data with the

GCTT model. Using the DCATH model instead, 59 individuals were placed in group A, and 14 were placed in group B. With the AATH model 66 individuals were placed in group A, and 7 individuals were placed in group B. Finally, with the 2CXM model, 63 individuals were placed in group A and 10 individuals were placed in group B.

Scorings, giving an indication of whether or not a participant was affected by JIA, based on structural MRI images were available for 52 of the 73 participants. Sensitivities and specificities were calculated assuming structural MRI data as the ground truth, using both unsupervised k-means stratification on all of the labelled data, as well as random forest classification on the balanced 25% of data used for testing of the random forest stratification, Table 5.

Across the pharmacokinetic models there was agreement about 52 participants; 51 of which were placed in group A, and one of which was placed in group B. Structural image scorings were available for 40 of the 52 participants between which there was agreement about group assignments across all pharmacokinetic models. Sensitivity of scores across models relative to the structural image scores was found to be 0, and the specificity 0.96. There clearly is an overlap between relative parameter differences (P_{rel}) in affected and unaffected participants Fig. 6, where the parameters are calculated with the DCATH model and there is agreement between the k-means clustered groupings and the structural image scores in 41 cases. Based on a two-way ANOVA test (significance threshold <0.05) with the standardized relative parameters and group scorings as independent variables and Tukey’s post hoc test, that neither the parameters, nor the interaction of parameters with group scorings were significant. However, group scorings were found to be significant ($p = 1.0 \cdot 10^{-6}$).

4. Discussion

There is need for more accurate diagnostic tests for JIA in general, since reported disease prevalence varies between 0.07 and 4.01 per 1000 children [2]. More specifically, reported TMJ involvement in confirmed cases of JIA covers a range from 45% to 87%, and this is largely due to differing diagnostic methodology and asymptomatic TMJ [2], [5–13]. In the current study DCE-MRI is explored as a potential tool to aid in the diagnosis.

We have examined the methodology in application of DCE-MRI as a possible diagnostic tool and found that a better fit to the GCTT model is obtained with high-level elastic motion correction. We recommend a sampling rate of at least 4 s to capture potentially disease relevant signal variations after application of high-level motion correction. The various parametric models all leave comparable and small residues. Since none of the applied perfusion models left a substantial residue and since they display comparable sensitivities and specificities relative to the structural image scores, in principle, all the models are potentially applicable to the TMJ. It remains to be tested whether one of the models outperforms the others in the diagnostics of JIA affected TMJ, and since the diagnostic criteria are still hampered by differing diagnostic methodologies, the model estimations must be evaluated in the light of more clinical data.

High-level motion correction, specifically elastic image registration, provides smoother relative enhancement curves and a better fit to the GCTT model approximation. The model approximation also becomes smoother with increasing levels of motion correction of the raw data. The statistical comparison between mean values of parameter distributions does not suggest that the post registration parameter distributions differ significantly from pre-registration parameter distributions. A large proportion of data stemming from minimally moving participants could be a reason for this. Even though estimated parameter values do not change on a population level, individual parameters might still be estimated more accurately when motion correction is applied.

Even without application of motion correction, the results of this study indicate that if the sampling rate is lower than 4 s, it is possible that important information about the dynamics in the TMJ is lost. The

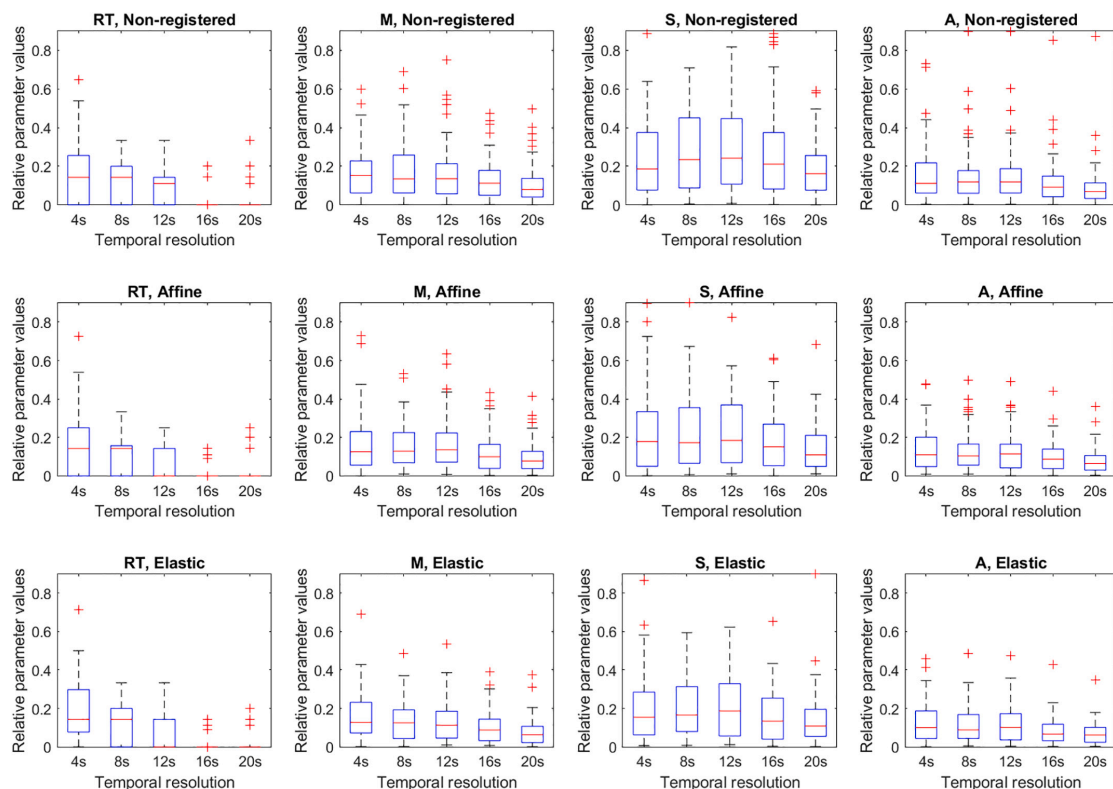


Fig. 4. Effects of sampling rates in DCE-MRI. Distributions of relative differences, P_{rel} , in semi-quantitative parameters (Rise time - RT, First maximum value - M, Slope of curve tail - S and Area under curve - A) between the left and right temporomandibular joints with decreasing temporal resolution after motion correction (top; non-registration, middle; affine registration, bottom; elastic registration) in 73 participants.

parameter distributions with diminishing temporal resolution become more dissimilar with a higher level of motion correction. This could also suggest the importance of high sampling rates to avoid loss of potentially valuable diagnostic information.

There is substantial overlap within detectable differences in parameter estimations between the left and right TMJ in presumed affected versus unaffected participants. However, DCE-MRI may be a feasible diagnostic tool in the evaluation of JIA affected TMJ, as a specific, rather than a sensitive tool. The current study focuses on the methodological aspects of DCE-MRI data processing, to ensure that the data can be evaluated in JIA diagnostics. Since no consensus yet exists in the evaluation of JIA affected TMJ, to further assess DCE-MRI data for this application, DCE-MRI data should be compared to other clinical data in a larger study cohort.

A limitation of this study is the use of a population-based AIF, as opposed to patient specific AIFs, since patient specific AIFs might be better suited for the description of individual biology. However, measuring individual AIFs would be user dependent, adding another level of variability to the data. A recent study did not find that patient specific AIFs improved the repeatability in the head and neck area [39]. Furthermore, we have been comparing relative perfusion parameter differences between the left and right TMJ. We have therefore assumed that inaccuracies that are not disease relevant, caused by the AIF are cancelled out. While it is unlikely that both TMJs are equally affected [26], one should keep in mind that the possibility that they are, though small, is still present. Our approach is conservative, in that if both TMJs

should indeed be equally affected it would not contribute towards a positive conclusion about the DCE-MRI feasibility as a diagnostic tool for JIA. We have aimed to highlight the disease relevant information contained in the measurements, given that we do not know whether absolute parameter measurements can be directly compared between children.

In conclusion, we have found that any of the pharmacokinetic models investigated can be used to model the TMJ vascularity. A temporal resolution of at least 4 s should be used in the measurement of the DCE-MRI data. A high temporal resolution in DCE-MRI data from the TMJ holds information which is not available in corresponding lower sampled data. Elastic image registration allows motion affected data to be sufficiently recovered to be included for pharmacokinetic modelling. Motion correction thus facilitates the data analysis for evaluation of DCE-MRI as a diagnostic tool for JIA affected TMJ. To further assess the diagnostic value of high temporal resolution DCE-MRI data, as well as of motion corrected DCE-MRI data, the estimated perfusion parameters should be correlated to other clinical information in a larger study cohort.

Funding

This work was supported by the Trond Mohn Foundation [grant numbers BFS2016TMT01]; the European Regional Development Fund-Project "Modernization and support of research activities of the national infrastructure for biological and medical imaging Czech-Biolmaging"

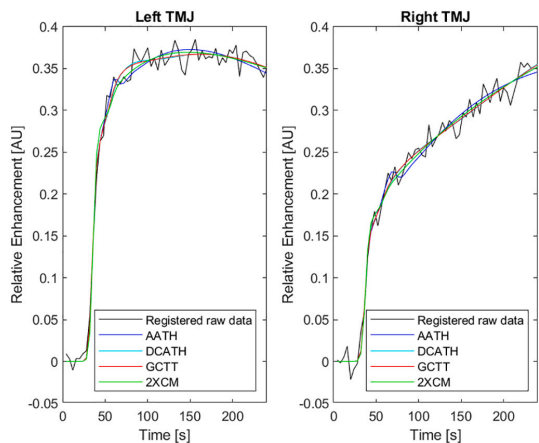


Fig. 5. A comparison of four pharmacokinetic models (Blue: Adiabatic Approximation to the Tissue Homogeneity Model (AATH), Cyan: Distributed Capillary Adiabatic Tissue Homogeneity Model (DCATH), Red: Gamma Capillary Transit Time Model (GCTT) and Green: Two Compartment Exchange Model (2XCM)) applied in a random participant. Left Temporomandibular Joint (TMJ) (left column), right TMJ (right column). Elastic motion corrected relative enhancement curves (black) are overlaid parametric model curves. (For interpretation of the references to colour in this figure legend, the reader is referred to the web version of this article.)

Table 5

Sensitivities and specificities of k-means clusters after principal component analysis. Principal component analysis was performed including all parameters defined in Table 1. The quantitative model parameters were estimated with the Adiabatic Approximation to Tissue Homogeneity (AATH) model, Distributed Capillary Adiabatic Tissue Homogeneity (DCATH) model, Gamma Capillary Transit Time (GCTT) model as well as the Two-Compartment Exchange Model (2XCM). Numbers in parentheses refer to the sensitivity and specificity of random forest machine learning predictions on the 25% of the data that was used for testing.

	AATH	DCATH	GCTT	2XCM
Sensitivity	0 (0)	0.27 (0)	0 (0)	0.18 (0)
Specificity	0.93 (0.85)	0.93 (0.85)	0.90 (0.83)	0.93 (0.85)

[grant numbers CZ.02.1.01/0.0/0.0/16_013/0001775]; the MEYS CR

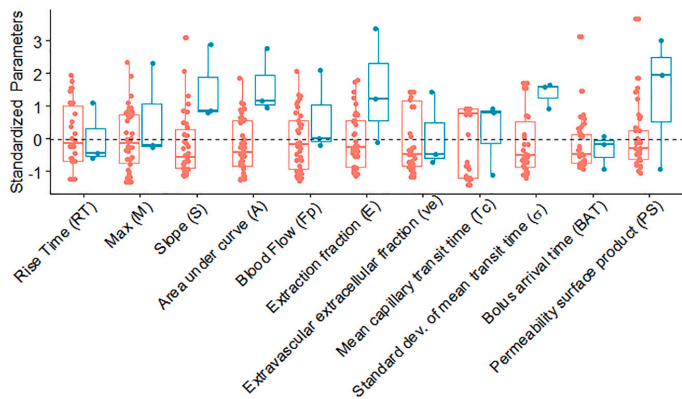


Fig. 6. Standardized relative parameter differences calculated using the Distributed Capillary Adiabatic Tissue Homogeneity (DCATH) model and semi-quantitative parameters in the assumed unaffected participants (Group A; red) and assumed affected participants (Group B; blue) in the 41 cases where there is agreement on diagnosis between the k-means clustering and structural image scores. (For interpretation of the references to colour in this figure legend, the reader is referred to the web version of this article.)

[grant numbers LO1212]; the Northern Norway Regional Health Authority [grant numbers; SPF1229-15]; and the Tromsø Research Foundation.

Declaration of Competing Interest

The authors have no financial interests to declare.

References

- [1] Petty RE, Southwood TR, Manners P, Baum J, Glass DN, Goldenberg J, et al. International league of associations for rheumatology classification of juvenile idiopathic arthritis: second revision. *J Rheumatol* 2004;31:390–1.
- [2] Manners PJ, Bower C. Worldwide prevalence of juvenile arthritis - why does it vary so much? *J Rheumatol* 2002;29:1520–30.
- [3] Selvaag AM, Aulie HA, Lilleby V, Flato B. Disease progression into adulthood and predictors of long-term active disease in juvenile idiopathic arthritis. *Ann Rheum Dis* 2016;75:190–5.
- [4] Oliveira-Ramos F, Eusébio M, Martins FM, Mourão AF, Furtado C, Campanilho-Marques R, et al. Juvenile idiopathic arthritis in adulthood: fulfilment of classification criteria for adult rheumatic diseases, long-term outcomes and predictors of inactive disease, functional status and damage. *RMD Open* 2016;2. <https://doi.org/10.1136/rmdopen-2016-000304>.
- [5] Weiss PF, Arabshahi B, Johnson A, Blaniuk LT, Zarnow D, Cahill AM, et al. High prevalence of temporomandibular joint arthritis at disease onset in children with juvenile idiopathic arthritis, as detected by magnetic resonance imaging but not by ultrasound. *Arthritis Rheumatol* 2008;58:1189–96.
- [6] Niibo P, Pruunsild C, Voog-Oras U, Nikopensius T, Jagomägi T, Saag M. Contemporary management of TMJ involvement in JIA patients and its orofacial consequences. *EPMA J* 2016;7. <https://doi.org/10.1186/s13167-016-0061-7>.
- [7] Twilt M, Mober SMLM, Arends LR, ten Cate R, van Suijlekom-Smit L. Temporomandibular involvement in juvenile idiopathic arthritis. *J Rheumatol* 2004;31:1418–22.
- [8] Küselér A, Pedersen TK, Herlin T, Gelineck J. Contrast enhanced magnetic resonance imaging as a method to diagnose early inflammatory changes in the temporomandibular joint in children with juvenile chronic arthritis. *J Radiol* 1998;25:1406–12.
- [9] Hauser RA, Schroeder S, Cannizzaro E, Müller L, Kellenberger CJ, Saurenmann RK. How important is early magnetic resonance imaging of the temporomandibular joint for the treatment of children with juvenile idiopathic arthritis: a retrospective analysis. *Pediatric Rheumatol* 2014;12. <https://doi.org/10.1186/1546-0096-12-36>.
- [10] Karhullahti T, Ylijoki H, Rönning O. Mandibular condyle lesions related to age at onset and subtypes of juvenile rheumatoid arthritis in 15-year-old children. *Scand J Dent Res* 1993;101:332–8.
- [11] Müller L, Kellenberger CJ, Cannizzaro E, Ettlin D, Schraner T, Bolt IB, et al. Early diagnosis of temporomandibular joint involvement in juvenile idiopathic arthritis: a pilot study comparing clinical examination and ultrasound to magnetic resonance imaging. *Rheumatology* 2009;48:680–5.
- [12] Jank S, Haase S, Strobl H, Michels H, Häfner R, Missmann N, et al. Sonographic investigation of the temporomandibular joint in patients with juvenile idiopathic arthritis: a pilot study. *Arthritis Rheum* 2007;57:213–8.
- [13] Ronchezel MV, Hilarío MO, Goldenberg J, Ledermann HM, Faltin KJ, Azevedo MF, et al. Temporomandibular joint and mandibular growth alterations in patients with juvenile rheumatoid arthritis. *J Rheumatol* 1995;22:1956–61.
- [14] Suenaga S, Hamamoto S, Kawano K, Higashida Y, Noikura T, Dynamic MR. Imaging of the temporomandibular joint in patients with arthrosis: relationship





- between contrast enhancement of the posterior disk attachment and joint pain. *AJR Am* 1996;166:1475–81.
- [15] Tasali N, Cubuk R, Aricak M, Ozazar M, Saydam B, Nur H, et al. Temporomandibular joint (TMJ) pain revisited with dynamic contrast-enhanced magnetic resonance imaging (DCE-MRI). *Eur J Radiol* 2011;81:603–8.
- [16] Xiong X, Ye Z, Tang H, Wei Y, Nie L, Wei X, et al. MRI of temporomandibular joint disorders: recent advances and future directions. *J Magn Reson Imaging* 2020;0. <https://doi.org/10.1002/jmri.27338>.
- [17] Sano T, Westesson P-L. Magnetic resonance imaging of the temporomandibular joint: increased T2 signal in the retrodiskal tissue of painful joints. *Oral Surg Oral Med Oral Pathol Oral Radiol Endod* 1995;79:511–6.
- [18] Rosen BR, Belliveau JW, Vevea JM, Brady TJ. Perfusion imaging with NMR contrast agents. *Magn Reson Med* 1990;14:249–65.
- [19] Chen W, Giger ML, Bick U, Newstead GM. Automatic identification and classification of characteristic kinetic curves of breast lesions on DCE-MRI. *Med Phys* 2006;33:2878–87.
- [20] Schabel MC. A unified impulse response model for DCE-MRI. *Magn Reson Med* 2012;68:1632–46.
- [21] Sourbron SP, Buckley DL. Tracer kinetic modelling in MRI: estimating perfusion and capillary permeability. *Phys Med Biol* 2011;57:R1–33.
- [22] Sourbron SP, Buckley DL. Classic models for dynamic contrast-enhanced MRI. *NMR Biomed* 2013;26:1004–27.
- [23] Starck LS, Andersen E, Macféeek O, Jirík R, Angenete O, Augdal T, et al. Effects of image registration in dynamic contrast enhanced MRI of the TMJ. In: Proceedings of the 27th Annual Meeting of ISMRM, Montréal; 2019 (abstract 4490).
- [24] Parker GJ, Roberts C, Macdonald A, Buonaccorsi GA, Cheung S, Buckley DL, et al. Experimentally-derived functional form for a population-averaged high-temporal-resolution arterial input function for dynamic contrast-enhanced MRI. *Magn Reson Med* 2006;56:993–1000.
- [25] Macféeek O, Jirík R, Mikulka J, Bartoš M, Šprláková-Puková A, Kerkovský M, et al. Time-efficient perfusion imaging using DCE- and DSC-MRI. *Measure Sci Rev* 2018; 18:262–71.
- [26] Demant S, Hermann NV, Darvann TA, Zak M, Schatz H, Larsen P, et al. 3D analysis of facial asymmetry in subjects with juvenile idiopathic arthritis. *Rheumatology* 2011;50:586–92.
- [27] St. Lawrence KS, Lee T-Y. An adiabatic approximation to the tissue homogeneity model for water exchange in the brain: I. theoretical derivation. *J Cereb Blood Flow Metab* 1998;18:1365–77.
- [28] St. Lawrence KS, Lee T-Y. An adiabatic approximation to the tissue homogeneity model for water exchange in the brain: II. Experimental validation. *J Cereb Blood Flow Metab* 1998;18:1378–85.
- [29] Bartoš M, Jirík R, Kratochvíla J, Standara M, Starčuk Z, Taxt T. The precision of DCE-MRI using the tissue homogeneity model with continuous formulation of the perfusion parameters. *Magn Reson Imaging* 2014;32:505–13.
- [30] Koh TS, Zeman V, Darko J, Lee T-Y, Milosevic MF, Haide M, et al. The inclusion of capillary distribution in the adiabatic tissue homogeneity model of blood flow. *Phys Med Biol* 2001;46:1519–838.
- [31] Klein S, Staring M, Murphy K, Viergever MA, JPW Pluim. Elastix: a toolbox for intensity based medical image registration. *IEEE Trans Med Imaging* 2010;29: 196–205.
- [32] Shamonin DP, Bron EE, Lelieveldt BPF, Klein MSS, Staring M. Fast parallel image registration on CPU and GPU for diagnostic classification of Alzheimer's disease. *Front Neuroinform* 2014;7:1–15.
- [33] Van't Klooster R, Staring M, Klein S. Automated registration of multispectral MR vessel wall images of the carotid artery. *Med Phys* 2014;40. <https://doi.org/10.1118/1.4829503>.
- [34] van't Klooster R. Open Source Image Registration Parameter File. 2020. "http://elastix.bigr.nl/wiki/index.php/Parameter_file_database," 3 March 2020. [Online]. Available: http://elastix.bigr.nl/wiki/images/8/89/Par0018_3D_affine_ML.txt. [Accessed 2020 May 21].
- [35] Maes F, Collignon A, Vandermeulen D, Marchal G, Suetens P. Multimodality image registration by maximization of mutual information. *IEEE Trans Med Imaging* 2006;16:187–98.
- [36] Klein S, Pluim JPW, Staring M, Viergever MA. Adaptive stochastic gradient descent optimisation for image registration. *Int J Comput Vis* 2009;81:227–39.
- [37] Hodneland E, Lundervold A, Rørvik J, Munthe-Kaas AZ. Normalized gradient fields for nonlinear motion correction of DCE-MRI time series. *Comput Med Imaging Graph* 2014;38:202–10.
- [38] Pedregosa F, Varoquaux G, Gramfort A, Michel V, Thirion B, Grisel O, et al. Machine learning with python. *J Mach Learn Res* 2011;12(85):2825–30.
- [39] Koopman T, Martens RM, Lavini C, Yaqub M, Castelijns JA, Boellaard R, et al. Repeatability of arterial input functions and kinetic parameters in muscle obtained by dynamic contrast enhanced MR imaging of the head and neck. *Magn Reson Imaging* 2020;68:1–8.

Appendix D: Paper 4

Effects of Multi-Shell Free Water Correction on Glioma Characterization

Article

Effects of Multi-Shell Free Water Correction on Glioma Characterization

Lea Starck^{1,2,*}, Fulvio Zaccagna^{3,4}, Ofer Pasternak^{5,6}, Ferdia A. Gallagher^{7,8}, Renate Grüner^{1,2} and Frank Riemer²

- ¹ Department of Physics and Technology, University of Bergen, N-5007 Bergen, Norway; rena.te.gruener@uib.no
 - ² Mohn Medical Imaging and Visualization Centre (MMIV), Department of Radiology, Haukeland University Hospital, University of Bergen, N-5021 Bergen, Norway; frank.riemer@helse-bergen.no
 - ³ Department of Biomedical and Neuromotor Sciences, University of Bologna, 40125 Bologna, Italy; f.zaccagna@gmail.com
 - ⁴ IRCCS Istituto delle Scienze Neurologiche di Bologna, Functional and Molecular Neuroimaging Unit, Bellaria Hospital, 40139 Bologna, Italy
 - ⁵ Department of Psychiatry, Brigham and Women's Hospital, Harvard Medical School, Boston, MA 02215, USA; ofer@bwh.harvard.edu
 - ⁶ Department of Radiology, Brigham and Women's Hospital, Harvard Medical School, Boston, MA 02215, USA
 - ⁷ Department of Radiology, University of Cambridge, Cambridge CB2 0QQ, UK; fag1000@cam.ac.uk
 - ⁸ Cancer Research UK Cambridge Institute, University of Cambridge, Cambridge CB2 0RE, UK
- * Correspondence: lea.starck@uib.no



check for updates

Citation: Starck, L.; Zaccagna, F.; Pasternak, O.; Gallagher, F.A.; Grüner, R.; Riemer, F. Effects of Multi-Shell Free Water Correction on Glioma Characterization. *Diagnostics* **2021**, *11*, 2385. <https://doi.org/10.3390/diagnostics11122385>

Academic Editor:
Panagiotis Papanagiotou

Received: 18 November 2021
Accepted: 13 December 2021
Published: 17 December 2021

Publisher's Note: MDPI stays neutral with regard to jurisdictional claims in published maps and institutional affiliations.



Copyright: © 2021 by the authors. Licensee MDPI, Basel, Switzerland. This article is an open access article distributed under the terms and conditions of the Creative Commons Attribution (CC BY) license (<https://creativecommons.org/licenses/by/4.0/>).

Abstract: Diffusion MRI is a useful tool to investigate the microstructure of brain tumors. However, the presence of fast diffusing isotropic signals originating from non-restricted edematous fluids, within and surrounding tumors, may obscure estimation of the underlying tissue characteristics, complicating the radiological interpretation and quantitative evaluation of diffusion MRI. A multi-shell regularized free water (FW) elimination model was therefore applied to separate free water from tissue-related diffusion components from the diffusion MRI of 26 treatment-naïve glioma patients. We then investigated the diagnostic value of the derived measures of FW maps as well as FW-corrected tensor-derived maps of fractional anisotropy (FA). Presumed necrotic tumor regions display greater mean and variance of FW content than other parts of the tumor. On average, the area under the receiver operating characteristic (ROC) for the classification of necrotic and enhancing tumor volumes increased by 5% in corrected data compared to non-corrected data. FW elimination shifts the FA distribution in non-enhancing tumor parts toward higher values and significantly increases its entropy ($p \leq 0.003$), whereas skewness is decreased ($p \leq 0.004$). Kurtosis is significantly decreased ($p < 0.001$) in high-grade tumors. In conclusion, eliminating FW contributions improved quantitative estimations of FA, which helps to disentangle the cancer heterogeneity.

Keywords: glioma; free water; tumor characterization

1. Introduction

Glial tumors are the most frequent malignant primary brain tumors, with incidence rates of 5.4/100,000 in Europe and 7.1/100,000 in the United States [1–3]. Gliomas are highly heterogeneous and infiltrative, limiting a complete surgical removal and successful treatment. Overall, the proportion of patients that fully recover is approximately 7.9% [3]. Gliomas can occur at any age, but when comparing to individuals under 20 years, gliomas are approximately 1.5 times more common in those aged over 20 years [4] and more than 10 times more common in those aged over 60 years [3]. Magnetic resonance imaging (MRI) retains a key role for diagnosis, treatment planning, and response monitoring of gliomas using both conventional and more advanced imaging techniques [5–7]. Based on morphological proton imaging, the tumor is commonly subdivided into different sub-regions: solid tumor, enhancing, non-enhancing, or peritumoral areas [8–11].

Diffusion tensor imaging (DTI) is an advanced technique that can estimate fractional anisotropy (FA) and mean diffusivity (MD), describing properties of the underlying tissue microstructure. There is still no consensus on the optimal methodology for processing DTI data; consequently, their ability to characterize gliomas, particularly regarding tumor grade, is still a matter of debate [8–10,12]. The most reported metrics are mean estimates of MD and FA, although statistical measures other than the mean could be of interest [10,11]. Based on eigenvalues and eigenvectors of the estimated diffusion tensor in each imaged voxel, tractography is often performed to create a three-dimensional visualization of fiber tracts [13,14].

High-grade gliomas typically spread outside the boundaries of the contrast enhancing lesion, within the surrounding peritumoral non-enhancing region of signal change. This spread may cause a reduction of FA, due to disrupted fiber tracts [15,16], but this is difficult to differentiate from the similar reduction of FA caused by vasogenic edema also abundant in the peritumoral region [17]. Vasogenic edema is mostly composed of free water (FW), and the fast diffusion of water molecules within edematous tissues will cause a more rapid diffusion signal decay than typically observed in tissues where water is more hindered or restricted. As a result, the DTI measures in edematous regions are biased by the FW contribution and reflect a mixture of edema and tissue.

One means of extracting the isotropic diffusion signal contribution from the edema is through advanced mathematical modelling [18–21]. A two-compartmental model accounting for free water contribution was first proposed by Pierpaoli and Jones [22]. The model assumes that the measured diffusion attenuation signal is the sum of attenuation in the two compartments and that these compartments have different diffusion tensors. In this study, an FW modelling approach proposed by Pasternak et al. [18] is applied in gliomas to improve tumor characterization. Since tumor heterogeneity is a hallmark of different biological and metabolic microenvironments, an *in vivo* assessment of heterogeneity may help, for instance, in determining treatment response, distinguishing true disease progression from pseudo-progression [23–25]. Necrosis is the result of a reduction in cell density [26,27], and increased FW content could provide a basis for a more detailed characterization of the expansion of necrosis. Improving the characterization of gliomas may also improve non-invasive tumor grading, as well as allow more accurate treatment planning. For example, several studies have reported increased fiber tracking capabilities after FW correction [28–32], indicating that FW correction may improve treatment planning.

To understand the impact of the advanced modelling in gliomas, diffusion tensor data are analyzed in the current study both with and without the free water elimination. Receiver operator characteristic (ROC) curves are estimated to investigate the classification of tumor sub-regions in high-grade tumors. Furthermore, potential differences between corrected and non-corrected FA estimations are evaluated in low- and high-grade tumors.

2. Materials and Methods

2.1. Data Collection

Twenty-six treatment-naïve glioma patients (11 males, 15 females; 52 ± 18 years, range 21–78 years), part of a cohort previously recruited for prospective, ethically approved studies, were included in this retrospective study. Patient characteristics are summarized in Table 1. MRI was carried out as part of routine surgical planning at Addenbrooke's Hospital, Cambridge University NHS Foundation Trust. Subjects included in this study matched the following criteria: glioma confirmed on histology, presence of structural MR imaging, multiple b-value diffusion imaging, and binarized masks of tumor volume. Written and informed consent was obtained from all participants and the study was approved by the NRES Committee East of England, Cambridge 2 ethics committee.

Table 1. Number of patients, mean total tumor volume, mean age, and sex across tumor grades. Note that edema was included in total volume, and the single grade I patient did not have much edema.

	Grade I	Grade II	Grade III	Grade IV
Number of patients	1 (1 F *)	8 (7 F, 1 M **)	2 (1 F, 1 M)	15 (6 F, 9 M)
Mean age	22 years	35 ± 11 years	46 ± 11 years	65 ± 10 years
Mean total tumor volume	6.0 cc ***	57.6 ± 76.5 cc	48.0 ± 12.5 cc	46.7 ± 27.2 cc

* F = female, ** M = male, *** cc = cubic centimeters.

Data were collected on a 3 T MRI system (Discovery MR750, GE Healthcare, Waukesha, WI, USA) using a 12-channel head coil. Structural T_1 -weighted (T_1w) images (256×256 matrix size, slice thickness 1.5 mm, FOV 240 mm \times 240 mm) were acquired using an inversion-prepared fast 3D spoiled gradient echo sequence ($TR/TE/TI/FA = 8.2$ ms/ 3.2 ms/ 450 ms/ 12°). T_2 -weighted (T_2w) images (320×320 matrix size, slice thickness 1.2 mm, FOV 240 mm \times 240 mm) were acquired using a 3D spin echo sequence ($TR/TE = 2500$ ms/ 79 ms).

Multi-shell DWI were acquired as follows with a pulsed-gradient spin-echo echo-planar imaging (EPI) sequence: b-values 0, 90, 150, 500, and 1000 s/mm²; 256×256 matrix size; slice thickness 2 mm; FOV 220 mm \times 220 mm; $TR/TE = 2000$ ms/ 80 ms. Diffusion acquisitions were performed in 8 directions in each shell. Low b-value shells were selected because, with a diffusivity of 3.00×10^{-3} mm²/s, FW is fast-diffusing compared to normal brain tissue, which has a diffusivity of approximately 0.8×10^{-3} mm²/s. Hence, lower b-values are better suited to estimate FW than higher b-values.

Based on the T_1w - and T_2w -images, a neuroradiologist with 8 years of experience manually outlined regions of interest (ROIs) encompassing the entire lesion, including the peritumoral region (total tumor volume), the enhancing lesion (enhancing tumor region), and the non-enhancing, presumed necrotic core (necrotic tumor region) (Figure 1). ROIs for the non-enhancing tissue (non-enhancing tumor region) were calculated by subtracting the enhancing tumor region and necrotic tumor region from the total tumor region. The tumor grades were confirmed by histology according to the 2016 WHO criteria [33,34].

2.2. Data Modelling

Each voxel is modelled as a weighted sum of two compartments, one compartment composed of free water (FW compartment), the other containing water in the vicinity of tissue structures that hinder or restrict water diffusion (tissue compartment). The diffusivity of the FW compartment is isotropic and fixed to 3.00×10^{-3} mm²/s, which is the diffusivity of FW at body temperature [35]. The data are modelled using a regularized fit [18], implementing a Euclidean tensor metric [36], and initialized with tensors with MD of 0.6×10^{-3} mm²/s. The fractional volume of the FW compartment, f , and the diffusion tensor modelling the tissue compartment are estimated. FW maps provide the voxel-wise f value, and the tissue compartment tensor is decomposed to eigenvalues to calculate free water corrected FA.

2.3. Data Processing and Parameter Extraction

Motion correction was performed using the FSL toolbox (version 6.0.1, University of Oxford, Oxford, UK) [37]. Skull stripping was performed prior to fitting of parameters [38].

Both regular tensor fits and free water corrected multi-shell tensor fits were computed from the data. Regular tensor fitting was applied to a single shell with b-value 1000 s/mm² using FSL [37]. Free-water-corrected tensor fitting was applied to the multi-shell diffusion data (b-values 90, 150, 500, and 1000 s/mm²). B0 images were registered to the T_1w images using a normalized mutual information cost function and a 4th degree b-spline interpolation in SPM12 (version 7771, University College London, London, UK) [39]. The transformation was then applied to all calculated maps, including the FW maps, FW-corrected FA (FA_t), and non-corrected FA (FA) maps. Measurements were extracted from the total tumor region and non-enhancing regions using (1) FA maps derived with regular

tensor fitting, (2) *FA* maps derived with free water corrected tensor fitting, and (3) *FW* maps derived with free-water-corrected tensor fitting. Map-derived ROI summary variables including mean and variance, 25th and 75th quantile, median, skewness, kurtosis, and entropy of the *FA* and *FW* map were computed.

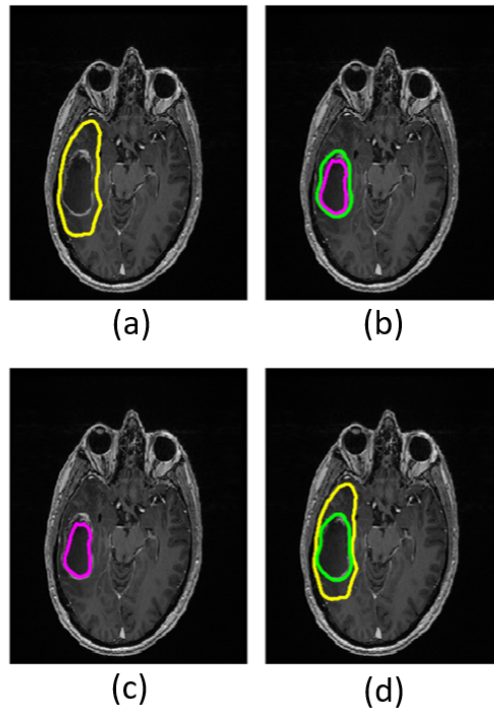


Figure 1. Masks in a grade IV patient overlaid on structural T_1w images. The yellow boundary shows the total tumor region (a); the area between the green and purple boundaries shows the enhancing tumor region (b); the area within the purple boundary shows necrotic tumor region (c); and the area between the yellow and green boundaries shows the non-enhancing tumor region (d).

FW correction failed in one out of the 15 grade IV patients, due to corrupted DICOM images in the low *b*-value diffusion images.

2.4. Statistical Analysis

To test whether tumor volumes, i.e., necrotic and enhancing volumes, and enhancing and non-enhancing volumes can be separated based on parameter means within these volumes after *FW* correction, ANOVA testing with Tukey's post hoc test was performed. To test whether conventional mean *MD* that is not corrected for *FW* can differentiate between tumor regions, the same ANOVA test with Tukey's post hoc test was performed using non-corrected data. Receiver operator characteristic (ROC) curves were computed by fitting a logistic regression model to labelled image voxels to evaluate the ability of *FW*-corrected data to classify voxels to their assigned tumor volume.

The effect of *FW* correction on the various tumor volumes (enhancing, necrotic, non-enhancing, and total tumor volumes) were investigated using a paired *t*-test.

To assess group differences, the patient cohort was separated into low-grade (grades I and II) and high-grade (grades III and IV) tumors, and differences were investigated using paired *t*-tests.

Results were deemed statistically significant for $p < 0.05$, and p -values were computed with t -tests adjusted for multiple comparisons using the Bonferroni method.

3. Results

3.1. Characterizing Tumor Sub-Regions

There is a larger variance in the distribution of the mean FW in the necrotic tumor region than in other parts of the tumor (Figure 2), and the mean FW is significantly higher in the necrotic region ($FW_{mean} = 0.50$) than in both the enhancing ($FW_{mean} = 0.30$) and non-enhancing ($FW_{mean} = 0.30$) regions in grade IV patients ($p \leq 0.015$), as well as in the total tumor volume region across all patients ($FW_{mean} = 0.33$). Mean FA_t is significantly lower ($p \leq 0.001$) in the necrotic tumor region ($FA_{t,mean} = 0.13$) than in the other defined tumor regions ($FW_{mean} \leq 0.27$). Measurements of FA and FW from the enhancing, non-enhancing, and total tumor regions do not differ statistically significantly from one another. Although there may be tendencies toward higher MD in the necrotic region compared to non-necrotic regions, conventional MD that is not corrected for FW does not significantly differentiate between tumor regions (Supplementary Material, Figure S1).

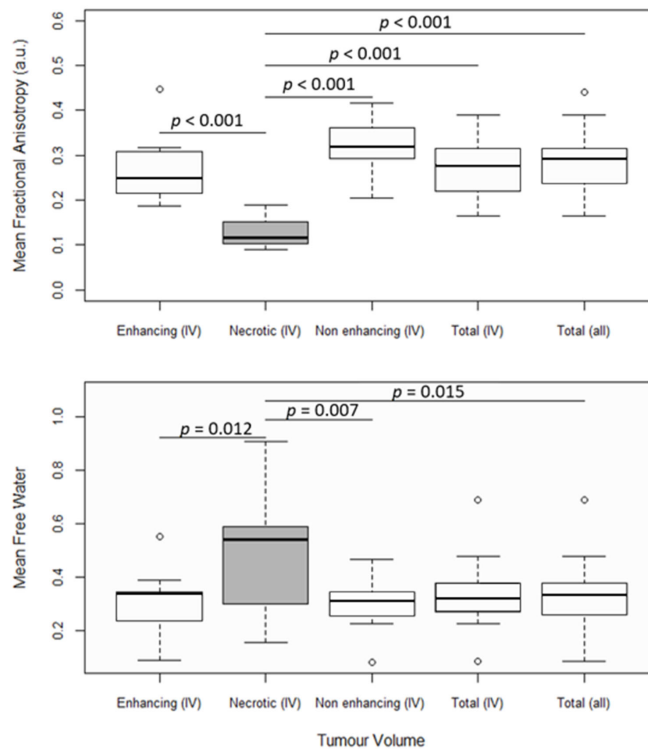


Figure 2. FW -corrected fractional anisotropy (FA_t) and mean free water (FW). The first four box and whisker plots from the left show the mean parameter values in enhancing tumor regions, necrotic tumor regions, non-enhancing tumor regions, and total tumor regions from grade IV patients. The fifth box and whisker plot shows the mean parameter values in total tumor regions from all patients. Significantly different distributions are marked with their corresponding p -values. Boxes with white backgrounds do not differ significantly from other boxes with white backgrounds. Statistics were performed with ANOVA tests and Tukey's post hoc test at a significance threshold of $p < 0.05$.

FW maps with cross-sections of total and necrotic tumor regions overlaid can be seen in Figure 3. The variance in mean FW, as mentioned above, may be visually suggested by the varying gray scale levels representing high and low FW content within the necrotic areas (green outline).

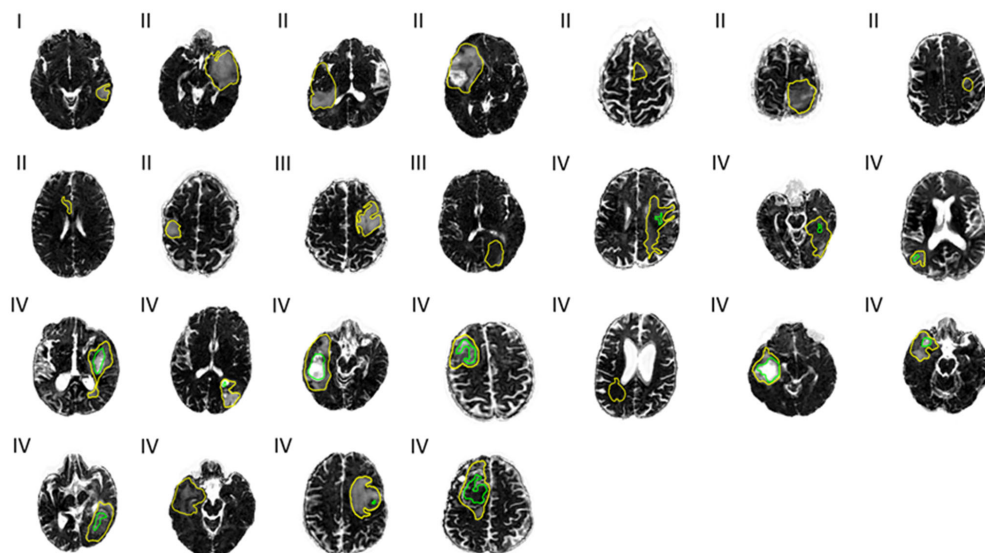


Figure 3. Free water (FW) maps across 25 patients. Tumor grades I, II, III, and IV are noted to the top left at each map. Outlines of the total tumor regions (yellow) and necrotic tumor regions (green) are overlaid.

The *FA* distribution in the necrotic tumor region is least affected by FW corrections, as there is no significant change in *FA* values, as measured by the mean, median, and quantiles (Table 2). In non-necrotic regions, these summary variables increase on average by 20.4%, and kurtosis decreases by 56.6%. Entropy increases by 6.7% in necrotic areas and on average by 7.5% in non-necrotic regions. Skewness decreases by 49.9% in necrotic areas and on average by 62.2% in non-necrotic regions.

Table 2. Significances of the effects of free water correction on fractional anisotropy (*FA*) summary variables across tumor regions (TR) in grade IV patients. *p*-values are calculated with a paired *t*-test and a significance threshold of *p* < 0.05. The *p*-values are adjusted for multiple comparisons using the Bonferroni method.

<i>p</i> -Values	Enhancing TR	Necrotic TR	Non-Enhancing TR	Total TR
Mean	0.013	1.0	<0.001	<0.001
Variance	0.11	1.0	1.0	1.0
25th Quantile	<0.001	0.27	<0.001	0.001
75th Quantile	0.005	0.068	<0.001	<0.001
Median	<0.001	0.22	<0.001	<0.001
Entropy	0.010	0.018	<0.001	<0.001
Kurtosis	<0.001	0.50	0.003	<0.001
Skewness	<0.001	0.018	<0.001	<0.001

ROC curves were calculated based on voxel-wise labelling of necrotic and enhancing tumor regions and a logistic regression model and show that necrotic tumor regions can be better differentiated using FW-corrected data than with regular *FA* maps. Results are shown from a single patient in Figure 4. In this patient, the average area under the curve (AUC)

is greater than average. Across all patients, the AUC was 0.77 based on *FA_t*, 0.73 with *FA*, and 0.77 with *FW*. Enhancing tumor regions were defined as the true positive and the adjacent necrotic tumor regions as the true negative. When enhancing tumor regions are separated from the adjacent non-enhancing tumor regions and non-enhancing tumor regions are labelled as the true positive, the AUCs are 0.66, 0.67, and 0.62 in *FA_t*, *FA*, and *FW*, respectively.

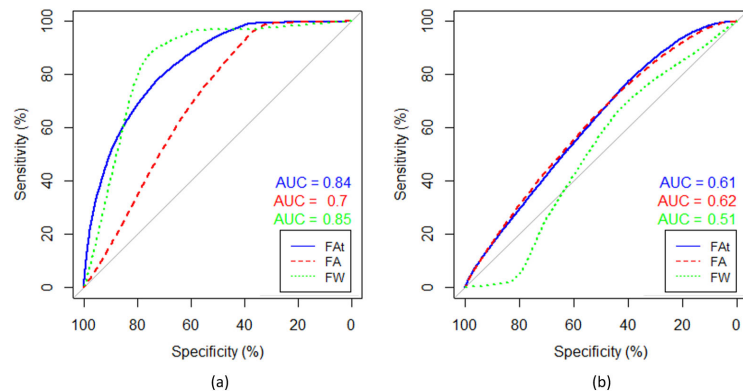


Figure 4. Receiver operator characteristics (ROCs) based on voxel-wise labelling. (a) ROC curves separating necrotic and enhancing tumor regions, and (b) ROC curves separating enhancing and non-enhancing tumor regions. Enhancing tumor region is defined as the true positive and the adjacent necrotic tumor region as the true negative. The patient is the same as the one shown in all single patient examples in this paper. The data were fitted to a logistic regression model and the ROC was computed for free-water (*FW*)-corrected fractional anisotropy (*FA_t*) (blue), non-corrected *FA* (red), and *FW* (green). Area under curve (AUC) is rendered in corresponding colors.

3.2. Impact of *FW* Correction on Parameter Distributions

FW elimination increases *FA* entropy ($p \leq 0.003$) and decreases *FA* skewness ($p \leq 0.004$) in the non-enhancing regions in both low- and high-grade tumors (Table 3). Kurtosis does not decrease significantly in low-grade tumors ($p = 0.90$) but does decrease significantly in high-grade tumors ($p \leq 0.001$). The *FA* distribution shifts toward higher *FA* values after *FW* correction. Refer to the Supplementary Material for a complete table of summary variables (Supplementary Material, Table S1). Maps calculated with and without *FW* correction are shown for a single patient in Figure 5.

Table 3. Comparison of fractional anisotropy summary variables with and without free water corrections in the non-enhancing tumor region. Reported p -values were computed according to the paired t -test and were adjusted with the Bonferroni method (significance threshold < 0.05).

Summary Variables from the Non-Enhancing Tumor Volume		Grade I and II (n = 9)		Grade III and IV (n = 16)	
		Mean and std. dev	p -Value	Mean and std. dev	p -Value
Entropy	<i>FA_t</i> *	7.21 ± 0.31	0.003	7.15 ± 0.15	<0.001
	<i>FA</i> **	6.73 ± 0.47		6.67 ± 0.35	
Kurtosis	<i>FA_t</i>	3.63 ± 1.44	0.90	3.57 ± 0.89	<0.001
	<i>FA</i>	7.86 ± 5.03		7.22 ± 3.76	
Skewness	<i>FA_t</i>	0.68 ± 0.51	0.004	0.59 ± 0.32	<0.001
	<i>FA</i>	1.58 ± 0.73		1.43 ± 0.71	

* *FA_t* = free-water-corrected fractional anisotropy, ** *FA* = non-corrected fractional anisotropy.

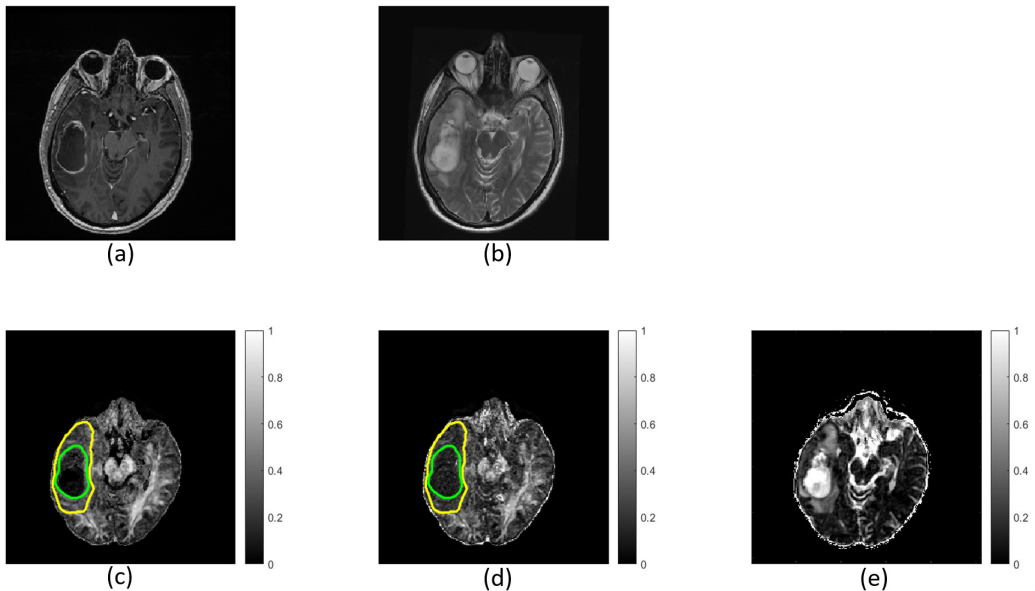


Figure 5. Images and maps from a grade IV patient: (a) T₁w image; (b) T₂w image; (c) free-water (FW)-corrected fractional anisotropy (FA_t) map; (d) non-corrected fractional anisotropy (FA) map with contours defining non-enhancing tumor; and (e) FW map. Within the non-enhancing region, more heterogeneity is revealed in the FA_t map compared to the FA map. The FW map quantitatively highlights FW content.

No significant correlation was found between tumors FW , FA_t , and FA (Supplementary Material, Table S2) nor to any parameter distribution summary variables apart from the mean (variance, 25th and 75th quantile, median, entropy, kurtosis, and skewness).

4. Discussion

Improved oncological imaging is dependent on an accurate description of tissue microenvironments, and descriptions of tumor heterogeneity may be improved by correcting for FW. The aim is to better characterize glioma by using FW modeling. Multi-shell DTI fitting to estimate and remove the FW contribution was performed using the method developed by Pasternak et al. [18]. The results indicate that by removing fluid bias from conventional FA maps, FW estimation and elimination allow for a quantitative non-invasive characterization of glioma, and FW correction improved automatic labelling of necrotic tumor voxels. Results show that FW correction significantly increases entropy across grades and significantly reduces kurtosis in high-grade tumors. Increased entropy may imply greater detected heterogeneity.

4.1. Characterizing Tumor Sub-Regions

FW maps show large variation of FW content within necrotic tumor regions across patients, suggesting that FW estimations can be an easily applicable method for quantitatively characterizing necrotic regions, as there is a reduction of cell density with necrosis [26,27]. Typically, lower grade patients do not have significant necrotic regions, but they may develop with progressing disease. Necrosis can be detected based on expert evaluations of MRI (post-contrast T₁w images in particular), but quantitative thresholds of FW content to characterize necrotic regions are not routinely applied in the clinic. Some studies have suggested that a more accurate description of the necrotic region helps with predicting survival and tumor aggressiveness in glioblastoma patients [40,41], and deep learning-based segmentation [42] and tumor classification [43] are being explored. Adding the estimation

of *FW* to such analyses is a possible, clinically useful application of *FW* estimation. Conventional *MD* that is not corrected for *FW* could not significantly differentiate between tumor regions. Calculating *FW* content may therefore add to a more precise description of the tumor.

The *FA* distribution within grade IV tumors changed significantly in all parts of the tumor region, except in the necrotic tumor region. Significant differences between *FA* and *FA_t* distributions were not present in *FW* correction of the necrotic tumor region as expected. The necrotic region contains large amounts of water, and due to the short *TR* used in this study, a concern could be incomplete signal spoiling in these regions. However, the diffusion signal versus *b*-values had the expected exponential decay (data not shown), confirming that the acquisition protocol did not bias the results. The *DWI* signal decay in both ventricles and the two most cystic necrotic volumes was found to be normal, and *FW* was estimated to one in both cases. It is possible that *FW* correction methods, such as the one applied in this study, can be of value in differentiating true disease progression from pseudo-progression [44]. Tumor cellularity, as derived with *RSL*, has been presented as a possible diagnostic tool in identifying pseudo-progression in glioblastoma [45,46]. The patients in this study are treatment-naïve; consequently, no pseudo-progression can be measured. Pseudo-progression is often accompanied by dead tissue and water, or it is due to immune cell infiltration [47]. Since the *FA* distribution changed significantly in enhancing and non-enhancing tumor regions and not in necrotic regions of these treatment-naïve patients, it is possible that pseudo-progression might be detected with *FW* correction in the enhancing and non-enhancing regions, if it could in the future be demonstrated that the *FA* distribution is also different in regions containing less structure due to dead tissue, water, or immune cell infiltration.

ROCs separating necrotic from enhancing tumor volumes had larger AUCs with applied *FW* correction than without. This implies that *FW*-corrected data may reduce partial volume effects, present on regular *DWI*, even if the tissues in enhancing volumes and non-enhancing volumes are not very different. We found no statistically significant differences between enhancing and non-enhancing tumor volumes based on *FA* or *FW*. It is important to note that ROC comparisons were performed with reference to regular structural *T₁w* and *T₂w* MR images and not histologically confirmed pathology. The logarithmic fits performed as part of the ROC curve calculations are relatively poor. This is because of the parameters *FW*, *FA_t*, and *FA* to some extent overlapping in, for example, necrotic and enhancing tumor regions. However, the point is not to fit the data to a logarithmic model, but merely to calculate a parameter cut-off point that provides a basis for a mathematical evaluation of ROC predictions. Based on “Restricted Spectrum Imaging” (*RSI*)-based tissue modelling, it has previously been demonstrated that accounting for *FW* components has been shown to help with tumor segmentation [48]. However, the study by White et al. [48] focused on the delineation between tumor and normal-appearing white matter based on various intensity ratios of *ADC* within tumor regions and normal-appearing white matter and not on calculations of *FW* or *FA_t*.

4.2. Impact of *FW* Correction on Parameter Distributions

The impact of free water elimination was found to significantly influence ROI summary variables, regardless of tumor grade when compared to regular diffusion tensor metrics. Entropy of *FA* increases in the tumor volume, which means that tissue heterogeneity may reflect the underlying heterogeneity better, helping in the assessment of the tumor microenvironment. Higher mean, median, and 25th and 75th quantiles in the *FW*-corrected maps show that the mass of the distribution is shifted towards higher *FA* values. There is an increase in median, quantiles, and mean *FA* after removal of *FW* contamination in the measured signal. These changes are expected when the isotropic signal is removed by the employed *FW*-correction method. Kurtosis and skewness decrease after *FW* correction, and the *FA_t* distribution comes closer to a normal distribution than the uncorrected *FA* distribution. This can be an effect of the increasing summary variables or an indication that

varying levels of FW are corrected for across the volume. *FAt* maps have higher entropy than *FA* maps, which may be indicative that FW correction reveals tissue heterogeneity. This heterogeneity may be due to, for example, fiber tracts or infiltrative tumor in the peritumoral tissue.

In our study, we were not able to identify *FW*, *FAt*, or *FA* distribution summary variables (mean, variance, 25th and 75th quantiles, median, entropy, kurtosis, or skewness) that correlated with tumor grades. This adds to inconsistent findings in previous studies, where some studies reported increased *MD* in high-grade glioma [8], while others reported decreased *MD* [9,49] or no difference in *MD* [11]. Since *MD* was used for initialization of the FW correction in our study, we do not report on *MD*. Similar to *MD*, *FA* has also been found to be increased [49], decreased [8], and not significantly different [9,11] across tumor grades, as well as to be increased in areas with recurrent tumors [44]. Kurtosis decreases in non-enhancing areas in high-grade tumors and not in low-grade tumors. This may be due to a larger number of low-grade tumors not having significant edema.

4.3. Limitations

FW correction provides more detail of the structures that are otherwise hidden beneath the edema, though apart from better characterization of the tumor regions, further studies are required to test the benefits of the FW correction in gliomas. Although tumor sub-regions were drawn on structural T₁w and T₂w MR images by an expert radiologist, the standard against which the FW-correction-based differentiation between tumor sub-regions were assessed should ideally be the pathology confirmed by histology. The method employed in our study makes use of multiple b-shell acquisitions. Nevertheless, it is still easily applicable in the clinic routine considering the limited increase in acquisition time. This study is a proof of concept, using previously acquired prospective data; hence, the sample size is limited. Another limitation is the quality of the diffusion-weighted imaging performed. Due to the relatively small number of signal acquisition from only eight diffusion directions, the *FW* and *FA* maps, as well as the *DWI* used for fiber tract reconstruction, are noisier than they could have been with more directions and signal averaging. However, the data represented in this study only took 4 min to acquire; therefore, it represents a clinically feasible scenario.

5. Conclusions

In conclusion, *FW* estimation is a way to quantitatively and non-invasively characterize necrotic tumor regions in particular. Monitoring potential changes within tumor regions due to developments of the disease may also be possible, though the hypothesis produced by these results must be further evaluated by histology of FW-mapped regions. Results based on *FA* maps of the tumor region are significantly impacted by FW correction, suggesting increased heterogeneity. The applied method is easily applicable in the clinic and reveals potentially important physiological information.

Supplementary Materials: The following are available online at <https://www.mdpi.com/article/10.3390/diagnostics11122385/s1>, Figure S1: Conventional MD from non-corrected data. The first four box and whisker plots from the left show the mean MD in enhancing tumor regions, necrotic tumor regions, non-enhancing tumor regions, and total tumor regions from grade IV patients. The fifth box and whisker plot shows the mean parameter values in total tumor regions from all patients. No statistical difference was found between tumor regions. Statistics were performed with ANOVA tests and Tukey's post hoc test at a significant threshold of $p < 0.05$. Table S1: Comparison of fractional anisotropy summary variables with and without free water corrections in the non-enhancing tumor volume. Reported p -values were computed according to the paired t -test and were adjusted with the Bonferroni method (significance threshold < 0.05), Table S2: Comparison of fractional anisotropy summary variables between low- and high-grade non-enhancing tumor volumes with and without free water corrections. Reported p -values were computed according to the unpaired t -test and were adjusted with the Bonferroni method (significance threshold < 0.05).

Author Contributions: Conceptualization: L.S., R.G. and F.R.; data curation: F.Z. and F.R.; formal analysis: L.S.; funding acquisition: F.Z. and F.A.G.; investigation: F.Z.; methodology: L.S. and F.R.; project administration: F.R.; resources: F.A.G.; software: O.P.; supervision: R.G. and F.R.; validation: L.S. and F.R.; visualization: L.S.; writing—original draft: L.S. and F.R.; writing—review and editing: L.S., F.Z., O.P., F.A.G., R.G. and F.R. All authors have read and agreed to the published version of the manuscript.

Funding: This work was supported by the Trond Mohn Foundation (BFS2018TMT05). This study also received funding from Cancer Research UK (CRUK; C19212/A16628) and the CRUK and Engineering and Physical Sciences Research Council (EPSRC) Cancer Imaging Centre in Cambridge and Manchester (C197/A16465). Additional support has been provided by the CRUK Cambridge Centre, the National Institute of Health Research (NIHR) Cambridge Biomedical Research Centre, and Addenbrooke’s Charitable Trust. The views expressed are those of the author(s) and not necessarily those of the NHS, the NIHR, or the Department of Health and Social Care.

Institutional Review Board Statement: The study was conducted according to the guidelines of the Declaration of Helsinki and approved 24 July 2008 by the NRES Committee of East England, Cambridge 2, REC number 07/H0308/245.

Informed Consent Statement: Informed consent was obtained from all subjects involved in the study.

Data Availability Statement: All data are available upon reasonable request and according to the funding sources’ policies from the corresponding author. Requests for materials should be addressed to F. R.

Acknowledgments: We would like to express our gratitude to the staff team for their help: Sarah Hilborne, Jackie Mason, Amy Fray, Ilse Patterson, Ronnie Hernandez, and Bruno Do Carmo.

Conflicts of Interest: The authors declare no conflict of interest.

References

1. Ostrom, Q.T.; Bauchet, L.; Davis, F.G.; Deltour, I.; Fisher, J.L.; Eastman Langer, C.; Pekmezci, M.; Schwartzbaum, J.A.; Turner, M.C.; Walsh, K.M.; et al. The epidemiology of glioma in adults: A “state of the science” review. *Neuro-Oncology* **2014**, *16*, 896–913. [[CrossRef](#)] [[PubMed](#)]
2. Ostrom, Q.T.; Cioffi, G.; Gittleman, H.; Patil, N.; Waite, K.; Kruchko, C.; Barnholtz-Sloan, J.S. CBTRUS Statistical Report: Primary Brain and Other Central Nervous System Tumors Diagnosed in the United States in 2012–2016. *Neuro-Oncology* **2019**, *21*, v1–v100. [[CrossRef](#)]
3. Crocetti, E.; Trama, A.; Stiller, C.; Caldarella, A.; Soffiotti, R.; Jaal, J.; Weber, D.C.; Ricardi, U.; Słowiński, J.; Brandes, A. Epidemiology of glial and non-glial brain tumours in Europe. *Eur. J. Cancer* **2012**, *48*, 1532–1542. [[CrossRef](#)]
4. Ostrom, Q.T.; Gittleman, H.; Liao, P.; Vecchione-Koval, T.; Wolinsky, Y.; Kruchko, C.; Barnholtz-Sloan, J.S. CBTRUS Statistical Report: Primary brain and other central nervous system tumors diagnosed in the United States in 2010–2014. *Neuro-Oncology* **2017**, *19*, v1–v88. [[CrossRef](#)] [[PubMed](#)]
5. Castellano, A.; Bailo, M.; Cicone, F.; Carideo, L.; Quartuccio, N.; Mortini, P.; Falini, A.; Cascini, G.; Minniti, G. Advanced Imaging Techniques for Radiotherapy Planning of Gliomas. *Cancers* **2021**, *13*, 1063. [[CrossRef](#)] [[PubMed](#)]
6. Lupo, J.M.; Nelson, S.J. Advanced Magnetic Resonance Imaging Methods for Planning and Monitoring Radiation Therapy in Patients With High-Grade Glioma. *Semin. Radiat. Oncol.* **2014**, *24*, 248–258. [[CrossRef](#)]
7. Zaccagna, F.; Grist, J.T.; Quartuccio, N.; Riemer, F.; Fraioli, F.; Caracò, C.; Halsey, R.; Aldalilah, Y.; Cunningham, C.H.; Massoud, T.F.; et al. Imaging and treatment of brain tumors through molecular targeting: Recent clinical advances. *Eur. J. Radiol.* **2021**, *142*, 109842. [[CrossRef](#)] [[PubMed](#)]
8. El-Serougy, L.; Razek, A.A.K.A.; Ezzat, A.; Eldawoody, H.; El-Morsy, A. Assessment of diffusion tensor imaging metrics in differentiating low-grade from high-grade gliomas. *Neuroradiol. J.* **2016**, *29*, 400–407. [[CrossRef](#)]
9. Lee, H.Y.; Na, D.G.; Song, I.-C.; Lee, D.H.; Seo, H.S.; Kim, J.-H.; Chang, K.-H. Diffusion-Tensor Imaging for Glioma Grading at 3-T Magnetic Resonance Imaging. *J. Comput. Assist. Tomogr.* **2008**, *32*, 298–303. [[CrossRef](#)] [[PubMed](#)]
10. White, M.; Zhang, Y.; Yu, F.; Kazmi, S. Diffusion Tensor MR Imaging of Cerebral Gliomas: Evaluating Fractional Anisotropy Characteristics. *Am. J. Neuroradiol.* **2010**, *32*, 374–381. [[CrossRef](#)]
11. Jakab, A.; Molnár, P.; Emri, M.; Berényi, E. Glioma grade assessment by using histogram analysis of diffusion tensor imaging-derived maps. *Neuroradiology* **2011**, *53*, 483–491. [[CrossRef](#)] [[PubMed](#)]
12. Li, Y.; Zhang, W. Quantitative evaluation of diffusion tensor imaging for clinical management of glioma. *Neurosurg. Rev.* **2018**, *43*, 881–891. [[CrossRef](#)] [[PubMed](#)]
13. Azad, T.D.; Duffau, H. Limitations of functional neuroimaging for patient selection and surgical planning in glioma surgery. *Neurosurg. Focus* **2020**, *48*, E12. [[CrossRef](#)] [[PubMed](#)]

14. Wende, T.; Hoffmann, K.-T.; Meixensberger, J. Tractography in Neurosurgery: A Systematic Review of Current Applications. *J. Neurol. Surg. Part A Central Eur. Neurosurg.* **2020**, *81*, 442–455. [[CrossRef](#)]
15. Goebell, E.; Fiehler, J.; Ding, X.-Q.; Paustenbach, S.; Nietz, S.; Heese, O.; Kucinski, T.; Hagel, C.; Westphal, M.; Zeumer, H. Disarrangement of Fiber Tracts and Decline of Neuronal Density Correlate in Glioma Patients—A Combined Diffusion Tensor Imaging and 1H-MR Spectroscopy Study. *Am. J. Neuroradiol.* **2006**, *27*, 1426–1431. [[PubMed](#)]
16. Price, S.J.; Gillard, J.H. Imaging biomarkers of brain tumour margin and tumour invasion. *Br. J. Radiol.* **2011**, *84*, S159–S167. [[CrossRef](#)] [[PubMed](#)]
17. Maier, S.E.; Sun, Y.; Mulkern, R.V. Diffusion imaging of brain tumors. *NMR Biomed.* **2010**, *23*, 849–864. [[CrossRef](#)]
18. Pasternak, O.; Sochen, N.; Gur, Y.; Intrator, N.; Assaf, Y. Free water elimination and mapping from diffusion MRI. *Magn. Reson. Med.* **2009**, *62*, 717–730. [[CrossRef](#)]
19. Pasternak, O.; Shenton, M.E.; Westin, C.-F. Estimation of Extracellular Volume from Regularized Multi-shell Diffusion MRI. *Lect. Notes Comput. Sci.* **2012**, *15*, 305–312. [[CrossRef](#)]
20. Hoy, A.R.; Koay, C.G.; Keckemeter, S.R.; Alexander, A.L. Optimization of a free water elimination two-compartment model for diffusion tensor imaging. *NeuroImage* **2014**, *103*, 323–333. [[CrossRef](#)] [[PubMed](#)]
21. Parker, D.; Ismail, A.A.O.; Wolf, R.; Brem, S.; Alexander, S.; Hodges, W.; Pasternak, O.; Caruyer, E.; Verma, R. Freewater estimator using interpolated initialization (FERNET): Characterizing peritumoral edema using clinically feasible diffusion MRI data. *PLoS ONE* **2020**, *15*, e0233645. [[CrossRef](#)]
22. Pierpaoli, C.; Jones, D.K. Removing CSF Contamination in Brain DT-MRIs by Using a Two-Compartment Tensor Model. In Proceedings of the ISMRM, Kyoto, Japan, 15–21 May 2004.
23. Yu, Y.; Ma, Y.; Sun, M.; Jiang, W.; Yuan, T.; Tong, D. Meta-analysis of the diagnostic performance of diffusion magnetic resonance imaging with apparent diffusion coefficient measurements for differentiating glioma recurrence from pseudoprogression. *Medicine* **2020**, *99*, e20270. [[CrossRef](#)] [[PubMed](#)]
24. Kim, J.Y.; Park, J.E.; Jo, Y.; Shim, W.H.; Nam, S.J.; Kim, J.H.; Yoo, R.-E.; Choi, S.H.; Kim, H.S. Incorporating diffusion- and perfusion-weighted MRI into a radiomics model improves diagnostic performance for pseudoprogression in glioblastoma patients. *Neuro-Oncology* **2019**, *21*, 404–414. [[CrossRef](#)]
25. Schmainda, K.M. Diffusion-weighted MRI as a biomarker for treatment response in glioma. *CNS Oncol.* **2012**, *1*, 169–180. [[CrossRef](#)] [[PubMed](#)]
26. Herneth, A.M.; Guccione, S.; Bednarski, M. Apparent Diffusion Coefficient: A quantitative parameter for in vivo tumor characterization. *Eur. J. Radiol.* **2003**, *45*, 208–213. [[CrossRef](#)]
27. Eidel, O.; Burth, S.; Neumann, J.-O.; Kieslich, P.J.; Sahm, F.; Jungk, C.; Kickingereder, P.V. (Né; Bickelhaupt, S.; Mundiyanapurath, S.; Bäumer, P.; et al. Tumor Infiltration in Enhancing and Non-Enhancing Parts of Glioblastoma: A Correlation with Histopathology. *PLoS ONE* **2017**, *12*, e0169292. [[CrossRef](#)]
28. Gong, S.; Zhang, F.; Norton, I.; Essayed, W.I.; Unadkat, P.; Rigolo, L.; Pasternak, O.; Rathi, Y.; Hou, L.; Golby, A.J.; et al. Free water modeling of peritumoral edema using multi-fiber tractography: Application to tracking the arcuate fasciculus for neurosurgical planning. *PLoS ONE* **2018**, *13*, e0197056. [[CrossRef](#)] [[PubMed](#)]
29. Ismail, A.A.L.; Parker, D.; Hernandez-Fernandez, M.; Bre, S.; Alexander, S.; Pasternak, O.; Caruyer, E.; Verma, R. Characterizing Peritumoral Tissue Using Free Water Elimination in Clinical DTI. In *Brainlesion: Glioma, Multiple Sclerosis, Stroke and Traumatic Brain Injuries, Proceedings of the 4th International Workshop, BrainLes 2018, Granada, Spain, 16 September, 2018*; Crimi, A., Bakas, S., Kuijff, H., Keyvan, F., Reye, M., van Walsum, T., Eds.; Springer Nature: Cham, Switzerland, 2019.
30. Weninger, L.; Na, C.-H.; Jütten, K.; Merhof, D. Analyzing the effects of free water modeling by deep learning on diffusion MRI structural connectivity estimates in glioma patients. *PLoS ONE* **2020**, *15*, e0239475. [[CrossRef](#)]
31. McDonald, C.R.; White, N.S.; Farid, N.; Lai, G.; Kuperman, J.M.; Bartsch, H.; Hagler, D.J.; Kesari, S.; Carter, B.S.; Chen, C.C.; et al. Recovery of White Matter Tracts in Regions of Peritumoral FLAIR Hyperintensity with Use of Restriction Spectrum Imaging. *Am. J. Neuroradiol.* **2013**, *34*, 1157–1163. [[CrossRef](#)]
32. Chen, Z.; Tie, Y.; Olubiyi, O.; Zhang, F.; Mehrtash, A.; Rigolo, L.; Kahali, P.; Norton, I.; Pasternak, O.; Rathi, Y.; et al. Corticospinal tract modeling for neurosurgical planning by tracking through regions of peritumoral edema and crossing fibers using two-tensor unscented Kalman filter tractography. *Int. J. Comput. Assist. Radiol. Surg.* **2016**, *11*, 1475–1486. [[CrossRef](#)]
33. Louis, D.N.; Perry, A.; Reifenberger, G.; von Deimling, A.; Figarella-Branger, D.; Cavenee, W.K.; Ohgaki, H.; Wiestler, O.D.; Kleihues, P.; Ellison, D.W. The 2016 World Health Organization Classification of Tumors of the Central Nervous System: A summary. *Acta Neuropathol.* **2016**, *131*, 803–820. [[CrossRef](#)]
34. Louis, D.N.; Ohgaki, H.; Wiestler, O.D.; Cavenee, W.K.; Burger, P.C.; Jouvet, A.; Scheithauer, B.W.; Kleihues, P. The 2007 WHO Classification of Tumours of the Central Nervous System. *Acta Neuropathol.* **2007**, *114*, 97–109. [[CrossRef](#)] [[PubMed](#)]
35. Dietrich, O. Diffusion Coefficients of Water. 2018. Available online: <https://dtrx.de/od/diff/index.html> (accessed on 13 August 2021).
36. Pasternak, O.; Sochen, N.; Basser, P.J. The effect of metric selection on the analysis of diffusion tensor MRI data. *NeuroImage* **2010**, *49*, 2190–2204. [[CrossRef](#)]
37. Jenkinson, M.; Smith, S. A global optimisation method for robust affine registration of brain images. *Med. Image Anal.* **2001**, *5*, 143–156. [[CrossRef](#)]
38. Smith, S.M. Fast robust automated brain extraction. *Hum. Brain Mapp.* **2002**, *17*, 143–155. [[CrossRef](#)] [[PubMed](#)]

39. Penny, W.; Friston, K.; Ashburner, J.; Kiebel, S. *Statistical Parametric Mapping: The Analysis of Functional Brain Images*, 1st ed.; Academic Press: London, UK, 2006.
40. Ishii, A.; Kimura, T.; Sadahiro, H.; Kawano, H.; Takubo, K.; Suzuki, M.; Ikeda, E. Histological Characterization of the Tumorigenic “Peri-Necrotic Niche” Harboring Quiescent Stem-Like Tumor Cells in Glioblastoma. *PLoS ONE* **2016**, *11*, e0147366. [[CrossRef](#)]
41. Liu, S.; Wang, Y.; Xu, K.; Wang, Z.; Fan, X.; Zhang, C.; Li, S.; Qiu, X.; Jiang, T. Relationship between necrotic patterns in glioblastoma and patient survival: Fractal dimension and lacunarity analyses using magnetic resonance imaging. *Sci. Rep.* **2017**, *7*, 1–7. [[CrossRef](#)]
42. Wan, Y.; Rahmat, R.; Price, S.J. Deep learning for glioblastoma segmentation using preoperative magnetic resonance imaging identifies volumetric features associated with survival. *Acta Neurochir.* **2020**, *162*, 3067–3080. [[CrossRef](#)] [[PubMed](#)]
43. Kobayashi, K.; Miyake, M.; Takahashi, M.; Hamamoto, R. Observing deep radiomics for the classification of glioma grades. *Sci. Rep.* **2021**, *11*, 1–13. [[CrossRef](#)]
44. Metz, M.-C.; Molina-Romero, M.; Lipkova, J.; Gempt, J.; Liesche-Starnecker, F.; Eichinger, P.; Grundl, L.; Menze, B.; Combs, S.E.; Zimmer, C.; et al. Predicting Glioblastoma Recurrence from Preoperative MR Scans Using Fractional-Anisotropy Maps with Free-Water Suppression. *Cancers* **2020**, *12*, 728. [[CrossRef](#)]
45. Daghighi, S.; Bahrami, N.; Tom, W.; Coley, N.; Seibert, T.M.; Hattangadi-Gluth, J.A.; Piccioni, D.E.; Dale, A.M.; Farid, N.; McDonald, C.R. Restriction Spectrum Imaging Differentiates True Tumor Progression From Immune-Mediated Pseudoprogression: Case Report of a Patient With Glioblastoma. *Front. Oncol.* **2020**, *10*, 1–6. [[CrossRef](#)] [[PubMed](#)]
46. Khan, U.A.; Rennert, R.C.; White, N.S.; Bartsch, H.; Farid, N.; Dale, A.M.; Chen, C.C. Diagnostic utility of restriction spectrum imaging (RSI) in glioblastoma patients after concurrent radiation-temozolomide treatment: A pilot study. *J. Clin. Neurosci.* **2018**, *58*, 136–141. [[CrossRef](#)] [[PubMed](#)]
47. Thust, S.C.; Bent, M.J.V.D.; Smits, M. Pseudoprogression of brain tumors. *J. Magn. Reson. Imaging* **2018**, *48*, 571–589. [[CrossRef](#)] [[PubMed](#)]
48. White, N.; McDonald, C.; Farid, N.; Kuperman, J.; Kesari, S.; Dale, A. Improved Conspicuity and Delineation of High-Grade Primary and Metastatic Brain Tumors Using “Restriction Spectrum Imaging”: Quantitative Comparison with High B-Value DWI and ADC. *Am. J. Neuroradiol.* **2013**, *34*, 958–964. [[CrossRef](#)]
49. Holly, K.; Barker, B.J.; Murcia, D.; Bennett, R.; Kalakoti, P.; Ledbetter, C.; Gonzalez-Toledo, E.; Nanda, A.; Sun, H. High-grade Gliomas Exhibit Higher Peritumoral Fractional Anisotropy and Lower Mean Diffusivity than Intracranial Metastases. *Front. Surg.* **2017**, *4*, 18. [[CrossRef](#)]



Graphic design: Communication Division, UIB / Print: Skjipes Kommunikasjon AS



uib.no

ISBN: 9788230853627 (print)
9788230856321 (PDF)